# 7.06 Temperatures, Heat, and Energy in the Mantle of the Earth

**C Jaupart**, Institut de Physique du Globe de Paris, Paris, France
**S Labrosse**, Ecole Normale Supérieure de Lyon, Lyon, France
**F Lucazeau**, Institut de Physique du Globe de Paris, Paris, France
**J-C Mareschal**, Université du Québec à Montréal, Montréal, QC, Canada

© 2015 Elsevier B.V. All rights reserved.

This chapter is a revision of the previous edition chapter by C Jaupart, S Labrosse and J.-C Mareschal, Volume 7, pp. 253–303, © 2007, Elsevier B.V.

## 7.06.1 Introduction

Even a cursory historical look at the development of geology reveals that the cooling of the Earth has always been a central issue (Birch, 1965; Fourier, 1824; Holmes, 1915; Joly, 1909; McDonald, 1959; Strutt, 1906; Thomson, 1864; Urey, 1964). From Hutton's view that there is no beginning or end to geologic time to today's debate on how far back in time plate tectonics can be traced, arguments eventually boil down to statements on our planet's thermal evolution. At the time of Fourier and Kelvin, the Earth's temperature gradient was estimated to be in the range 20–30 K $km^{-1}$, close to what we know today after more than six decades of heat flow measurements on land and at sea. Kelvin thought that this piece of data would constrain the age of the Earth and concluded from his famous calculation that the Earth was probably not much older than 100 My. The failure of Kelvin's model has usually been attributed to two assumptions, namely, that the Earth is cooling by conduction and that there are no sources of heat inside the Earth. In retrospect, one could argue that an equally damaging flaw was the inadequate data set that was available to him. Had Kelvin known that the heat flux varies by large amounts at the Earth's surface, he might not have advocated a simple uniform cooling model for the whole planet. The large lateral variations of heat flux that occur on Earth provide information on cooling mechanisms and heat sources that are as important as the global average.

Today, we know that the Earth is not cooling by conduction only and that the convective motions that drive the oceanic plates are responsible for a large fraction of its heat loss. We also know that heat generated by the radioactive decay of U, Th, and K in silicate rocks accounts for a large fraction of the surface heat loss. It is fair to state, however, that the Earth's heat engine works in ways that still elude us. In this context, it is worth remembering that we pursue two different goals in studies of mantle convection. One is to account for its present-day dynamics and for its role in shaping the Earth's surface features. The other goal is to go back in time in order to evaluate how the rates of geologic processes have changed and to decipher processes that are no longer active today. Both goals require a thorough understanding of the Earth's heat budget, but each relies on a different set of constraints. The former can be attained using present-day observations, such as the distributions of seismic velocities and density at depth. The latter goal requires knowledge of how the convective regime evolved as the Earth cooled down and its energy sources ran down. From another standpoint, the present-day energy budget of the planet and the distribution of heat flux at the surface are constraints that mantle convection models must satisfy.

The present-day energy budget reflects how the Earth's convective engine has evolved through geologic time. The power of this constraint has motivated a large number of studies. With hindsight, one may link the emergence of convection models to the failure of conductive (and radiative) thermal history models to account for the mantle temperature regime and the Earth energy budget (Jacobs, 1961; Jacobs and Allan, 1956; MacDonald, 1959). Convection in the Earth's mantle had become inescapable and was required to explain why the mantle is not fully molten today. The difficulty in running fully consistent dynamic calculations of convection over the whole history of our planet led to the so-called parameterized models such that the heat flux out of the Earth is written directly as a function of dimensionless numbers describing the bulk convective system, such as the Rayleigh number (Schubert et al., 2001). For a given set of initial conditions, the model results were required to match the present-day energy budget or more precisely the ratio of heat production to heat loss (the 'Urey' ratio). The earliest study of this kind was probably that of McKenzie and Weiss (1975) and was followed by countless others. This approach was used to argue against whole-layer mantle convection (McKenzie and Richter, 1981), to date the emergence of plate tectonics (Peltier and Jarvis, 1982), to derive constraints on the distribution of radiogenic heat sources in the mantle (Schubert et al., 1980), and even to determine the amount of radioactive sources in the Earth's core (Breuer and Spohn, 1993; Davies, 1980a,b). The difficulty in accounting for the wealth of processes that characterize the Earth, such as continental growth as well as degassing and the implied changes of rheological properties, however, has led to disenchantment. Yet, it is clear that the present-day thermal and tectonic regime of the Earth results from several billion years of convective processes and is best understood within a time-dependent framework.

Determination of the Earth's rate of heat loss requires a very large number of heat flux measurements in a variety of geologic settings. Local surveys as well as global analyses of large data sets have shown that heat flux varies on a wide range of spatial

scales and, in the continents, is not a function of a single variable such as geologic age. Heat flux data exhibit large scatter, which has had unfortunate consequences. One has been that few scientists have invested time and energy to sort out the large number of physical processes that come into play. The 1980s saw a rapid decrease in the number of research teams active in that field as well as in the number of measurements carried out at sea and on land. Another consequence has been that, with few notable exceptions (e.g., Coltice et al., 2012; Pari and Peltier, 2000), the distribution of heat flux is rarely used to test the validity of mantle convection calculations. Many evolutionary models for the Earth's mantle have abandoned the energy budget as a viable constraint and rely on geochemical data. Here, we will assess the reliability of heat flux measurements and shall demonstrate that the spatial distribution of heat flux provides a key constraint for understanding convection in the Earth.

The last three decades have seen notable advances in the interpretation of heat flux. In the oceans, these include a thorough understanding of hydrothermal circulation through oceanic crust and sediments, as well as detailed and precise heat flux measurements through both very young and very old seafloor. In the continents, sampling of old cratons is now adequate in several areas, heat production of lower crustal assemblages is better understood, and systematic studies of heat flux and heat production allow strong constraints on the crustal contribution to the surface heat flux. Today, we have a better understanding of the energy sources in the Earth than we did 30 years ago and know how large some of the uncertainties are.

In this chapter, we shall focus on two different, but closely related, problems. One is to evaluate the present-day energy budget of the mantle with emphasis on the associated uncertainties. The other is to evaluate how thermal evolution models must be developed in order to account for this budget. We shall establish the gross thermodynamics of the Earth and shall explain how estimates of heat loss and heat production have been obtained, drawing from recent advances. We shall emphasize the peculiarities of heat loss mechanisms of our planet and in particular the spatial distribution of heat flux. We shall then rely on this budget to infer the present-day secular cooling rate of our planet. We shall also evaluate independent constraints on temperature in the Earth's mantle and present a reference temperature profile through the convective mantle. Finally, we shall discuss the thermal evolution of our planet, from the standpoint of both observations and theoretical models. In order to facilitate the reader's task, we give a short summary of major points at the end of each section.

## 7.06.2 Basic Thermodynamics

### 7.06.2.1 Breakdown of the Energy Budget

The integral form of the energy balance for the whole planet takes the form

$$\frac{\mathrm{d}\left(U+E_\mathrm{c}+E_\mathrm{g}\right)}{\mathrm{d}t}=-\int_\mathrm{A}\boldsymbol{q}\cdot\boldsymbol{n}\,\mathrm{d}A+\int_\mathrm{V}H\mathrm{d}V+\int_\mathrm{V}\psi\mathrm{d}V-p_\mathrm{a}\frac{\mathrm{d}V}{\mathrm{d}t} \quad [1]$$

where $U$ is internal energy, $E_\mathrm{c}$ is kinetic energy, and $E_\mathrm{g}$ is gravitational potential energy. $\boldsymbol{q}$ is the surface heat flux, $n$ is the unit normal vector, $A$ is the Earth's outer surface, $H$ is internal heat production per unit volume, $p_\mathrm{a}$ is atmospheric pressure, $V$ is the Earth's total volume, and $\psi$ is energy transfers to or from external systems, such as tidal dissipation. Table 1 provides a list of the main symbols used in this chapter. Equation [1] states that the Earth's total energy changes due to heat loss, internal heat generation, energy transfer between our planet's interior and its surroundings (atmosphere as well as other celestial bodies), and finally the work of atmospheric pressure as the planet contracts. We have assumed that the Earth's surface is shear stress-free. Dissipation induced by internal convective motions and chemical differentiation is not written in because it is involved in internal transfers of energy and does not act to change the total energy of the system. The state variables include pressure, temperature, and chemical composition, which may all vary as a function of time and

**Table 1** Symbols used

| *Symbol* | *Definition* | *Units (commonly used units or value)* |
|---|---|---|
| $C_\mathrm{p}$ | Heat capacity | J kg$^{-1}$ K$^{-1}$ |
| $C_\mathrm{Q}$ | Heat flux/age$^{1/2}$ | 470 – 510 mW m$^{-2}$/(My)$^{1/2}$ |
| $C_\mathrm{A}$ | Seafloor accretion rate | 3.34 km$^2$ My$^{-1}$ |
| $D$ | Thickness of convecting layer | m |
| $E_\mathrm{c}$ | Kinetic energy | J |
| $E_\mathrm{g}$ | Gravitational potential energy | J |
| $E_\mathrm{rot}$ | Rotational energy | J |
| $E_\mathrm{s}$ | Strain energy | J |
| $F_\mathrm{b}$ | Buoyancy flux | W |
| $g$ | Acceleration of gravity | m s$^{-1}$ |
| $G$ | Gravitational constant | $6.67\times10^{-11}$kg m$^3$ s$^{-2}$ |
| $H$ | (Volumetric) heat production | W m$^{-3}$ ($\mu$W m$^{-3}$) |
| $I$ | Moment of inertia | kg m$^2$ |
| $K$ | Bulk modulus | Pa |
| $L$ | Length of oceanic plate (length scale) | m |
| $M$ | Mass of Earth | kg |
| $Q$, $q$ | Heat flux | W m$^{-2}$ (mW m$^{-2}$) |
| $p$ | Pressure | Pa (MPa, GPa) |
| $R$ | Radius of Earth | km (6378) |
| $Ra$ | Rayleigh number | / |
| $s$ | Entropy per unit mass | J kg$^{-1}$ K$^{-1}$ |
| $T$ | Temperature | K (°C) |
| $u$ | Internal energy per unit mass (also used for horizontal velocity component) | J kg$^{-1}$ |
| $U$ | Internal energy (also used for horizontal velocity component) | J |
| $Ur$ | Urey number | |
| $V$ | Volume | m$^3$ |
| $w$ | Radial velocity | |
| $\alpha$ | Volumetric expansion coefficient | K$^{-1}$ |
| $\gamma$ | Grüneisen parameter | |
| $\kappa$ | Thermal diffusivity | m$^2$ s$^{-1}$ |
| $\lambda$ | Thermal conductivity | W m$^{-1}$ K$^{-1}$ |
| $\mu$ | Viscosity | Pa s |
| $\Omega$ | Angular velocity | rad s$^{-1}$ |
| $\Phi$ | Heat dissipated by friction | W m$^{-3}$ |
| $\Psi$ | External energy sources | W m$^{-3}$ |
| $\rho$ | Density | kg m$^{-3}$ |
| $\Delta S_\mathrm{cond}$ | Entropy production | J K$^{-1}$ |
| $\sigma$ | Deviatoric stress tensor | Pa (MPa) |

position within the planet. Chemical differentiation proceeds mostly by the gravity-driven separation of different phases, which entails the transformation of gravitational potential energy into heat by viscous dissipation with no change of the total energy. In this chapter, we shall not dwell at length on such processes. The largest segregation events, such as the formation of the Earth's core and, possibly, the separation of two distinct mantle reservoirs through crystal–melt separation in a magma ocean, occurred very early on. These events set up the initial conditions for secular thermal evolution involving no major chemical separation process energy-wise. Extraction of continental crust out of the mantle has been active more or less continuously since the beginning, but we shall show that the magnitude of the induced energy change is small compared to other items in the energy budget. We shall therefore write thermodynamic principles using only temperature and pressure as variables of state. We shall not deal with the orbital energy of the Sun–Earth system and shall not discuss changes of the kinetic energy of the Earth's revolution around the Sun and associated changes of gravitational energy due to variations of the Earth's orbit.

Our main purpose in this chapter is to evaluate the different terms in the energy balance and to derive an equation for the average temperature of the Earth. The dominant terms on the right of the energy balance equation [1] are the Earth's rate of heat loss and internal heat generation, which are inferred from field measurements and chemical Earth models. The other terms are evaluated theoretically and are shown to be negligible. We explain how internal energy transfers operate and show that changes of gravitational energy are compensated by changes of strain energy $E_S$, which is the energy required to compress matter to its actual local pressure $p$.

The gravitational energy of the Earth is defined as the energy required to bring matter from infinity and, assuming spherical symmetry, can be written as

$$E_g = -\int_0^R \rho(r) g(r) r 4\pi r^2 \mathrm{d}r \qquad [2]$$

with $\rho$ and $g$ the spatially varying density and gravity. This energy is negative because the accretion process releases energy. This energy can be computed for the present Earth and an upper limit can be obtained for a sphere with uniform density:

$$E_g = -\frac{3}{5}\frac{GM^2}{R} \qquad [3]$$

where $G$ is the gravitational constant and $M$ is the mass of the Earth.

Kinetic energy may be broken down into several different components:

$$E_c = E_{rot} + E_{contr} + E_{conv} \qquad [4]$$

corresponding to the bulk rotation of our planet, radial contraction induced by secular cooling, and internal convective motions, respectively. One may easily show that the latter two are small compared to the first one.

Table 2 lists estimates for gravitational, kinetic, and internal energy components and makes it clear that kinetic energy is very small compared to the other two. A striking result is that the largest component by far is gravitational energy, which is larger than internal energy by at least one order of magnitude. In a constant mass planet, gravitational energy changes due to thermal contraction, chemical differentiation, and vertical movements of the Earth's surface (tectonic processes and erosion–deposition). These various processes work in different ways and are associated with different energy transport mechanisms and hence must be dealt with separately.

**Table 2** Numbers: order of magnitude

| | *Value* | *Units* |
|---|---|---|
| Rotational energy | $2.1 \times 10^{29}$ | J |
| Internal energy (for 2500 K average temperature) | $1.7 \times 10^{31}$ | J |
| Gravitational energy (uniform sphere) | $2.2 \times 10^{32}$ | J |
| Rotation angular velocity | $7.292 \times 10^{-5}$ | rad $s^{-1}$ |
| Polar moment of inertia | $8.0363 \times 10^{37}$ | kg $m^2$ |
| Total mass | $5.9737 \times 10^{24}$ | kg |
| Total volume | $1.08 \times 10^{21}$ | $m^3$ |
| Mass mantle | $\approx 4.0 \times 10^{24}$ | kg |
| Mass crust | $\approx 2.8 \times 10^{22}$ | kg |

### 7.06.2.2 Changes in Gravitational Energy: Contraction due to Secular Cooling

Gravitational energy is the largest component of the budget (Table 2), and special care is warranted to evaluate how it gets converted to other forms of energy when the planet contracts. This has been discussed in a series of papers (Flasar and Birch, 1973; Lapwood, 1952). Here, we avoid detailed calculations and throw light on some interesting thermodynamic aspects.

The gravitational energy changes when the planet contracts:

$$\frac{\Delta E_g}{E_g} = -\frac{\Delta R}{R} \qquad [5]$$

Neglecting changes of pressure and gravity and assuming uniform cooling by an amount $\Delta T$,

$$\frac{\Delta R}{R} \approx \frac{\langle\alpha\rangle \Delta T}{3} \qquad [6]$$

where $\langle\alpha\rangle$ is an average value for the coefficient of thermal expansion and $\Delta T$ is negative. In Appendix A, we show that the changes of pressure and gravity that are induced by the contraction process enhance the contraction rate. Assuming $\langle\alpha\rangle \approx 2 \times 10^{-5}\,\mathrm{K}^{-1}$ and a secular cooling rate of 100 K $\mathrm{Gy}^{-1}$, the contraction velocity is $\mathrm{d}R/\mathrm{d}t \approx -10^{-13}\,\mathrm{m\,s}^{-1}$, a very small value compared to the typical convective velocity of $\approx 10^{-9}$ m $\mathrm{s}^{-1}$. The induced change of gravitational energy, however, is far from being negligible. For the same choice of parameter values, it is $\approx 4$ TW, which, as we shall see, corresponds to 10% of the total energy loss of our planet. We shall demonstrate, however, that such changes of gravitational energy are not converted to heat.

Thermal contraction affects the planet's rotation. The moment of inertia $I$ changes:

$$\Delta I/I = 2\Delta R/R \qquad [7]$$

and hence,

$$\Delta E_{rot}/E_{rot} = \Delta\Omega/\Omega = -2\Delta R/R \qquad [8]$$

where $\Omega$ is the Earth rotation velocity. Thus, some of the gravitational potential energy goes into the energy of rotation. Rotational energy is much less (three orders of magnitude)

than gravitational energy, however, and hence may be neglected in the present analysis.

To elucidate energy transfer processes, we now consider thermodynamics at the local scale. We focus on a few specific aspects of interest and refer the reader to the study by Braginsky and Roberts (1995) for a comprehensive analysis. All energies are now written per unit mass with small letters, that is, $e_c$ and $u$ stand for the kinetic energy and internal energy per unit mass, respectively. We begin with the standard form of the first law of thermodynamics (Bird et al., 1960; Schubert et al., 2001; see also **Chapter 7.02** by Ricard in this volume):

$$\rho\frac{\mathrm{D}(u+e_c)}{\mathrm{D}t}=-\nabla\cdot\boldsymbol{q}-\nabla\cdot(p\mathbf{v})-\nabla\cdot[\boldsymbol{\sigma}\cdot\mathbf{v}]+H+\psi+\rho\mathbf{g}\cdot\mathbf{v} \qquad [9]$$

where $\boldsymbol{\sigma}$ is the deviatoric stress tensor, $\mathbf{v}$ is velocity, and $\psi$ collects external source terms such as tidal dissipation. We have adopted the convention that $\boldsymbol{\sigma}$ denotes stresses acting on material located on the positive side of a surface. From the momentum equation, we get

$$\rho\frac{\mathrm{D}e_c}{\mathrm{D}t}=\rho\frac{\mathrm{D}\left(\frac{\mathbf{v}^2}{2}\right)}{\mathrm{D}t}=-\mathbf{v}\cdot\boldsymbol{\nabla}p-\mathbf{v}\cdot\boldsymbol{\nabla}\cdot\boldsymbol{\sigma}+\rho\mathbf{g}\cdot\mathbf{v} \qquad [10]$$

Subtracting this from the total energy balance leads to an equation for the internal energy:

$$\rho\frac{\mathrm{D}u}{\mathrm{D}t}=-\nabla\cdot\mathbf{q}+H+\psi+\phi-p\boldsymbol{\nabla}\cdot\mathbf{v} \qquad [11]$$

where $\phi$ stands for viscous dissipation:

$$\phi=-\nabla\cdot[\boldsymbol{\sigma}\cdot\mathbf{v}]+\mathbf{v}\cdot\nabla\cdot\boldsymbol{\sigma}=-\boldsymbol{\sigma}:\nabla\mathbf{v} \qquad [12]$$

Equation [11] is thus the usual statement that changes of internal energy $u$ are due to heat gains or losses (which are broken into four contributions) and to the work of pressure (the last term on the right).

All the equations earlier stem from standard thermodynamics theory. We now introduce gravitational energy and strain energy. We decompose variables into the sum of the azimuthal average and a perturbation, such as

$$T=\overline{T}+\theta \qquad [13]$$

for temperature. The velocity field is decomposed into a component due to contraction, $\mathbf{v}_c$, and a convective component, $\mathbf{w}$. We consider separately the effects of contraction, which act on the average density and pressure, and the effects of convection, which involve departures from these averages.

We may assume that contraction proceeds in conditions close to hydrostatic equilibrium, such that it involves no deviatoric stress and no dissipation. In this case, the azimuthal average of the momentum equation reduces to a hydrostatic balance:

$$0=-\nabla\overline{p}+\overline{\rho}\mathbf{g} \qquad [14]$$

For the contraction process with velocity $\mathbf{v}_c$, we may break down internal energy changes as follows:

$$\overline{\rho}\frac{\mathrm{D}u}{\mathrm{D}t}=\overline{\rho}T\frac{\mathrm{D}s}{\mathrm{D}t}-\overline{p}\nabla\cdot\mathbf{v}_c \qquad [15]$$

where $s$ is the entropy per unit mass and where we identify the work done by pressure as a change of strain energy:

$$-\overline{p}\nabla\cdot\mathbf{v}_c=\overline{\rho}\frac{\mathrm{D}e_s}{\mathrm{D}t} \qquad [16]$$

In the total energy balance equation [9], the last term on the right is the work done by the gravity force. By definition, this term can be written as the change of gravitational potential energy when it is carried over to the left-hand side of the balance:

$$\overline{\rho}\frac{\mathrm{D}e_g}{\mathrm{D}t}=-\overline{\rho}\mathbf{g}\cdot\mathbf{v}_c \qquad [17]$$

This relationship is demonstrated in integral form in **Appendix B**. Collecting all terms, the energy balance equation [9] is written as

$$\overline{\rho}T\frac{\mathrm{D}s}{\mathrm{D}t}+\overline{\rho}\frac{\mathrm{D}\left[e_s+e_g+e_c\right]}{\mathrm{D}t}=-\nabla\cdot\mathbf{q}+H+\psi-\nabla\cdot(\overline{p}\mathbf{v}_c)+(\cdots) \qquad [18]$$

In this equation, terms associated with convective motions are not written explicitly and will be dealt with later. Kinetic energy is also negligible and, by inspection, one may deduce from eqn [18] that

$$\overline{\rho}\frac{\mathrm{D}\left[e_s+e_g\right]}{\mathrm{D}t}=-\nabla\cdot(\overline{p}\mathbf{v}_c) \qquad [19]$$

This can be demonstrated by recalling the identity

$$\nabla\cdot(\overline{p}\mathbf{v}_c)=\overline{p}\nabla\cdot\mathbf{v}_c+\mathbf{v}_c\cdot\nabla\overline{p} \qquad [20]$$

Using the hydrostatic balance in eqn [17], the right-hand side of this equation can be recast as

$$\overline{p}\nabla\cdot\mathbf{v}_c+\mathbf{v}_c\cdot\nabla\overline{p}=-\overline{\rho}\frac{\mathrm{D}e_s}{\mathrm{D}t}-\overline{\rho}\frac{\mathrm{D}e_g}{\mathrm{D}t} \qquad [21]$$

which is indeed eqn [19].

Integrating eqn [19] over the whole planet volume, we finally obtain

$$\frac{\mathrm{d}E_g}{\mathrm{d}t}+\frac{\mathrm{d}E_s}{\mathrm{d}t}=-p_a\frac{\mathrm{d}V}{\mathrm{d}t} \qquad [22]$$

where $E_s$ is the total strain energy of the planet. The term on the right-hand side is negligible, and this equation therefore states that the change of gravitational energy is compensated by one of strain energy and does not generate heat. Contraction does lead to a small temperature increase, however, as will be shown in the succeeding text.

### 7.06.2.3 Secular Cooling Equation

To derive an equation for temperature, we need an expression for dissipation and lengthy manipulations that are given in **Appendix C**. Dissipation is balanced by the work of buoyancy forces driving convection (called the 'buoyancy flux') and disappears from the final budget, as expected. This leads to the following temperature equation:

$$\int_V\overline{\rho}C_v\frac{\partial\overline{T}}{\partial t}\mathrm{d}V=\int_V\frac{\alpha TK_T}{\rho}\frac{\partial\rho}{\partial t}\mathrm{d}V-\int_A\mathbf{q}\cdot\mathrm{d}A+\int_V H\mathrm{d}V \qquad [23]$$

where $C_v$ is thermal capacity at constant volume. The first term on the right is the only remaining contribution of contraction and has been called 'adiabatic' heating. It can be estimated as follows:

$$E_a = \int_V \frac{\alpha T K_T}{\rho}\frac{\partial \rho}{\partial t}\mathrm{d}V = -\int_V C_v \frac{\alpha K_T}{\rho C_v}\alpha T \frac{\partial T}{\partial t}\rho \mathrm{d}V$$
$$= -\int_V C_v \gamma \alpha T \frac{\partial T}{\partial t}\rho \mathrm{d}V \qquad [24]$$

where we have used the Grüneisen parameter $\gamma = (\alpha K_T/\rho C_v)$. Using the fact that $C_v$ is approximately constant (the Dulong–Petit–Debye limit for solids at high temperature), we finally obtain

$$E_a = -MC_v\langle\gamma\alpha T\rangle\frac{\mathrm{d}\langle T\rangle}{\mathrm{d}t} \qquad [25]$$

where $\mathrm{d}\langle T\rangle/\mathrm{d}t$ is the average cooling rate. Using $\gamma \approx 1.5$ and $\langle\alpha\rangle T \approx 0.03$, we find that $E_a \approx 1$ TW for a global cooling rate of 100 K Gy$^{-1}$. As will be shown in the succeeding text, this estimate of the cooling rate must be considered as an upper bound. The adiabatic heating term is smaller than the uncertainty on the energy budget and may be neglected, which leads to

$$MC_v\frac{\mathrm{d}\langle T\rangle}{\mathrm{d}t} = -\int_A \overline{q}_r \mathrm{d}A + \int_V H\mathrm{d}V \qquad [26]$$

which is the secular cooling equation. The average cooling rate lumps together the contributions of two reservoirs with very different physical properties, the mantle and the core, and must be handled with care. For this reason, the two associated energy budgets will be discussed separately.

#### 7.06.2.4 Summary

The thermodynamics of the cooling Earth involve both slow contraction and convective motions. The change of gravitational energy due to thermal contraction does not enter in the global heat budget because it is stored as strain energy. Similarly, the viscous dissipation can be important but is balanced by the bulk buoyancy flux. The secular cooling is dominated by the imbalance between radiogenic heat production and heat loss through the Earth's surface.

### 7.06.3 Heat Loss Through the Seafloor

For the purposes of calculating the rate at which the Earth is losing heat, the most direct and unbiased method is to integrate individual measurements of heat flux over the surface. As we shall see, this method fails in the oceans, and one has to use theory in order to obtain a reasonable estimate (Jaupart and Mareschal, Chapter 6.05). This approach has been criticized on the grounds that it is a theoretical one and leads to a biased result. We shall discuss this point in detail. Our present understanding of the global thermal budget of the Earth can be summarized in the map of the surface heat flux (Figure 1). It is important to remember that this map is based on the heat flux observations on the continents and their margins but that for the oceans, the surface heat flux is calculated from our best model of energy loss by the oceanic lithosphere.

#### 7.06.3.1 Oceanic Heat Flow Measurements

Heat flow through permeable rock and sediment involves two mechanisms: conduction through the solid matrix and water flow through pores and fractures into the sea. Measuring the latter directly is very costly and requires continuous recording over long timescales in order to determine a representative flow rate. The vast majority of marine heat flux determinations rely on the probe technique, such that a rigid rod carrying a thermistor chain is shoved into sediments. Determination of the temperature gradient and of the sediment thermal conductivity leads to the heat lost by conduction. Another technique is to measure temperatures in deep-sea drillholes. This is clearly the best technique because it relies on measurements over a

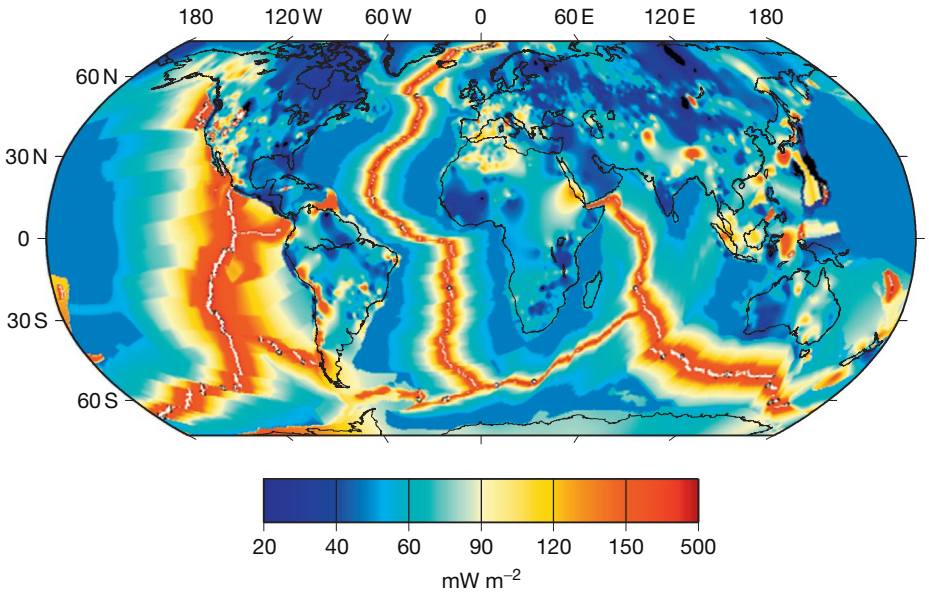


**Figure 1** Global heat flux of the Earth combining heat flux measurements on land and continental margins with a thermal model for the cooling of the oceanic lithosphere.

large depth range through poorly permeable crystalline basement, but it is particularly time-consuming. Drilling operations perturb the thermal environment greatly, implying that measurements cannot be done just after drilling is completed and require hole reentry. In addition, the number of deep-sea drillholes is too small to provide a good sampling of the seafloor. The few comparisons that have been made between the two techniques show that the shallow probe technique provides reliable results (Erickson et al., 1975). Obviously, these techniques only account for conductive heat transport, a systematic bias that has important consequences.

The extent of alteration in ophiolitic massifs shows that hydrothermal circulation is pervasive and affects large volumes of oceanic rocks (Davis and Elderfield, 2004). In situ quantitative assessment of heat transport by hydrothermal circulation can only be achieved by measuring the discharge rates and temperature anomalies of hot aqueous upwellings out of the seafloor (Ramondec et al., 2006). A single black smoker can evacuate as much as 0.1 MW (Barreyre et al., 2012), and diffuse venting through thin crack networks and bacterial mats accounts for an even larger power (Mittelstaedt et al., 2012). About 20 MW is lost to the sea through an $\approx 50 \times 50$ m region of the Lucky Strike hydrothermal field of the mid-Atlantic ridge (Mittelstaedt et al., 2012). This shows that, in hydrothermal systems, large amounts of heat loss escape conventional measurement techniques. In such systems, the vagaries of crack sealing and porosity change imply large variations of the shallow thermal structure in both time and space. It therefore does not come as a surprise that oceanic heat flux data exhibit enormous scatter (**Figure 2**). This has presented geophysicists with a major difficulty, all the more as the scatter is largest on young seafloor where the largest heat flow values are recorded.

Various methods have been used to deal with the scatter of heat flow data and the influence of hydrothermal circulation. One has been to bin data by age group in the hope that measurement errors cancel each other in a large data set, but this is not valid if measurement errors are not random, which is the case here. In the widely used compilation by Stein and Stein (1992), heat flux data have been binned in 2 My age intervals (**Figure 2**). This global data set includes a very large number of measurements with no quality assessment. Most of the early data are associated with larger errors than those of recent surveys due to small probe lengths and because thermal conductivity determinations were not made in situ. The first age bin presents a specific problem because it is characterized by the largest heat flux values as well as the most conspicuous signs of hydrothermal activity. A proper average for this age bin requires data at very young ages, $<1$ My, say, which are virtually nonexistent. Another strategy to measure the oceanic heat loss has been to seek sites with thick sedimentary cover. In crystalline basement, hydrothermal convection proceeds through cracks and generates a highly heterogeneous temperature field with narrow discrete anomalies. With a thick sedimentary cover, upwellings are slowed down and become diffuse and hence tend toward thermal equilibrium with the surrounding matrix. In this case, conduction is the dominant heat transport mechanism and conventional heat flow techniques yield reliable results. Heat flux varies spatially but the integrated value is equal to the heat extracted from the lithosphere. A reliable heat flux determination therefore requires closely spaced stations over a representative area. A third strategy has been to enhance our understanding of heat transport characteristics through young seafloor, which was done with both detailed local surveys and physical models (Davis et al., 1999; Spinelli and Harris, 2011).

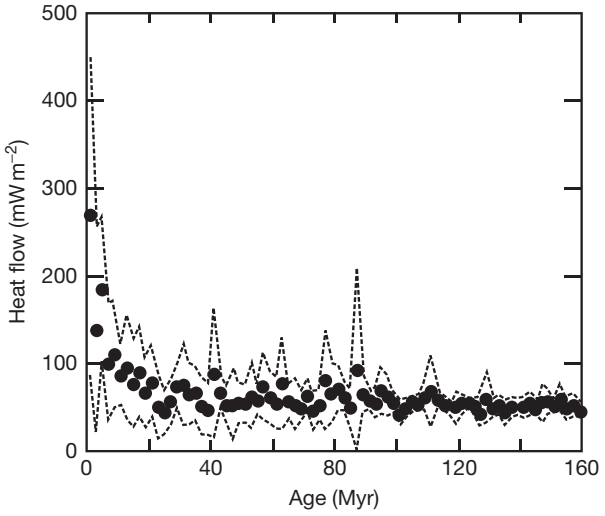


**Figure 2** Distribution of heat flux data as a function of age from the compilation by Stein and Stein (1992). Dots represent averaged heat flux values in 2 My bins. Dashed lines indicate the envelope at one standard deviation.

In summary, oceanic heat flux data are plagued by systematic errors that arise from the measurement environment and that can only be sorted out by careful small-scale local studies. There are very sound reasons that explain why heat flux data underestimate the total heat flux out of the seafloor, especially at young ages (Harris and Chapman, 2004). Using the raw data average turns a blind eye to this fundamental problem and pays no attention to the systematics of the scatter. For the purposes of calculating heat loss through the oceans, such a brute force method is not appropriate and one must instead account carefully for the specifics of the shallow oceanic environment. We shall rely on detailed heat flux surveys in selected areas and shall generalize the insights gained in this manner by comparing the data to robust thermal models for the cooling of oceanic lithosphere. We shall also evaluate the amplitude of the scatter in heat flow data using simple thermal considerations. We shall finally show how the topography of the seafloor records the amount of heat that is lost by the oceanic lithosphere.

### 7.06.3.2 Cooling of the Oceanic Lithosphere

Here, we are interested in the large-scale thermal structure and evolution of oceanic lithosphere and momentarily ignore the complexities of the shallow environment. The heat equation provides the basic framework

$$\rho C_p \frac{DT}{Dt} = \rho C_p \left( \frac{\partial T}{\partial t} + \mathbf{v} \cdot \nabla T \right) = \nabla \cdot (\lambda \nabla T) \qquad [27]$$

where $C_p$ is the heat capacity, $\rho$ is the density of the lithosphere, $\lambda$ is thermal conductivity, and $\mathbf{v}$ is the velocity of the plate. We have neglected radiogenic heat production, which is very small in

the oceanic crust and in mantle rocks (see succeeding text), and viscous heat dissipation. Over the temperature range of interest here, variations of heat capacity amount to ±20%. Such subtleties will be neglected momentarily for the sake of clarity and simplicity. They must be taken into account, however, for accurate calculations (McKenzie et al., 2005). In the upper boundary layer of a convection cell (see **Chapter 7.04**), vertical advective heat transport is negligible. Over the large horizontal distances involved, vertical temperature gradients are much larger than horizontal ones, except in the immediate vicinity of the ridge axis, and one may neglect horizontal diffusion of heat. The validity of this standard boundary layer approximation was verified by Sclater et al. (1980), who found that calculations with and without horizontal heat diffusion could not be distinguished from one another at ages larger than 1 My.

It is best to work in a reference frame that moves with the plate (i.e., a Lagrangian approach). Over the lifetime of an oceanic plate, secular cooling may be safely neglected so that temperature can be written as a function of age, noted $\tau$, instead of time. For negligible horizontal heat transport, the heat eqn [27] can be reduced to

$$\frac{\partial T}{\partial \tau} = \kappa \frac{\partial^2 T}{\partial z^2} \qquad [28]$$

where $\kappa$ is thermal diffusivity. This is the one-dimensional heat diffusion equation, whose solution requires a set of initial and boundary conditions. The initial condition requires specification of the thermal structure of an oceanic spreading center. For the top boundary condition, one must in principle account for thermal conditions in the shallow oceanic environment. The bottom boundary condition depends on the efficacy of heat transport in the asthenosphere. All these conditions are only approximations to more complex realities and must be evaluated carefully.

#### 7.06.3.2.1 The shallow oceanic environment

The upper part of young oceanic lithosphere is made of fractured crust allowing pervasive water circulation, which is not accounted for in the heat eqn [27]. An exact solution must deal with different environments and involve a host of parameters that are not known precisely and vary with time, such as permeability, which decreases as fractures and pores get clogged by precipitates from the highly charged solutions that circulate through them. Fortunately, several facts conspire to dramatically reduce the impact of water circulation on bulk lithospheric cooling.

Hydrothermal convection in the oceanic crust is self-defeating and becomes inefficient after about 0.1 My (Dunn et al., 2000; McLennan et al., 2005; Spinelli and Harris, 2011). The end result is cold oceanic crust sitting on basement that has not had time to lose much heat by conduction. After this initial transient, the cold crust heats up against the hotter basement by diffusion and temperatures in both crust and basement adjust to a profile resembling that of steady conductive cooling from $\tau = 0$. On the ridge flanks, away from the axial hydrothermal zone, the highly permeable pillow lava layer at the top of the crust hosts strong lateral water flow (Davis and Elderfield, 2004) that effectively smoothes out thermal anomalies and imposes a nearly constant and uniform temperature. Below this aquifer, heat conduction is the dominant process, save for isolated deep open fractures. Fluid-driven cooling therefore proceeds in two different phases, with deep convection in large parts of the crust followed by superficial circulation in a thin aquifer. Only the first phase is significant for the large-scale heat budget of the lithosphere, but it has a prolonged influence on the shallow lithospheric thermal structure due to the slowness of diffusive relaxation. It may leave its imprint on the surface heat flux for as long as 10 My depending on the thickness affected by axial hydrothermal convection (Spinelli and Harris, 2011).

What has been achieved by hydrothermal convection at the ridge axis is rapid heat extraction out of the crust at the top of the lithosphere, and this could be taken as an initial condition for the conduction cooling model. The vagaries of convection, fracturing, and sealing in the crust and of sedimentation in a ridge environment with irregular topography prevent a universally valid axial temperature structure, however, and the preferred approach has been to use a 'reference' conduction model with simple boundary and initial conditions. We shall see that this allows an excellent fit to various types of data. Departures from model predictions can be calculated, observed, and included in an error analysis.

Due to the high efficacy of heat transport in seawater, the seafloor is at a fixed temperature of about 4 °C (in practice 0 °C for convenience), which provides an upper boundary condition.

#### 7.06.3.2.2 Initial condition: Temperature distribution at the ridge axis

To specify the temperature profile at the ridge axis, which provides the initial condition for the cooling model, two effects come into play. Mantle that rises toward the oceanic ridge undergoes pressure release and partial melting, which absorbs latent heat. This mantle is hotter than its surroundings and loses heat laterally by diffusion. During isentropic ascent of dry mantle, temperature decreases by about 200 K (McKenzie and Bickle, 1988), which is small relative to the temperature contrast at the top of the oceanic plate (≈1350 K). Thus, it is commonly assumed that the axial temperature does not vary with depth and is equal to a constant value noted $T_M$. Calculations based on a realistic temperature profile lead to minor differences (McKenzie et al., 2005). One problem with these temperature profiles is that they specify a finite temperature drop at the surface at $\tau = 0$, implying that the surface heat flux diverges as $\tau \to 0$. This problem disappears if one specifies that the heat that is advected vertically by the upwelling mantle at the ridge is lost by horizontal conduction to the adjacent oceanic plate (Davis and Lister, 1974). In this modified model, the heat flux is finite at the ridge but differs significantly from the previous model only for ages $< 1$ My (Sclater et al., 1980). For determining the heat loss, such differences are of no consequence: heat flux integrated over finite areas remains bounded regardless of the initial condition and is very weakly sensitive to the choice of initial condition (Sclater et al., 1980).

#### 7.06.3.2.3 Bottom boundary condition

The simplest model, called the 'half-space' model, has the lower boundary at infinite depth and assumes that temperature remains finite, such that cooling proceeds unhampered over the entire age span of oceanic lithosphere. For the reference

upper boundary condition, such that $T(z=0)=0$, the temperature distribution is then

$$T(z,\tau)=T_{\mathrm{M}}\,\mathrm{erf}\left(\frac{z}{2\sqrt{\kappa\tau}}\right)=\frac{2T_{\mathrm{M}}}{\sqrt{\pi}}\int_0^{z/2\sqrt{\kappa\tau}}\exp\left(-\eta^2\right)\mathrm{d}\eta \qquad [29]$$

for which the surface heat flux is

$$q(0,\tau)=\frac{\lambda T_{\mathrm{M}}}{\sqrt{\pi\kappa\tau}}=C_{\mathrm{Q}}\tau^{-1/2} \qquad [30]$$

where $C_{\mathrm{Q}}$ is a constant. This equation makes the very simple prediction that heat flux varies as $\tau^{-1/2}$. One remarkable feature is that this relationship holds for arbitrary temperature-dependent physical properties (Carslaw and Jaeger, 1959; Lister, 1977) (**Appendix D**). Numerical models of mantle convection that are in a platelike regime conform very well to this relationship. **Figure 3** displays a snapshot of the temperature field and surface observables in such a model, from Grigné et al. (2005). One sees clearly that the horizontal velocity at the surface is piecewise constant, defining plates, and that the heat flux decreases with distance $x$ from ridges as $1/\sqrt{x}$, that is to say $\tau^{-1/2}$ for a constant velocity. We shall see that the value for the mantle temperature $T_{\mathrm{M}}$ remains subject to some uncertainty. The value of the constant $C_{\mathrm{Q}}$ in eqn [30], however, may be determined empirically from the data, as will be shown later.

In the other class of models, a boundary condition is applied at some depth, which marks the base of the 'plate.' In principle, one should solve for heat supply from the asthenosphere. However, this requires elaborate physical models of mantle convection relying on specific choices of material properties and simplifying assumptions. For the sake of simplicity, one may consider two simple end-member cases, such that temperature or heat flux is constant at the base of the plate. Both these boundary conditions are approximations. For example, the fixed temperature boundary condition requires infinite thermal efficiency for heat exchange between the plate and the mantle.

The choice of the proper basal boundary condition is important because it determines the relationship between the relaxation time and the plate thickness. For plate thickness $a$, the diffusion relaxation time scales with $a^2/\kappa$ with a proportionality constant that depends on the bottom boundary condition. Specifically, the thermal relaxation time of a plate is four times as long for fixed heat flux at the base than it is for fixed temperature. Thus, for the same relaxation time, a plate with a fixed basal temperature is twice as thick as one with a fixed basal heat flux. For short times, the cooling rate (i.e., the surface heat flux) does not depend on the lower boundary condition and, for both types of plates, it is the same as the heat flux for the cooling half-space. The details are provided in **Appendix E**. Thus, it is better to use a half-space model for young ages because it relies on a reduced set of hypotheses and because it does fit the oceanic data, as will be shown later. Furthermore, it has been tested over and over again and forms the basis for scaling laws of convective heat flux in many different configurations (Howard, 1964; Olson, 1987; Turcotte and Oxburgh, 1967). This simple model breaks down at ages larger than about 80 My for reasons that are still debated. For this reason, it may be wise not to rely on a specific physical model, such as that of a plate. For ages >80 My, we do not need a theoretical cooling model to calculate the oceanic heat loss because the data scatter is small. For this second phase of lithospheric evolution, the heat flux is approximately constant (see succeeding text), indicating that heat is supplied to the base of the oceanic lithosphere and that thermal steady state is nearly achieved.

One final worry is that oceanic ridges and oceanic plates drift over mantle that may not be thermally well mixed, which could be responsible for a bottom boundary condition that varies with age. A detailed study of oceanic tholeiitic basalts, however, demonstrates that their composition, and hence the temperature of the mantle from which they were derived, has not changed significantly for about 80 My (Humler et al., 1999).

### 7.06.3.3 Validating the Cooling Model for Oceanic Lithosphere

#### *7.06.3.3.1 High-resolution surveys near mid-ocean ridges*

A very detailed heat flux survey on young seafloor near the Juan de Fuca Ridge was conducted by Davis et al. (1999) with three specific goals: to evaluate the intensity and characteristics of hydrothermal circulation, assess local thermal perturbations due to basement irregular topography, and test cooling models for the lithosphere. **Figure 4** shows the salient results. Direct observation of the seafloor shows that the basement outcrop region is a zone of recharge and that, beneath the sedimentary cover, water flow is dominantly horizontal. Focused discharge occurs at a few locations in association with basement

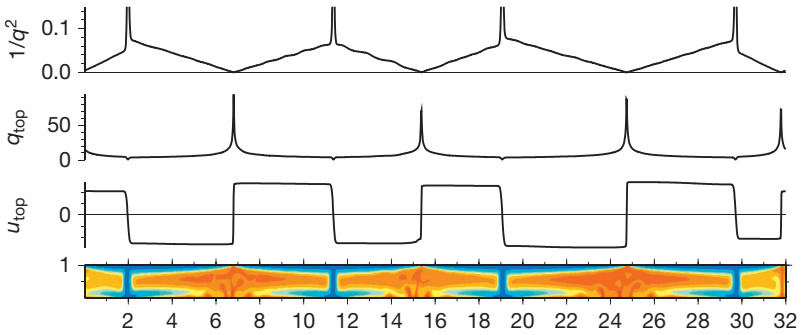


**Figure 3** Snapshot of temperature, surface velocity ($u_{\mathrm{top}}$), heat flux ($q$), and pseudo age ($1/q^2$) in a numerical convection model with self-consistent plate tectonics (Grigné et al., 2005). See **Appendix H** for details. Note that the pseudo age varies linearly as function of distance to the ridge, which is consistent with the $\tau^{-1/2}$ heat flux law for young oceanic lithosphere.

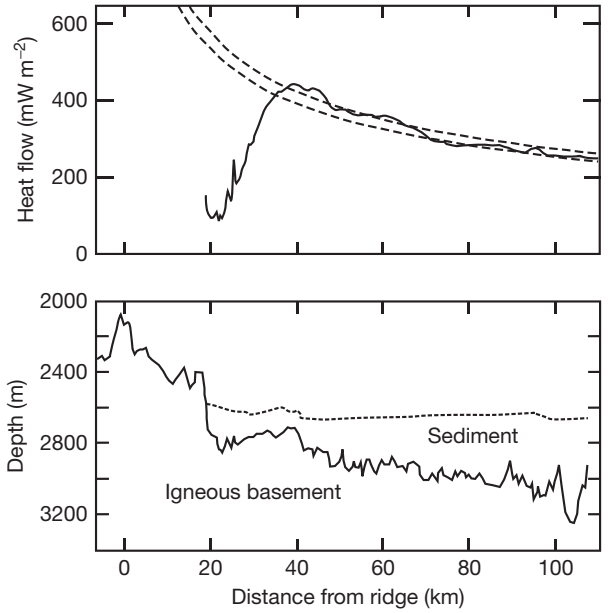


**Figure 4** High-resolution heat flux profile near the Juan de Fuca Ridge from Davis et al. (1999). Dashed lines stand for two predictions of the half-space cooling model with constant $C_Q$ in the $\tau^{-1/2}$ heat flux–age relationship equal to 470 and 510 (with heat flux in mW m$^{-2}$ and age in My).

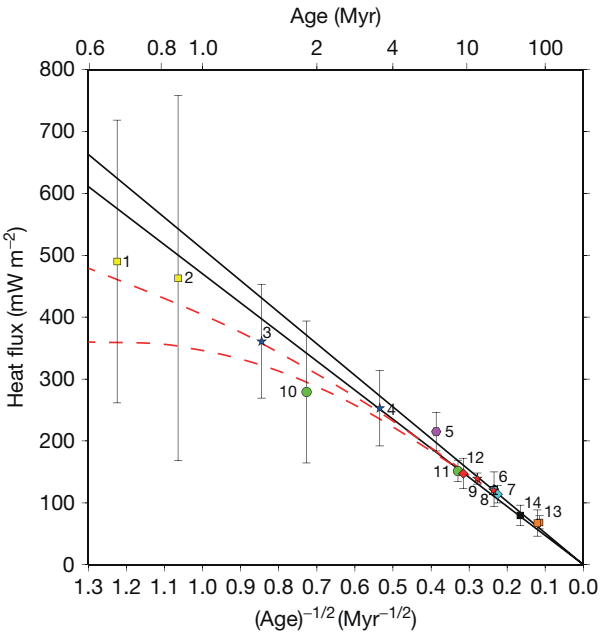


**Figure 5** Heat flow versus age for selected sites with a sediment blanket. 1–2: Galápagos Spreading Center (Williams et al., 1974); 3–4: Juan de Fuca Ridge (Hasterok et al., 2011); 5: Costa Rica Rift (Hasterok et al., 2011); 6–7: Cocos Plate (Hasterok et al., 2011); 8–9: the Gulf of Aden (Cochran, 1981; Lucazeau et al., 2010); 10–11 East Pacific Rise (Villinger et al., 2002); 12: south Azores (Lucazeau et al., 2006); 13: Mascarene basin (Bonneville et al., 1997); 14: Reykjanes Ridge (Sclater and Crowe, 1979). Several sites (1, 2, 3, and 10) deviate from the conductive cooling trend, which can be explained by thermal relaxation of the initial thermal structure at the ridge inherited from pervasive hydrothermal convection in the crust. Dashed red curves represent the predictions of models of hydrothermal convection in fast spreading centers extending to depths of 2 and 6 km (Spinelli and Harris, 2011).

topographic highs. Elsewhere, water flow is diffuse, such that it equilibrates with the sediments.

At the Juan de Fuca Ridge site, the heat flux fluctuates on the scale of station spacing (2 km), which implies that surveys with coarser spatial resolution do not yield meaningful results. To emphasize the long-wavelength trends, a 15 km running average was applied on the heat flux profile. This profile shows two distinct trends: near the basement outcrop, to the left, the heat flux increases with age and reaches a maximum value in excess of 400 mW m$^{-2}$, and further away from the outcrop, the heat flux decreases with age. In the latter region, the total heat flux variation is large enough to allow comparison with theoretical models for the cooling of oceanic lithosphere. The data conform to the $\tau^{-1/2}$ relationship and indicate that constant $C_Q$ in eqn [30] is between 470 and 510 (with heat flux in mW m$^{-2}$ and age in My).

### 7.06.3.3.2 Global analysis

The local Juan de Fuca Ridge survey can be corroborated independently using filtered heat flow data over larger age ranges. Hasterok et al. (2011) used a revised heat flow database with more than 15 000 oceanic values and selected sites located >60 km from the nearest seamount where the sediment cover is >400 m. These data exhibit a well-defined correlation with the age of the seafloor but remain scattered.

For better results, we focus on 14 sites with thick sedimentary cover and dense heat flow sampling (Figure 5). For those sites, hydrothermal circulation that may still be active in the igneous basement is effectively sealed off by the hydraulically resistive sedimentary cover. There are no localized discharge zones and the average heat flux is equal to the rate at which the basement loses energy. The data conform to the $\tau^{-1/2}$ relationship between 3 and 80 My. In order to determine the best-fit coefficient, we add the constraint that the heat flux tends to zero as age tends to infinity and find that $C_Q = 490$, close to the value for the Juan de Fuca Ridge. For ages <3 My, the measurements are more dispersed and site-averaged values fall below the simple cooling model. This can be explained by the conductive relaxation of the anomalous thermal structure generated by hydrothermal convection in the axial zone. We show in Figure 5 calculated values from the model of Spinelli and Harris (2011), which account nicely for the data.

Combining the local Juan de Fuca Ridge survey and the global data set of reliable heat flux sites, we conclude that $C_Q = 490 \pm 20$, with an uncertainty of ±4%. Table 3 compares the various estimates that have been used in the past. The heat loss estimate of Pollack et al. (1993) was based on $C_Q = 510$, which is clearly an upper bound. This value was taken from the analysis of Stein and Stein (1992), which was based on the plate model with constant basal temperature. One feature of this model is that $T_M = 1725$ K, a high value that is not consistent with the average ridge axis temperature derived from the compositions of mid-ocean ridge basalts (MORBs) (Kinzler and Grove, 1992) (Table 4).

The $\tau^{-1/2}$ relationship is based on sound physics and holds for conductive cooling models at early times, including those

**Table 3** Estimates of the continental and oceanic heat flux and global heat loss

| | *Continental (mW m$^{-2}$)* | *Oceanic (mW m$^{-2}$)* | *Total (TW)* |
|---|---|---|---|
| Williams and von Herzen (1974) | 61 | 93 | 43 |
| Davies (1980a,b) | 55 | 95 | 41 |
| Sclater et al. (1980) | 57 | 99 | 42 |
| Pollack et al. (1993) | 65 | 101 | 44 |
| Davies and Davies (2010) | 71 | 105 | 47 |
| This study[a] | 65 | 94 | 46 |

[a]The average oceanic heat flux does not include the contribution of hot spots. The total heat loss estimate does include 3 TW from oceanic hot spots.

**Table 4** Potential temperature of the oceanic upper mantle

| | *Reference* | *Method* |
|---|---|---|
| 1333 °C[a] | Parsons and Sclater (1977) | Average depth + heat flux |
| 1450 °C[a] | Stein and Stein (1992) | Average depth + heat flux |
| 1300–1370 °C[a] | Carlson and Johnson (1994) | True basement depth (DSDP) |
| 1315 °C[a] | McKenzie et al. (2005) | Depth + heat flux with $\lambda$(T), $C_p$(T) and $\alpha$(T) |
| 1280 °C[a] | McKenzie and Bickle (1988) | Average basalt composition |
| 1315–1475 °C[a] | Kinzler and Grove (1992) | Basalt composition |
| 1275–1375 °C[a] | Katsura et al. (2004) | Isentropic profile through the Ol–Wa phase change |
| 1454 ± 81 °C | Putirka et al. (2007) | Olivine–liquid equilibriums |

[a]Temperature estimate for a cooling model with constant temperature below the ridge axis (i.e., which does not account for isentropic decompression melting).

for a plate of fixed thickness. This relationship provides a good fit to the data and we shall use it for the 3–80 My age range. For ages $<3$ My, this relationship breaks down for the global data set but is still valid in some areas (**Figure 4**). We shall still use it and calculate the associated uncertainty. For ages $>80$ My, we shall simply use a constant heat flux as the data indicate that $q_{80} \approx 48$ mW m$^{-2}$ (Lister et al., 1990) (**Figure 6**).

### 7.06.3.3.3 Depth of the seafloor

The variation of ocean floor depth with age provides an additional constraint on lithospheric cooling at the cost of introducing a new physical property, the coefficient of thermal expansion. As for heat flow, depth data are highly scattered due to intrinsic seafloor roughness, the presence of seamounts, and a variable sediment cover. Coping with the noisy data set has involved again either binning of the data (Parsons and Sclater, 1977) or rejecting 'anomalous' sites (Crosby and McKenzie, 2009; Crough, 1983; Hillier and Watts, 2005; Korenaga and Korenaga, 2008). Analyzing seafloor subsidence in detail would be outside the scope of this chapter and we only seek confirmation for the two main features of lithospheric evolution that are used here: the $\tau^{-1/2}$ heat

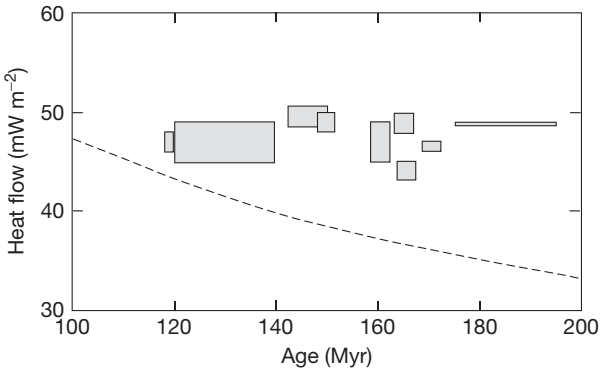


**Figure 6** Heat flux data and prediction of the half-space cooling model for ages larger than 100 My. Reproduced from Lister CRB, Sclater JG, Nagihara S, Davis EE, and Villinger H (1990) Heat flow maintained in ocean basins of great age – Investigations in the north-equatorial West Pacific. *Geophysical Journal International* 102: 603–630.

flux–age dependence up to 80 My and the interrupted cooling at later ages.

An isostatic balance condition leads to a very simple equation for subsidence with respect to the ridge axis (Sclater and Francheteau, 1970):

$$\begin{aligned}\Delta h(\tau) &= h(\tau) - h(0) \\ &= \frac{1}{\rho_m - \rho_w}\int_0^d (\rho[T(z,\tau)] - \rho[T(z,0)])\mathrm{d}z\end{aligned} \quad [31]$$

where $h(\tau)$ and $\Delta h(\tau)$ are the depth of the ocean floor and subsidence at age $\tau$ and where $\rho_m$ and $\rho_w$ denote the densities of mantle rocks at temperature $T_M$ and water, respectively. In this equation, $d$ is some reference depth in the mantle below the thermal boundary layer. This equation neglects the vertical normal stress at depth $d$, which may be significant only above the mantle upwelling structure, that is, near the ridge axis. We are interested in the heat flux out of the seafloor, $q(0,\tau)$. Assuming for simplicity that the coefficient of thermal expansion $\alpha$ is constant, the equation of state for near-surface conditions is

$$\rho(T) = \rho_m[1 - \alpha(T - T_M)] \quad [32]$$

From the isostatic balance equation [31], we obtain

$$\begin{aligned}\frac{\mathrm{d}h}{\mathrm{d}\tau} &= \frac{-\alpha\rho_m}{\rho_m - \rho_w}\frac{\mathrm{d}}{\mathrm{d}\tau}\left[\int_0^d T(z,\tau)\mathrm{d}z\right] \\ &= \frac{-\alpha}{C_p(\rho_m - \rho_w)}\frac{\mathrm{d}}{\mathrm{d}\tau}\left[\int_0^d \rho_m C_p T(z,\tau)\mathrm{d}z\right]\end{aligned} \quad [33]$$

where we have also assumed that $C_p$ is constant. Heat balance over a vertical column of mantle between $z=0$ and $z=d$ implies that

$$\frac{\mathrm{d}h}{\mathrm{d}\tau} = \frac{\alpha}{C_p(\rho_m - \rho_w)}[q(0,\tau) - q(d,\tau)] \quad [34]$$

which states that thermal contraction reflects the net heat loss between the surface and depth $d$. Because $q(0,\tau)$ depends on $T_M$, the subsidence rate also depends on the initial temperature at the ridge axis. This equation states that the surface heat flux is the sum of heat flux at depth $d$ and the amount of cooling over vertical extent $d$. Using only the latter therefore leads to an underestimate of the surface heat flux.

Carlson and Johnson (1994) investigated these theoretical predictions using the best data set, basement depths from deep-sea drillholes, which require no correction for sediment thickness. The data are consistent with the half-space cooling model up to an age of about 80 My and indicate that the rate of subsidence decreases markedly at later ages. In its simplest formulation with constant physical properties and a constant temperature beneath the ridge, the plate model does not allow a good fit to the data. Using the best-fit parameters deduced from subsidence data and estimates for the various physical properties of mantle rocks in eqn [34] (i.e., for $\alpha$, $C_p$, and the densities), Carlson and Johnson (1994) predicted heat flux values that were consistent with reliable heat flux data. For ages $<80$ My, the best-fit depth versus age relationship is

$$h(\tau) = (2600 \pm 20) + (345 \pm 3)\tau^{1/2}, \text{with } h \text{ in meters and } \tau \text{ in My} \quad [35]$$

From this relationship, the predicted heat flux over the same age range is

$$q(0, \tau) = (480 \pm 4)\tau^{-1/2}, \text{with } q \text{ in mW m}^{-2} \text{ and } \tau \text{ in My} \quad [36]$$

We shall return to these estimates later. Using the same physical properties, Carlson and Johnson (1994) found that fitting the depth data with the plate model and half-space model leads to different values for the average ridge axis temperature $T_M$: 1470 and 1370 °C, respectively.

Many authors have debated on how 'normal' seafloor subsides using various filtering techniques and by winnowing data from seamounts and other anomalous areas. The major issue was whether or not the data truly indicate flattening of the seafloor for ages larger than 80–100 My (Crough, 1983; Korenaga and Korenaga, 2008). Recent work has established that flattening does occur (Crosby and McKenzie, 2009; Hillier, 2010; Hillier and Watts, 2005). For our present purposes, this is important because it confirms what is indicated by heat flow data: after about 80 My, cooling of the oceanic lithosphere slows down markedly, and thermal steady state gets established due to heat supply from the asthenosphere.

### 7.06.3.4 Heat Loss Through the Ocean Floor

Simple physical considerations demonstrate that seafloor topography and surface heat flux record the same phenomenon and furthermore that the subsidence rate is proportional to surface heat flux for as long as 80 My. In contrast, the raw oceanic heat flux data set records the conductive heat flux through a heterogeneous permeable superficial sedimentary layer. Using this data set leaves the seafloor topography unexplained.

The plate model with fixed basal temperature has been used to calculate the total oceanic heat loss by several authors (Hasterok, 2013; Pollack et al., 1993; Sclater et al., 1980; Stein and Stein, 1992). Its advantage is that it provides a function that fits noisy data over the whole range of ages. We shall not follow this approach for two reasons. One is that the plate model is only an approximation of the physics involved. Maintaining a constant temperature at a fixed depth requires infinitely efficient heat exchange between lithosphere and asthenosphere and a mechanism that maintains the plate thickness. Another reason is that the plate model depends on parameters such as the plate thickness and axial ridge temperature that are determined a posteriori by a best fit to the data. This procedure may introduce trade-offs such that, for example, data at old ages steer model predictions away from data at younger ages. We prefer to stay as close to the data as possible with as few hypotheses as possible. To calculate the total rate of oceanic heat loss, we separate the data in two different age intervals: 0–80 My, where the $\tau^{-1/2}$ law holds, and older seafloor where heat flux data depart from the half-space model. For seafloor older than 80 My, the heat flux is approximately constant $q_{80} \approx 48\,\text{mW m}^{-2}$ (Lister et al., 1990) (**Figure 6**). Deviations from this value are $\leq 3\,\text{mW m}^{-2}$ and exhibit no systematic age trend. The mean is determined with an uncertainty of $1\,\text{mW m}^{-2}$, which represents 1% of the average oceanic heat flux. This has negligible impact on the total heat loss estimate, which is dominated by the young seafloor contribution. We also use bathymetry data for seafloor younger than 80 My but not for older ages. We add the contribution of marginal basins that follow the standard oceanic heat flux model, as demonstrated by Sclater et al. (1980). Continental margins, passive or active, are transition zones between continents and oceans and are treated in the continental section.

#### 7.06.3.4.1 Global oceanic heat loss calculation

Heat loss through the ocean floor is equal to

$$Q_0 = \int_0^{\tau_{max}} q(0, \tau) \frac{dA}{d\tau} d\tau \quad [37]$$

where $A(\tau)$ is the distribution of seafloor with age, which can be deduced from maps of the ocean floor (Müller et al., 1997, 2008; Royer et al., 1992; Sclater et al., 1980). Using the data sets of Royer et al. (1992) and Müller et al. (1997), Rowley (2002) and Cogné and Humler (2004) found that a simple linear relationship provides a good fit to the data (**Figure 7**), confirming the earlier result of Sclater et al. (1980):

$$\frac{dA_1}{d\tau} = C_A(1 - \tau/\tau_m) \quad [38]$$

These three different groups of authors agree that $\tau_m = 180$ My but quote slightly different values of the coefficient $C_A$: $3.45\,\text{km}^2\,\text{year}^{-1}$ for Sclater et al. (1980), $2.96\,\text{km}^2\,\text{year}^{-1}$ for Rowley (2002), and $2.85\,\text{km}^2\,\text{year}^{-1}$ for Cogné and Humler (2004). The high estimate of Sclater et al. (1980) is due to the inclusion of marginal basins, which contribute $\approx 0.38\,\text{km}^2\,\text{year}^{-1}$ to the global accretion rate. The small difference of about $0.12\,\text{km}^2\,\text{year}^{-1}$ (4%) between the more recent estimates of Rowley (2002) and Cogné and Humler (2004) arises from the different methods used to fit the data. One independent constraint is brought by the total area of ocean floor, which is sensitive to the exact location of the continent–ocean boundary. A detailed analysis of continental margins leads to a total continental area of $210 \times 10^6\,\text{km}^2$ (Cogley, 1984) (see **Table 5**). From this, the total seafloor surface is $300 \times 10^6\,\text{km}^2$, slightly less than the value used by Sclater et al. (1980). For a triangular age distribution with a maximum age $\tau_m = 180$ My, this implies that $C_A = 3.34\,\text{km}^2\,\text{year}^{-1}$. Subtracting the contribution of marginal basins, this corresponds exactly to the Rowley (2002) estimate. Thus, for our purposes, we shall use $C_A = 3.34\,\text{km}^2\,\text{year}^{-1}$. This discussion illustrates that uncertainties may come from unexpected variables, the area of the

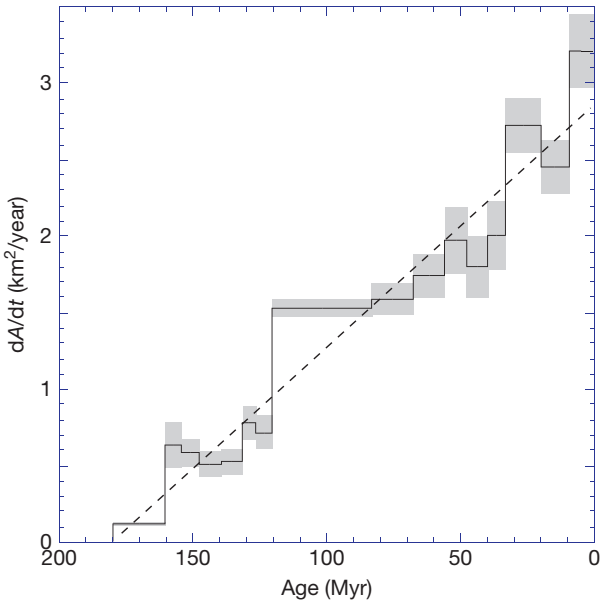


**Figure 7** Distribution of seafloor ages. The dashed line is the best-fit linear function. Modified from Cogné J-P and Humler E (2004) Temporal variation of oceanic spreading and crustal production rates during the last 180 My. *Earth and Planetary Science Letters* 227: 427–439.

**Table 5** Surface area and heat flux in oceans and continents

| | *Area* | *Total heat flux* |
|---|---|---|
| *Oceans* | | |
| Oceanic | $273 \times 10^6 km^2$ | |
| Marginal basins | $27 \times 10^6 km^2$ | |
| Total oceans | $300 \times 10^6 km^2$ | 32 TW |
| *Continents* | | |
| Precambrian | $95 \times 10^6 km^2$ | |
| Paleozoic | $23 \times 10^6 km^2$ | |
| Stable continents | $118 \times 10^6 km^2$ | |
| Active continental | $30 \times 10^6 km^2$ | |
| Submerged (margins and basins) | $62 \times 10^6 km^2$ | |
| Total continental | $210 \times 10^6 km^2$ | 14 TW |

seafloor in this particular instance. The continental heat flux budget must account for the remaining $210 \times 10^6 km^2$ (Table 5).

Integrating separately seafloor younger and older than 80 My gives

$$Q_{80-} = \int_0^{80} C_Q \tau^{-1/2} C_A (1 - \tau/180) d\tau = 24.3 TW \quad [39]$$

$$Q_{80+} = q_{80} \int_{80}^{180} C_A (1 - \tau/180) dt' = 4.4 TW \quad [40]$$

$$Q_{oceans} = 29 \pm 1 TW \quad [41]$$

where the uncertainty comes mostly from that on coefficient $C_Q$. The present estimate is slightly less than earlier estimates because of the slightly lower ridge temperature (or equivalently, the slightly smaller value of coefficient $C_Q$ in the heat flux vs. age relationship) and because of the revised estimate for the mean accretion rate at zero age $C_A$. For $C_Q = 510 mW m^{-2} My^{-1/2}$ and $C_A = 3.45 km^2 year^{-1}$, the heat loss would be 31 TW. In an independent study, Hasterok (2013) relied on a 'heat flow calibrated plate model' and obtained 29.4 TW, which is identical to our result.

For young ages, the bathymetry provides a direct measure of the heat lost by the cooling plate. We obtain another heat loss estimate with the following equation:

$$Q(80-) = \frac{C_p}{\alpha}(\rho_m - \rho_w) \int_0^{80} \frac{dh}{d\tau} \frac{dA(\tau)}{d\tau} d\tau \quad [42]$$

$$\approx 24 TW \quad [43]$$

which is formally identical to the heat flux equation above and where $\rho_m = 3300 kg m^{-3}$, $C_p = 10^3 J kg^{-1} K^{-1}$, and $\alpha = 3 \times 10^{-5} K^{-1}$. In old basins, where the heat flux $\approx 48 mW m^{-2}$, the bathymetry is almost flat and cannot be used to estimate the rate of heat loss.

Uncertainties on the oceanic heat loss come from three sources other than that on the coefficient $C_Q$. One source is the uncertainty on the age distribution and the total area of ocean floor or, more precisely, the total area of continental shelves. The latter is $<3\%$ and implies an even lower uncertainty on the global heat loss because a change in the area of oceans is compensated by a change in the area of continents. Considering the difference between the average oceanic heat flux and continental heat flux, the resulting uncertainty on the global heat loss estimate is only 1%. The impact of departures from the triangular age distribution is best assessed by comparing the heat loss estimate derived from eqn [37] and that obtained by adding the individual contributions of each age group. Parsons (1982) showed that this difference amounts to about 0.3% of the total, which may be considered negligible. As we shall see later on, however, evaluating the uncertainty on the age distribution must be done over a large timescale and involves consideration of the stability of the mantle convection planform. The two other sources of uncertainty are discussed next and involve the thermal regime of young seafloor, which is not captured accurately by the conductive cooling model, and the contribution of hot spots.

#### 7.06.3.4.2 Heat loss through young ocean floor

The conductive cooling model is vindicated for ages older than 3 My by a global data set of reliable heat flux determinations and on younger seafloor by local surveys with small station spacing and favorable environmental conditions. It is not valid for many areas of the seafloor that are younger than 3 My and particularly for axial hydrothermal zones, however, because it does not account for ridge processes. Yet it is within that age interval that the heat flux is highest, and we evaluate the consequences for heat loss estimates. We cannot determine precisely the error because this would require models for all the different axial hydrothermal zones that exist in the world's oceans. Instead, we compare two different estimates of the energy that is lost to the sea in 3 My through a unit area of seafloor. The estimate from the conductive cooling model is $\approx 55 \times 10^{12} J m^{-2}$. For the other estimate, we consider the two independent processes that produce the cooling of young oceanic lithosphere. For hydrothermal convection at the ridge, an upper bound is obtained by considering that the whole crust

gets cooled to the sea temperature. For a 6 km thick crust, this represents $\approx 25 \times 10^{12}\,\mathrm{J\,m^{-2}}$. After this very short-lived phase, conductive cooling is recorded by reliable heat flux measurements on ridge flanks (Figure 5). Over 3 My, these data account for $\approx 40 \times 10^{12}\,\mathrm{J\,m^{-2}}$. Adding these two components leads to $\approx 65 \times 10^{12}\,\mathrm{J\,m^{-2}}$, about 18% higher than the conductive model. This represents the upper bound for the uncertainty. The 0–3 My age range accounts for 18% of the total oceanic heat loss, implying that the final error on the total heat loss estimate is $< 3\%$.

#### 7.06.3.4.3 Hot spots

The oceanic heat loss estimate relies on a thermal model that specifies explicitly that the oceanic lithosphere cools by conduction over a well-mixed asthenosphere. This ignores the contribution of isolated hot spots that are the surface expressions of localized mantle upwellings with temperatures that are above those of the well-mixed mantle. Theoretical physical models show that, beneath a moving plate, plume material gets deflected by the ambient mantle flow and spreads at the base of the lithosphere. Thus, the magnitude of the heat flux perturbation at the base of the plate is smaller than that for a vertical plume rising through a static fluid (Olson, 1990; Ribe and Christensen, 1994). The thermal anomaly propagates by diffusion to the top of the plate in a time that depends on the plate thickness and on the extent of plume penetration (i.e., the amount of plate thinning). Given the scatter inherent in oceanic measurements, it is not surprising that heat flux anomalies over hot spot tracks have been elusive. Bonneville et al. (1997) had shown that dense station spacings are required to isolate a meaningful signal from shallow topographic effects and the influence of water circulation. They did find that the Reunion hot spot track was an area of enhanced heat flux, corroborating the earlier findings of Courtney and White (1986) over the Cape Verde Rise. Faced once again with the shortcomings of raw heat flux data, one has had to resort to indirect methods. The heat flux from hot spots has been estimated from the buoyancy of bathymetric swells (Davies, 1988; Sleep, 1990). These estimates are in the range 2–4 TW and are added to the heat loss due to plate cooling.

The hot spot contribution must be handled with care as some mantle plumes may not penetrate the oceanic lithosphere over large vertical distances and may only heat up a thin basal region. In this case, the induced thermal anomaly remains 'locked' within the lithosphere with no surface heat flux expression. The heated region returns with the plate into the mantle in subduction zones and contributes no net heat loss.

### 7.06.3.5 Summary

Heat loss through the ocean floor cannot be determined using the raw heat flux data set that includes many measurements that are affected by hydrothermal circulation and irregularities of the sediment cover. For ages in the 3–80 My range, predictions of the 'half-space' model for the cooling of the lithosphere can be compared successfully to measurements in selected environments where the effects of hydrothermal circulation can be assessed and accounted for. This model implies values for the mantle temperature beneath mid-ocean ridges that are consistent with independent petrologic models for basalt genesis. Finally, it is consistent with the evolution of seafloor bathymetry that the raw heat flux data leave unaccounted for. The heat loss estimate requires an accurate areal distribution of seafloor ages. Uncertainty in the end result is essentially due to errors on the extent of continental margins. Accounting for the various uncertainties involved, the present-day rate of heat loss through the ocean floor is $32 \pm 2$ TW. This estimate includes the enhanced heat flux over hot spots.

## 7.06.4 Heat Loss Through Continents

### 7.06.4.1 Average Continental Heat flux and Heat Loss Through Continental Areas

There are more than 35 000 heat flux measurements over the continents and their margins, including measurements made in oil wells. Large areas (Antarctica, Greenland, parts of the shields in Brazil, and Africa) have almost no data. The raw average of all the continental heat flux values is $80\,\mathrm{mW\,m^{-2}}$ (Table 6, see also Pollack et al., 1993). However, there is a strong bias to high heat-flux values because many measurements were made in geothermal areas (e.g., the western United States and Baikal rift). In the United States, a large fraction of the more than 14 000 heat flux measurements belong to the Basin and Range Province. Excluding the values from the United States, the mean continental heat flux is only $66\,\mathrm{mW\,m^{-2}}$.

Bias in the sampling can be removed by area weighting the average as demonstrated in Table 6. Averaging over $1 \times 1$ windows yields a mean heat flux of $65.3\,\mathrm{mW\,m^{-2}}$. Using wider windows does not change this mean value significantly. The histograms of individual heat flux values and $1 \times 1$ averages have identical shapes, except for the extremely high values ($>200\,\mathrm{mW\,m^{-2}}$). Pollack et al. (1993) and later Davies and Davies (2010) had obtained a mean continental heat flux of $65–66\,\mathrm{mW\,m^{-2}}$ by binning heat flux values by tectonic age and weighting by the area. Different methods to estimate the mean continental heat flux consistently yield $63–66\,\mathrm{mW\,m^{-2}}$ (Jaupart and Mareschal, Chapter 6.05). For a mean continental heat flux value of $65\,\mathrm{mW\,m^{-2}}$, the contribution of all the continental areas (i.e., $210 \times 10^6\,\mathrm{km^2}$) to the energy loss of the Earth represents $\approx 14$ TW. This number includes the submerged margins and continental areas with active tectonics,

**Table 6** Continental heat flux statistics[a]

| | $\mu(Q)$ (mW m$^{-2}$) | $\sigma(Q)$ (mW m$^{-2}$) | N(Q) |
|---|---|---|---|
| *All measurements* | | | |
| All values | 70.1 | 152.0 | 35 065 |
| Averages 1° × 1° | 64.5 | 64.7 | 4261 |
| Averages 2° × 2° | 63.7 | 53.9 | 1955 |
| Averages 3° × 3° | 62.6 | 34.4 | 1205 |
| *Standard measurements only* | | | |
| All values | 80.3 | 215.1 | 17 256 |
| Averages 1° × 1° | 64.8 | 79.8 | 3391 |
| Averages 2° × 2° | 63.0 | 57.4 | 1673 |
| Averages 3° × 3° | 62.6 | 37.3 | 1051 |

[a] $\mu$ is the mean, $\sigma$ is the standard deviation, and $N$ is the number of values.

where higher than normal heat flux values are associated with thick radiogenic crust and shallow magmatic activity. Uncertainty in this number is due to lack of adequate data coverage in Greenland, Antarctica, and large parts of Africa. To estimate the induced uncertainty, we assume that heat flux in those areas is equal to either the lowest or the highest average heat flux recorded in well-sampled geologic provinces (36 and 100 mW $m^{-2}$, respectively). This procedure allows departures of $\pm 1.5$ TW from the estimate of 14 TW. This uncertainty is certainly exaggerated because the poorly sampled regions are vast and contain geologic provinces of various ages and geologic histories; for instance, both Antarctica and Greenland are known to include high and low heat-flux regions. For the sake of simplicity, we retain a final uncertainty estimate of 1 TW.

### 7.06.4.2 Various Contributions to the Surface Heat Flux in Continental Areas

Determining the heat loss from the mantle through the continental lithosphere requires accounting for the radiogenic heat production. In stable continents, for ages greater than about 500 My, continents are near thermal steady state such that surface heat flux is the sum of heat production in the lithosphere and of the heat supply at the base of the lithosphere. The average heat flux does not vary significantly for provinces older than 500 My (Sclater et al., 1980) and, only in Archean (i.e., older than 2.5 Gy) provinces, it might be lower than in younger terranes (Morgan, 1983). We shall focus on estimating the crustal heat production and shall discuss briefly the contribution of the lithospheric mantle. The number of heat flux determinations in Archean and Precambrian provinces has increased during the past 30 years. With adequate sampling of heat flux and heat production, and detailed information on geology and crustal structure, the crustal and mantle components of the heat flux can now be determined. Further constraints are provided by ($P$, $T$) data on mantle xenoliths brought to the surface by kimberlite eruptions. It will be shown that, for stable regions, the crustal heat production makes the dominant contribution and the heat flux from the mantle is low.

Recently active regions are in a transient thermal regime and the high surface heat flux reflects cooling of the continental lithosphere. After removing the crustal heat production (which has been determined in stable provinces), it is possible to estimate the transient component of the heat flux, which originates in mantle cooling.

### 7.06.4.3 Estimating Moho Heat Flux

Many authors have assumed that the mantle heat flux is $\approx 25$ mW $m^{-2}$ in stable continental regions, because this was the lowest measured value (Cermak and Bodri, 1986; Pollack and Chapman, 1977a). As the number of measurements increased, it became clear that this cannot be true. Heat flux values $\approx 20$ mW $m^{-2}$ or less have been obtained in several different locations (Chapman and Pollack, 1974; Duchkov, 1991; Mareschal et al., 2000a,b, 2005; Swanberg et al., 1974), and the average heat flux over wide areas ($500 \times 500$ $km^2$) of the Baltic and Siberian Shields is $<18$ mW $m^{-2}$. For the mantle heat flux to be equal to that at the surface, the whole crust below each measurement site must be completely devoid of heat-producing elements over a large area, which is not realistic. Tightening the range of values for the mantle heat flux was achieved in various ways.

#### 7.06.4.3.1 Relationship between heat flow and heat production

Early attempts to calculate mantle heat flux relied on an empirical relationship between heat flux and heat production rate (Birch et al., 1968; Roy et al., 1968):

$$Q = Q_r + D \times H \qquad [44]$$

where $Q$ is the local surface heat flux, $H$ is the local surface heat production, and $D$ is a length scale related to the thickness of a shallow layer enriched in radiogenic elements. The intercept $Q_r$ represents the contribution of the mantle and crust below the enriched shallow layer. It was suggested that crustal heat production decreases exponentially as a function of depth down to the Moho (Lachenbruch, 1970). If this were true, values for $D$ ($\approx 10$ km) would imply that the mantle heat flux is equal to $Q_r$. Although it was soon realized that it cannot be so, this is still taken for granted by many authors.

The significance of the empirical heat flow heat production relationship has been questioned on various grounds (England et al., 1980; Jaupart, 1983). For the rather small wavelengths involved, theory shows that the surface heat flux is only sensitive to shallow heat production contrasts (Jaupart, 1983; Vasseur and Singh, 1986). With more data available, it was found that the linear relationship is not verified in many geologic provinces (Jaupart and Mareschal, 1999; Jaupart et al., 1982). The crustal component of the heat flux can now be estimated from systematic investigations of lower crustal rocks, from both large granulite facies terrains (Ashwal et al., 1987; Fountain and Salisbury, 1981; Fountain et al., 1987) and xenolith suites (Rudnick and Fountain, 1995). The heat production values, obtained on samples from large exposure of granulite facies terranes in different areas of the Superior Province, are very consistent ($\approx 0.4$ μW $m^{-3}$). They appear to be representative of all granulite facies terranes worldwide, including the Ivrea zone (Joeleht and Kukkonen, 1998; Pinet and Jaupart, 1987). Thirdly, sampling in superdeep holes (Kola, Russia, and KTB, Germany) demonstrates that heat production shows no systematic variation with depth as would be required by the linear relationship. At Kola, the Proterozoic supracrustal rocks (above 4 km depth) have lower heat production (0.4 μW $m^{-3}$) than the Archean basement (1.47 μW $m^{-3}$) (Kremenentsky et al., 1989). At KTB, heat production decreases with depth at shallow levels, reaches a minimum between 3 and 8 km, and increases again in the deepest parts of the borehole (Clauser et al., 1997). Over a larger depth extent, studies of exposed crustal sections suggest a general trend of decreasing heat production with depth, but this trend is not a monotonic function (Ashwal et al., 1987; Fountain et al., 1987; Ketcham, 1996). Even for the Sierra Nevada Batholith where the exponential model had initially been proposed, recent research has shown that the heat production does not decrease exponentially with depth (Brady et al., 2006). In the Sierra Nevada, heat production first increases, then decreases, and remains constant in the lower crust beneath 15 km.

Another approach was to assume that the mantle heat flux is roughly proportional to the average surface heat flux (in a

proportion of ≈40%, Pollack and Chapman (1977b)). This analysis, however, was based on a small data set and implies that the crustal heat production is proportional to the mantle heat flux, which has no physical basis. In order to detect changes of mantle heat flux, small-scale heat flux variations are of little use because they record shallow heat production contrasts and one must work at a minimum scale of about 250 km (Mareschal and Jaupart, 2004). This places stringent constraints on data coverage because heat flux and heat production vary on a typical scale of 10 km due to the heterogeneity of the crust. In North America, there are sufficient data to illustrate the influence of the horizontal scale on heat flux and heat production. With individual measurements in a single geologic province, there is no meaningful $(Q, H)$ relationship. At the scale of $\approx 250 \times 250$ km windows, a relationship between heat flux and heat production begins to emerge (Lévy et al., 2010). At the larger scale of geologic provinces with different crustal structures and histories ($\approx 500 \times 500$ km), the relationship is well defined and statistically significant (Figure 8). The data are close to a relationship of the form

$$\overline{Q} = Q_i + D\overline{H} \qquad [45]$$

where $\overline{Q}$ and $\overline{H}$ are province-wide averaged heat flux and heat production. That this relationship takes the same form as the 'local' relationship (eqn [44]) is probably fortuitous. In northern America, the latter is only valid for relatively small-scale variations (typically 10–50 km) of heat flux and heat production over Appalachian plutons and does not hold in the Precambrian provinces (Grenville, Trans-Hudson orogen, and Superior Province). The new relationship (eqn [45]) reflects variations of average heat flux on a much larger scale (>500 km) and relies on a very large data set. It implies that the average heat flux takes the same value $Q_i$ at some intermediate crustal depth in all provinces. Formally, it is not possible to rule out variations of mantle heat flux between the five provinces, but the data require that such variations are exactly compensated by opposite variations of lower crustal heat production. It is hard to explain how this may be achieved in practice, and the most sensible hypothesis is that the mantle heat flux is approximately the same

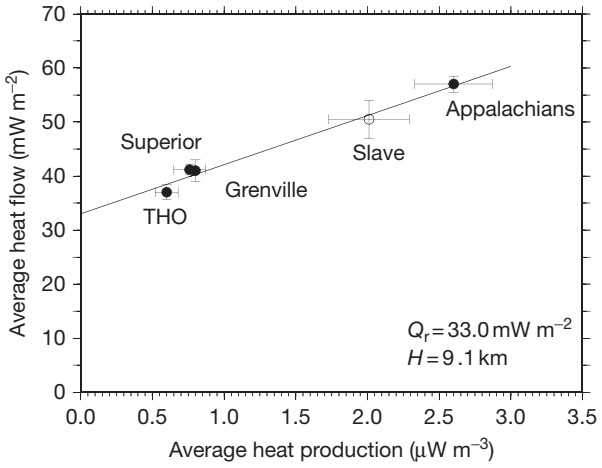


**Figure 8** Averaged heat flux versus average surface heat production for five major geologic provinces of North America. The solid line is the best-fit linear relationship of eqn [45].

beneath the five provinces. For these provinces, independent geophysical and petrologic constraints on crustal structure show indeed that changes of crustal heat production account for the observed heat flux variations (Mareschal et al., 1999; Pinet et al., 1991).

We now describe several methods for calculating crustal heat production, which consistently imply that the mantle heat flux is $\leq 18\,\mathrm{mW\,m^{-2}}$.

#### 7.06.4.3.2 Crustal heat production and Moho heat flux

In several parts of the Canadian Shield, heat flux values as low as 22 mW m$^{-2}$ have been measured ( Jaupart and Mareschal, 1999; Mareschal et al., 2000a,b). Similar or even lower values have also been reported for the Siberian Shield (Duchkov, 1991), the Norwegian Shield (Swanberg et al., 1974), and Western Australia (Cull, 1991). These low values, which correspond to areas where the crustal contribution is the lowest, provide an upper bound to the mantle heat flux. One may refine this estimate further by subtracting some lower bound for crustal heat production. Surface heat flux records a large-scale average of heat production, and one should consider a representative crustal assemblage and not a single rock type such as gabbro. For no crustal material are heat production estimates lower than $0.1\,\mu\mathrm{W\,m^{-3}}$ ( Joeleht and Kukkonen, 1998; Pinet and Jaupart, 1987; Rudnick and Fountain, 1995). Over an average thickness of ≈40 km, the contribution of the crust must be at least $4\,\mathrm{mW\,m^{-2}}$, and the mantle heat flux must be <18 mW m$^{-1}$. In Norway, Swanberg et al. (1974) obtained a heat flux value of 21 mW m$^{-2}$ over an anorthosite body; after estimating the crustal heat production, they concluded that mantle heat flux is about 11 mW m$^{-2}$. The same value was obtained from the analysis of all the heat flux and radiogenic heat production data in the Norwegian Shield (Pinet and Jaupart, 1987).

A lower bound on mantle heat flux can be obtained by requiring that melting conditions are not attained in the crust in the absence of tectonic events and magmatic intrusions (Rolandone et al., 2002). In high heat-flux areas of the Canadian Shield, crustal rocks are at high temperatures today and were still hotter in the past when radiogenic heat production was higher. The condition of thermal stability provides a lower bound of 11 mW m$^{-2}$ on the mantle heat flux. Combining this result with the independent constraints derived from present-day heat flux values leads to a range of 11–18 mW m$^{-2}$ for the mantle heat flux beneath the Canadian Shield. Arguments different from these have led to the same range of values in other Precambrian areas (Guillou-Frottier et al., 1995; Gupta et al., 1991; Jones, 1988).

In several regions of the world, a large fraction of the crustal column has been exposed by tectonic processes. Sampling of such exposed cross sections allows the determination of the vertical distribution of radiogenic elements. If heat flux and seismic data are also available, it is possible to determine the total crustal heat production. For the Kapuskasing structure in the Canadian Shield where the crustal contribution could be determined, the Moho heat flux was calculated to be 13 mW m$^{-2}$ (Ashwal et al., 1987; Pinet et al., 1991). The average crustal heat production can also be estimated in provinces where all crustal levels can be found at the surface. In these provinces, systematic sampling will yield an estimate of the average bulk crustal heat production. In the Grenville

province of the Canadian Shield, the average crustal heat production was determined to be 0.65 μW m$^{-3}$ for an average surface heat flux of 41 mW m$^{-2}$. This yields a Moho heat flux of 15 mW m$^{-2}$ (Pinet et al., 1991). Similar results have been reported for other shields in the world, including South Africa (Nicolaysen et al., 1981) and India (Roy and Rao, 2000), and are listed in Table 7.

Other methods have combined heat flux with other geophysical data, mainly long-wavelength Bouguer gravity, to estimate changes in crustal composition. A search for all models consistent with all the available data, including gravity data and bounds on heat production rates for the various rock types involved, leads to a range of 7–15 mW m$^{-2}$ for the mantle heat flux in eastern Canada (Guillou et al., 1994).

The estimates mentioned earlier were derived using local geophysical and heat production data in several provinces and rely on knowledge of crustal structure. Independent determinations of the mantle heat flux may be obtained by considering the lithosphere thickness determined by seismic and xenolith studies. Pressure and temperature estimates from mantle xenoliths may be combined to determine a best-fit geotherm consistent with heat transport by conduction. Mantle heat flux estimates obtained in this manner depend on the value assumed for thermal conductivity. Available estimates are consistent with those deduced from crustal models and are listed in Table 7.

The estimates of Table 7 come from Archean and Proterozoic cratons where heat flux values are generally low. Heat flux values tend to be larger in younger stable continental regions. For example, heat flux is higher (57 mW m$^{-2}$) in the Appalachians than in the Canadian Shield. The crust of the Appalachians contains many young granite intrusions with very high heat production (>3 μW m$^{-3}$). The elevated heat flux can be accounted for by the contribution of these granites and does not require mantle heat flux to be higher than in the shield (Mareschal et al., 2000a,b; Pinet et al., 1991). Throughout stable North America, including the Appalachians, variations of the mantle heat flux may not be exactly zero but must be less than departures from the best-fitting relationship (Figure 8), or about ±2 mW m$^{-2}$. This estimate is close to the intrinsic uncertainty of heat flux measurements (Jaupart and Mareschal, 1999).

Allowing for the uncertainties and requiring consistency with low heat-flux measurements, we retain the range of 15 ± 3 mW m$^{-2}$ for the mantle heat flux in stable continents. For this range, the differences of average heat flux between geologic provinces cannot be accounted for by changes of mantle heat flux and must be attributed to changes of crustal heat production. The ranges of heat flux and heat production values are the same for all provinces between 200 My and 2.5 Gy, with a weak trend of decreasing average heat flux and heat production with age (Perry et al., 2006). The range is narrower in Archean provinces where high heat-flux values are not found, possibly because a very radioactive crust would have been too hot to be stabilized (Morgan, 1983). Averaging the heat production of the crust of different ages yields a range of 0.79–0.99 μW m$^{-3}$ (Table 8 and Jaupart and Mareschal (2013)).

**Table 7** Various estimates of the heat flux at Moho in stable continental regions

| *Location* | *Heat flux (mW m$^{-2}$)* | *Reference* |
|---|---|---|
| Norwegian Shield | 11[a] | Swanberg et al. (1974) and Pinet and Jaupart (1987) |
| Baltic Shield | 7–15[a] | Kukkonen and Peltonen (1999) |
| Siberian craton | 10–12[a] | Duchkov (1991) |
| Dharwar Craton (India) | 11[a] | Roy and Rao (2000) |
| Kapuskasing (Canadian Shield) | 11–13[a] | Ashwal et al. (1987) and Pinet et al. (1991) |
| Grenville (Canadian Shield) | 13[a] | Pinet et al. (1991) |
| Abitibi (Canadian Shield) | 10–14[a] | Guillou et al. (1994) |
| Trans-Hudson orogen (Canadian Shield) | 11–16[b] | Rolandone et al. (2002) |
| Slave province (Canada) | 12–24[c] | Russell et al. (2001) |
| Vredefort (South Africa) | 18[a] | Nicolaysen et al. (1981) |
| Kalahari Craton (South Africa) | 17–25[c] | Rudnick and Nyblade (1999) |

[a]Estimated from surface heat flux and crustal heat production.
[b]Estimated from condition of no melting in the lower crust at the time of stabilization.
[c]Estimated from geothermobarometry on mantle xenoliths.

### 7.06.4.4 Recently Active Regions and Continental Margins

Submerged and recently active (i.e., during the past 200 My) continental areas cover 92 × 10$^6$ km$^2$, ≈45% of the total continental surface (Table 5). These regions are not in thermal steady state and are characterized by higher heat flux than the continental average. Because of the long thermal relaxation time of the continental lithosphere, present surface heat flux includes the inputs of heat from the mantle of the past 100–200 My. The crustal component can now be calculated from crustal thickness and average heat production. After accounting for crustal heat production, the heat from the mantle (including the transient component) can be estimated.

#### *7.06.4.4.1 Compressional orogens*

In compressional orogens, crustal and lithospheric thickening result in reduced temperature gradients and heat flux, but the total heat production in the thick crust is high. These two competing effects lead to a complex transient thermal structure, and few generalizations can be made on the surface

**Table 8** Estimates of bulk continental crust heat production from heat flux data (Jaupart and Mareschal, 2013)

| *Age group* | *Heat production (μW m$^{-3}$)* | *Total (40 km crust) (mW m$^{-2}$)* | *% Area* [a] |
|---|---|---|---|
| Archean | 0.56–0.73 | 23–30 | 9 |
| Proterozoic | 0.73–0.90 | 30–37 | 56 |
| Phanerozoic | 0.95–1.21 | 37–47 | 35 |
| Total continents | 0.79–0.99 | 32–40 | |

[a]Fraction of total continental surface, from model 2 in Rudnick and Fountain (1995).

heat flux. For instance, very high heat-flux values ($>100$ mW m$^{-2}$) have been measured on the Tibetan Plateau (Francheteau et al., 1984; Hu et al., 2000; Jaupart et al., 1985). They have been attributed to shallow magma intrusions and yield little information on the mantle heat flux. In contrast, present surface heat flux remains low in the Alps, and after removing the crustal heat production, heat flux at the Moho is estimated to be as low as 5 mW m$^{-2}$ (Vosteen et al., 2003). After removing the crustal contribution, heat flux from the mantle is also low beneath the North American Cordillera (Brady et al., 2006) and beneath the South American Cordillera, at least where it has not been affected by back-arc extension (Henry and Pollack, 1988).

#### 7.06.4.4.2 Rifts and continental zones of extension

In rifts, recently extended regions, continental margins, and basins, heat flux is higher than in stable areas because of a large transient component, which ultimately represents additional outputs of heat from the mantle. Crustal extension and lithospheric thinning will instantly result in steepening the temperature gradient and increasing the heat flux. Thermal relaxation from the initial conditions depends on the boundary condition at the base of the lithosphere.

In zones of extension and continental rifts, heat flux values are significantly higher (75–125 mW m$^{-2}$) than in stable regions (Morgan, 1983). A striking feature of extension zones is that the transition between the region of elevated heat flux and the surrounding is as sharp as the sampling allows one to determine, that is, Colorado Plateau–Basin and Range Province in North America (Bodell and Chapman, 1982), East African Rift–Tanzania Craton (Nyblade, 1997), and Baikal rift–Siberian craton (Poort and Klerkx, 2004). This suggests that the enhanced heat flux is not due to conductive processes but is the direct result of extension and lithospheric thinning. With sufficient sampling, one can detect short-wavelength variations of heat flux that can be attributed to the cooling of shallow magmatic intrusions and groundwater movement. The actual heat loss is higher than the average conductive value because of heat transport by hot springs and magmas. Lachenbruch and Sass (1978) had estimated that the heat delivered by volcanic systems in rifts and in the Basin and Range Province is negligible. They had also argued that the integrated effect of heat transport by groundwater is small for this province, with the exception of the Yellowstone system, where locally the heat flux is $>40$ W m$^{-2}$. Heat loss for the entire Yellowstone system has been estimated to be $\approx 5$ GW, including both conductive and convective components (Fournier, 1989). It would thus require 200 'Yellowstones' to increase the continental heat loss by 1 TW. The effect of continental hot spots on the budget seems presently negligible. Estimates for the total heat loss through geothermal systems in the East African Rift are comparable to those of Yellowstone (Crane and O'Connell, 1983). Similar values have been inferred for Baikal (Poort and Klerkx, 2004). In continental as well as in oceanic rifts, the heat loss is underestimated because of hydrothermal heat transport. However, because continental rifts are narrow and their total surface area is small, they account for a small fraction of the total continental heat loss, and errors on their contribution will have a negligible impact on the end result.

The contribution of wide regions of extension is more significant than that of rifts. In the Basin and Range Province in the southwestern United States, the high average heat flux (105 mW m$^{-2}$) has been attributed to an extension of 100% (Lachenbruch and Sass, 1978). This interpretation depends on assumptions on the preextensional heat flux and on crustal heat production. Early estimates of the mantle heat loss are probably too large because the crustal heat production was underestimated (Ketcham, 1996). It now appears that the average heat production of the crust is the same as in stable regions and yields a total crustal heat flux contribution of $\approx 33$ mW m$^{-2}$. This implies that the transient component due to cooling and the mantle heat flux in the Basin and Range Province add up to a total of $\approx 70$ mW m$^{-2}$ (Ketcham, 1996). Physical models to account for this heat loss assume either delamination of the lithospheric mantle or stretching and transport of heat into the lithosphere by magmatic intrusions (Lachenbruch and Sass, 1978). Regardless of the mechanism, at least 2/3 of the heat flux in regions of extension comes from the mantle.

Large igneous provinces testify of periods of enhanced volcanic activity in the continents. Their effect on the heat flow is however negligible. In the Deccan, where 500 000 km$^3$ of basalts was deposited *c.*60 My, there is no heat flow anomaly, suggesting that the magmas did not heat up the lithosphere over large volumes. Assuming that the lavas were deposited in 1 My, the heat that they carried to the surface contributed $<0.1$ TW to the energy budget.

#### 7.06.4.4.3 Continental margins: Passive

Continental margins are the transition zones between ocean and continents and have the characteristics of both: crust that is enriched in radioelements and rests on top of thin lithosphere. For a total length of about 100 000 km (Bradley, 2008) and an average width of 300 km, they cover $30 \times 10^6$ km$^2$, or 15% of the total continental area. Passive margins form during the breakup of continents as continental lithosphere extends and seafloor spreading begins. They come in many different styles and shapes, depending on width, abundance of magmatic activity, and sediment thickness. Their deepest parts are generally made of hyperextended continental crust and in some cases exhumed continental mantle (Boillot et al., 1980; Unternehr et al., 2010; Whitmarsh et al., 2001). They subside as the thermal perturbation caused by thinning and rifting decays (Sleep, 1971; Vogt and Ostenso, 1967). Most of the present-day ones, which border the Atlantic and Indian Oceans, formed during the breakup of Gondwanaland and have returned to thermal equilibrium. A few recent ones (Red Sea, Gulf of Aden, North Atlantic, etc.) are in transient thermal regimes.

Heat flow measurements on passive margins are scarce because conventional techniques are not adapted to shallow water environments and/or to the high-porosity sedimentary layers. Many heat flow values have been deduced from temperatures recorded in oil wells on continental platforms or from the depth of the bottom simulating reflector (BSR) on continental slopes. Oil well data are either bottom hole temperatures, which are perturbed by mud circulation and drilling operations, or fluid temperatures during completion tests, which are considered to be more reliable. BSRs are strong

reflectors that occur at the lower stability limit of gas hydrates and free gas (Singh et al., 1993). Because the stability limit depends on pressure and temperature, the geothermal gradient can be estimated from the depth of the BSR. Usually, thermal conductivity is estimated empirically from lithology and porosity, which adds to the uncertainty. The accuracy of these data has been assessed in a few deep margins through a comparison with conventional marine measurements (Lucazeau et al., 2004). Analysis of the global data set shows that heat flow measurements are highly scattered and decrease with the age of the margin (**Figure 9**), as expected (e.g., McKenzie, 1978). The values, however, are higher than the predictions of conductive models of passive rifting with acceptable amounts of stretching (**Figure 9**). Local surveys show indeed that the surface heat flux is perturbed with respect to the adjacent continental and oceanic domains.

In young continental margins (Red Sea and Gulf of Aden), heat flow is higher than could be expected from the magnitude of continental crust extension (Lucazeau et al., 2008; Martínez and Cochran, 1989). Heat flow increases abruptly at the landward edge of the transition region between oceanic and continental domains (OCT). The sharp lateral variation and the magnitude of the heat flux variation both require the presence of a shallow thermal anomaly. In the Gulf of Aden, for example, heat flow increases from 60 to 120 mW $m^{-2}$ over a few km and then remains almost constant for several tens of kilometers over the OCT (Lucazeau et al., 2008). Higher heat-flux values (up to 300 mW $m^{-2}$) have been measured in the northern Red Sea, where continental breakup is occurring today (Martínez and Cochran, 1989). Independent evidence for a shallow thermal anomaly comes from the depth of the seafloor. Sediments that are deposited in the OCT during early phases of extension and rifting belong to shallow water environments, indicating that the isostatic consequences of crustal thinning are compensated by the buoyancy of hot mantle (Huismans and Beaumont, 2011).

In mature continental margins, the surface heat flux is usually higher than expected from passive rifting models. In the Labrador margin (Canada), heat flux is about 15–25 mW $m^{-2}$ higher than on the adjacent continent (Goutorbe et al., 2007; Mareschal et al., 2000a,b). This is observed in many other regions, for example, the Gulf of Guinea (Lucazeau et al., 2004), Senegal (Latil-Brun and Lucazeau, 1988), South Africa (Goutorbe et al., 2008a), the Gulf of Mexico (Husson et al., 2008; Nagihara and Opre, 2005), South West India and Makran (Calves et al., 2010; Rao et al., 2001), Mozambique margin (Nyblade, 1997), Australian margins (Goutorbe et al., 2008b), and the Iberia margin (Louden et al., 1997). Many different explanations have been put forward, including high heat production in the sediments (McKenna and Sharp, 1998) or in the stretched continental crust (Louden et al., 1997; Nagihara and Opre, 2005), volcanism (Rao et al., 2001),

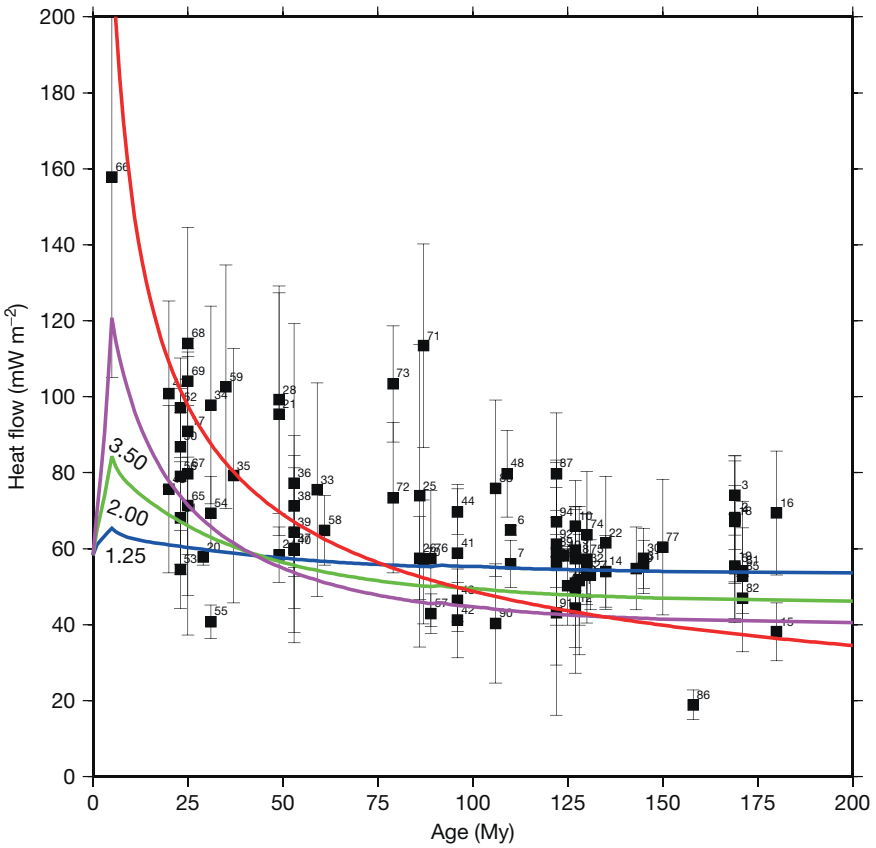


**Figure 9** Heat flow versus continental margin age. Results of the homogeneous extension model (McKenzie, 1978) modified to account for crustal heat production for stretching factors = 1.25 (blue), 2.00 (green), and 3.50 (magenta). The dark red curve shows the predictions of the half-space cooling model with $C_Q = 490$.

erosion, renewed rifting (Husson et al., 2008), and fluid circulation (Deming et al., 1992; Reiter and Jessop, 1985). The systematic pattern of heat flux variations in continental margins, however, is best accounted for by a local mantle convective circulation (Armitage et al., 2013; Grigne et al., 2007; Guillou and Jaupart, 1995; King and Anderson, 1998).

Measurements on passive margins, as defined in the UNESCO Geological Map of the World (CCGM/CGMW, 2000), account for $<5\%$ of the entries in the global heat flow database. They average 62 mW m$^{-2}$ (**Table 5**), which is close to the bulk continental average. OCTs are usually mapped as oceanic domains, but do not affect the statistics significantly if they are lumped with continental margins proper. Young rifted margins are associated with significantly higher heat flow values, but they account for $<10\%$ of the total passive margin area (Bradley, 2008). Multiplying the average heat flux by the area of passive margins, we obtain a heat loss contribution of 2.0 TW.

#### *7.06.4.4.4 Continental margins: Active*

Active continental margins lie at the transition between oceans and continents in subduction zones. There, the surface heat flux depends on the thermal structure and dip of the subducting plate (Molnar and England, 1990) and records local perturbations due to sedimentation (Hyndman et al., 1993; Marcaillou et al., 2006) and fluid flow (Henry and Wang, 1991; Hyndman et al., 1993). Theory predicts that the surface heat flux should decrease from the trench to the accretionary prism and forearc basin.

In forearc domains, heat flow reflects the thermal structure of the subducting plate and is related to the age of the plate. The average value is 70 mW m$^{-2}$ (**Figure 10**). In back-arc basins, heat flow is controlled mostly by the magnitude of extension and magmatic activity and takes large values with an average of 91 mW m$^{-2}$ (**Table 5**). Similar values are found in active mobile belts, such as the Canadian Cordillera and Cascadia (Hyndman, 2010; Lewis et al., 2003).

For a total area of $30\times10^6$ km$^2$, active margins contribute $\sim$2.4 TW to the total heat loss, assuming equal partitioning between forearcs and back-arcs.

### 7.06.4.5 Mantle Heat Loss Through Continental Areas

There is a major difference in the thermal regime between stable and active continental regions. In stable continental regions, the mean heat flux is low ($\leq$55 mW m$^{-2}$) and mostly comes from crustal heat production. Heat flux from the mantle is $\approx$15 mW m$^{-2}$. In extensional regions, the high heat flux ($\geq$75 mW m$^{-2}$) includes contributions from crustal radioactivity ($\approx$30 mW m$^{-2}$) as well as from thermal relaxation of the mantle. Despite their thin crust, continental margins also have higher than average heat flux ($\approx$80 mW m$^{-2}$) because they are cooling after being extended.

Different methods lead to a value of 14 TW for the integrated heat flux from continental areas. Neglecting geothermal and volcanic transport has no significant impact on this value. The estimated average heat production of the continental crust ranges between 0.79 and 0.99 μW m$^{-3}$ (Jaupart and Mareschal, 2013), and the total volume of continental crust is $\approx0.73\times10^{10}$ km$^3$, which gives a total heat production in the crust between 6 and 7 TW.

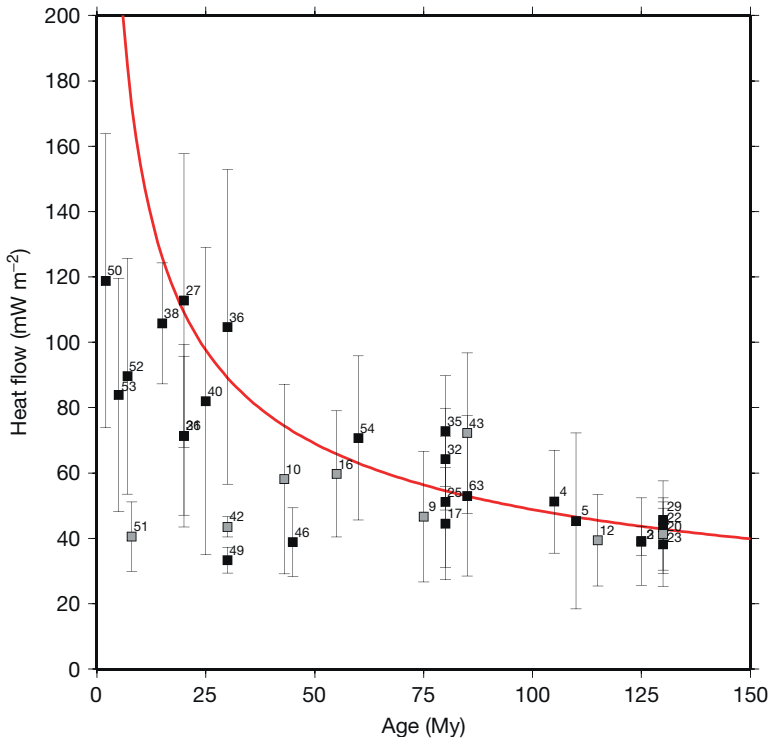


**Figure 10** Heat flow measured on trenches and forearc basins versus age of the subducting plate. Black symbols are measurements close to the trenches and gray symbols are measurements obtained at distance >100 km. Oceanic half-space cooling model for $C_0=490$ is also shown (red curve).

Little is known about the amounts of radiogenic elements in the lithospheric mantle. Direct estimates rely on a few exposures of peridotite massifs, which are typically depleted (Rudnick et al., 1998), and on mantle xenoliths from kimberlite pipes, which are usually enriched (Russell et al., 2001). Considerations on the thermal stability of continental roots and consistency with heat flux measurements as well as with petrologic temperature estimates lead to the conclusion that enrichment must be recent and associated with metasomatic infiltrations (Jaupart and Mareschal, 1999; Russell et al., 2001). This enrichment process is probably limited in both area and volume and our best estimate of radiogenic heat production in the lithospheric mantle comes from peridotite massifs. For the sake of completeness, we take a value of 0.02 $\mu W\ m^{-3}$ (Rudnick et al., 1998) and consider an average lithosphere thickness of 150 km. The total heat thus generated in the subcontinental lithospheric mantle is about 0.5 TW, which is only accurate within a factor of about 2.

Subtracting the contribution of radioactive sources from the total heat loss out of continents, we thus arrive at an estimate of the heat input from the mantle of 6–7 TW, about half of which is brought through the tectonically active regions and the continental margins.

#### 7.06.4.6 Summary

Heat flux data are now available for provinces of all ages, including Archean cratons that were poorly sampled 30 years ago. About half of the heat loss through continents is accounted for by crustal radiogenic heat production. Stable continents allow a small heat flux of about 15 $mW\ m^{-2}$ out of the convecting mantle and act as insulators at the surface of the Earth.

### 7.06.5 Heat Sources

#### 7.06.5.1 Radiogenic Sources in the Bulk Silicate Earth

The composition of our planet cannot be measured directly for lack of direct samples from the lower mantle and the core and has been estimated using various methods. It had been noted by Birch (1965) that if the Earth had a chondritic composition, its heat production would match what was then thought to be the heat loss (30 TW). This remarkable coincidence did not resist close scrutiny. It was soon noted that the Earth is depleted in K relative to chondrites and this reduces the heat production (Wasserburg et al., 1964). With the same amount of U and Th as in the chondrites, and a terrestrial K/U ratio, the total heat production was estimated to be only 20 TW (Wasserburg et al., 1964). On the other side of the balance, the heat loss is now believed to be much larger than it was then.

All attempts to construct a bulk Earth composition model rely on two different kinds of samples: meteorites, which represent the starting material, and pieces of today's upper mantle. Both show rather extensive variations of composition due to their different histories. Processes in the early solar nebula at high temperature contribute one type of compositional variation. Processes within the Earth, which occur at lower temperatures, contribute another type of compositional variation. Stated schematically, one has a range of compositions from the early solar system and a range of compositions for the upper mantle of the Earth, and one must devise a procedure to account for the different processes that have affected the two types of samples.

Chondrites represent samples of undifferentiated silicate material from the solar system prior to melting and metallic core segregation. Their composition derives from the solar composition altered by processes in the early solar nebula that have generated different families of chondrites. Perturbations are essentially brought in the gas state and elemental behavior is classified according to volatility (or condensation temperature). For our present purposes, the important elements are uranium, thorium, and potassium. The first two are associated with very high condensation temperatures and called 'refractory lithophile' elements (RLE). That these two elements have the same behavior in the early solar system is demonstrated by the fact that they have the same ratio in all types of chondritic meteorites. Potassium is a 'moderately volatile' element with a lower condensation temperature. The best match with solar concentration ratios is achieved by CI chondrites, which explains why many Earth models have relied on them. However, we do know that CI chondrites have larger amounts of volatiles, including water and $CO_2$, than the Earth. As regards samples from the Earth's mantle, one may establish a systematic compositional trend through the samples and identify the most primitive (and least differentiated) material. With these problems in mind, we review the four main types of approaches that have been used and the resulting estimates of Earth composition. We shall refer to the bulk silicate Earth (BSE) that corresponds to mantle and crust.

The first method relies on direct samples from the mantle. Ringwood (1962) argued that basalts and peridotites are complementary rocks, such that the latter is the solid residue of the partial melting event that led to basalt genesis and extraction. Thus, mixing them back together with the appropriate proportions yields the starting material, which was named 'pyrolite.' Clearly, one has to choose the samples that have not been affected by leaching and low-temperature alteration. Unfortunately, this procedure is not efficient for uranium, which is very mobile and seldom resists weathering.

A second method relies on a choice for the starting material. BSE concentrations are obtained by working one's way through the processes that turn meteorites into Earth-like material: devolatilization (loss of water, $CO_2$, and other volatile elements present in very small amounts in the Earth), followed by reduction (loss of oxygen) and segregation of a metallic core. Errors associated with this obviously come not only from the mass loss estimates but also from the starting chondrite composition since the different groups of meteorites are all quite heterogeneous. Many authors (e.g., Hart and Zindler, 1986) have used CI chondrites, as explained earlier. Javoy (1995, 1999) had argued in favor of a different type of meteorites. His line of reasoning focuses on the oxidation state of the solar nebula when it started to condense. The only meteorites with the right isotopic ratios and oxidation state are enstatite chondrites (EH) (Javoy et al., 2010). These chondrites are largely degassed, save for sulfur, so that the volatile loss correction is small. RLE elements are not affected by devolatilization and core segregation and one can use this property to avoid forward calculations that are error-prone given the many variables and parameters involved. Calcium belongs to the RLE group and

the Th/Ca and U/Ca ratios of EH chondrites, which are necessarily identical to the BSE values, are known (Wasson and Kalleymen, 1988). In the model of Kaminski and Javoy (2013) for the formation of the Earth's mantle and core out of EH chondritic material, the BSE Ca concentration is $1.71 \pm 0.08$ wt%, which leads to values of 18.1 and 60.2 ppb for U and Th, respectively.

The debate about the starting material for the Earth is in full swing at the time of writing, and one can expect further developments as new isotopic measurements become available. The choice of starting material has implications for studies of the early solar nebula and meteorites on the one hand and of the Earth's mantle structure on the other hand. For example, one argument against EH chondrites as Earth building material is that their Si/Mg ratio is much larger than that of the upper mantle, which requires a lower mantle enriched in Si (Fitoussi and Bourdon, 2012). In fact, it may be that the Earth was not made out of chondritic material. This is suggested by differences in the $^{142}$Nd concentrations and $^{142}$Nd/$^{144}$Nd ratios of chondrites and terrestrial rocks (Boyet and Carlson, 2005; Boyet and Gannoun, 2013; Caro et al., 2008). Using the terrestrial Nd values and geochemical systematics, Caro and Bourdon (2010) and Jackson and Jellinek (2013) had built a nonchondritic BSE model that has lower U and Th concentrations than chondritic ones (**Table 9**).

A third method tries to avoid a specific choice for the starting composition and aims at determining it. Hart and Zindler (1986) determined the compositional trends of chondritic meteorites and peridotites, which are not parallel to one another. Each trend records the effects of the two different sets of processes operating in the primitive solar nebula and in the Earth, and their intersection can only be the starting Earth material. In this case, the error comes from the scatter around the two compositional trends.

A fourth method relies on elemental ratios. For RLE, such as uranium and thorium, the concentration ratio is independent of chondrite type and is a property of the starting Earth material. Once these ratios have been determined, two procedures can be used to determine primitive abundances from measurements on peridotite samples. In one procedure, one starts with one specific element for which one can determine a reliable value for the bulk Earth and work sequentially to all the others using elemental ratios. The element of choice is Mg because, although it is not the most refractory element, its behavior during melting and alteration is well understood (Palme and O'Neill, 2003). The other procedure is to study the relationship between abundance and elemental ratios (McDonough and Sun, 1995). Changes in both values can be accounted for by variations in the degree of melting of peridotite. McDonough and Sun (1995) used a linear regression to extrapolate the data array to the chondritic ratio, which gives the primitive abundance. Depletion processes due to melt extraction are intrinsically nonlinear, however. With a more realistic treatment of these effects and tighter statistical analysis of the highly scattered data, Lyubetskaya and Korenaga (2007) had obtained a model for the BSE that is more depleted than previous ones. Uncertainties on the uranium, thorium, and potassium concentrations are large ($\approx$15%; see **Table 9**).

As regards the radioactive elements of interest here, the 'pyrolite' method is unreliable and was not used. **Table 9** lists

**Table 9** Radio-element concentration and heat production in meteorites, in the Bulk Silicate Earth, in Earth mantle and crust

| | *U (ppm)* | *Th (ppm)* | *K (ppm)* | A* *(pW kg$^{-1}$)* |
|---|---|---|---|---|
| CI chondrites | | | | |
| Palme and O'Neill (2003) | 0.008 | 0.030 | 544 | 3.5 |
| McDonough and Sun (1995) | 0.007 | 0.029 | 550 | 3.4 |
| EH chondrites | | | | |
| Wasson and Kalleymen (1988) | 0.009 | 0.030 | / | |
| Bulk silicate Earth | | | | |
| From CI chondrites | | | | |
| Javoy (1999) | 0.020 | 0.069 | 270 | 4.6 |
| From EH chondrites | | | | |
| Kaminski and Javoy (2013) [b] | $0.018 \pm 0.001$ | $0.060 \pm 0.003$ | $217 \pm 11$[a] | $4.0 \pm 0.2$ |
| From chondrites and lherzolites trends | | | | |
| Hart and Zindler (1986) | 0.021 | 0.079 | 264 | 4.9 |
| From elemental ratios and refractory lithophile element abundances | | | | |
| McDonough and Sun (1995) | $0.020 \pm 20\%$ | $0.079 \pm 15\%$ | $240 \pm 20\%$ | $4.8 \pm 0.8$ |
| Palme and O'Neill (2003) | $0.022 \pm 15\%$ | $0.083 \pm 15\%$ | $261 \pm 15\%$ | $5.1 \pm 0.8$ |
| Lyubetskaya and Korenaga (2007) | $0.017 \pm 0.003$ | $0.063 \pm 0.011$ | $190 \pm 40$ | $3.9 \pm 0.7$ |
| Jackson and Jellinek (2013) | $0.014 \pm 0.003$ | $0.055 \pm 0.011$ | $166 \pm 30$ | $3.4 \pm 0.5$ |
| Depleted MORB source | | | | |
| Workman and Hart (2005) | 0.0032 | 0.0079 | 25 | 0.59 |
| Average MORB mantle source | | | | |
| Su (2000) and Langmuir et al. (2005) | 0.013 | 0.040 | 160 | 2.8 |
| Peridotites | 0.006 | 0.02 | 100 | 1.5 |
| Continental crust | | | | |
| Rudnick and Gao (2003) | 1.3 | 5.6 | $1.5 \times 10^4$ | 330 |
| Jaupart and Mareschal (2013) | / | / | / | 293–352 |

[a]Calculated from the U value and K/U = 12 000.

[b]U and Th values deduced from the Ca concentration and the chondritic U/Ca and Th/Ca ratios.

estimates obtained by different authors using the other methods. One should note that concentration ratios are constrained more tightly than absolute concentrations. One cannot separate uncertainties due to the starting chemical data from those of the calculation algorithm, because each author uses his own data and method. Without major improvement in our understanding of early planetary accretion, it may well prove impossible to reduce the spread of results.

Values for U, Th, and K concentrations yield estimates of the radiogenic heat production rate in the Earth. We have used the revised decay constants listed in **Table 10** (Dye, 2012). Those differ slightly (<4%) from the earlier estimates given by Rybach (1988), which are commonly used in the geophysical literature. Heat production values vary within a restricted range, from 3.4 to 5.1 pW $kg^{-1}$. The BSE model of Palme and O'Neill (2003) leads to the highest value and may well be an overestimate. The EH chondrite model does not lead to a major difference for the present-day heat production rate but implies important changes at early ages because its Th/U and K/U ratios differ strongly from the others. In spite of the differences, the range of compositions from the various estimates (≈15%) is sufficiently wide to allow some overlap between them.

The different models for the bulk silicate Earth, which includes continental crust, are listed in **Table 9**. They lead to a total rate of heat production of 18 TW, with an uncertainty of 28%. After removing the contributions of the continental crust (6–7 TW) and the lithospheric mantle (≈1 TW), heat production in the mantle amounts to a total of 11 TW, with an uncertainty of 55%.

Independent constraints can be derived from the compositions of MORBs, which have been comprehensively sampled. MORBs span a rather wide compositional range and common practice has been to define end-members associated with different chemical reservoirs. According to this framework, depleted MORBs come from a depleted reservoir whose complement is enriched continental crust. Enriched basalts are attributed to primitive mantle tapped by deep mantle plumes or to secondary processes, for example, infiltrations of low-degree melts and metasomatic fluids in subduction zones (Donnelly et al., 2004). The heat production rate of the depleted MORB mantle source is ≈0.6 pW $kg^{-1}$ (i.e., at this rate, the entire mantle would generate only 2.4 TW). This source, however, does not provide an exact complement of average continental crust (Workman and Hart, 2005). An alternative approach avoids the separation of different mantle reservoirs and determines the average composition of all the mantle that gets tapped by mid-ocean ridges (Langmuir et al., 2005; Su, 2000). Composition of the average MORB mantle source is then derived from a well-constrained melting model. This mantle reservoir is a mixture of different components and is the average mantle lying below oceanic ridges. It is depleted in compatible elements and may be interpreted as the mantle reservoir that has been processed to form continents (Langmuir et al., 2005). There may be a volume of primitive mantle lying at depth that has never been sampled by mid-oceanic ridges, however. Assuming that the average MORB source extends through the whole mantle leads to a lower bound of 11 TW on the total mantle heat production (**Table 9**). Adding radioelements from the continental crust and lithospheric mantle, which contribute 7–8 TW, we obtain a lower bound of 18 TW for the total rate of heat production in the Earth. This is consistent with the BSE models and their uncertainties.

### 7.06.5.2 Geoneutrino Measurements

So far, it has been impossible to directly detect heat-producing elements in the mantle and measure their concentration, but this may change with the advent of 'geoneutrino' detection. 'Geoneutrinos' are antineutrinos generated by the decay of the radioelements in the Earth and they can be captured by the large liquid scintillation detectors of underground neutrino observatories (Dye, 2010; Enomoto et al., 2007; Fiorentini et al., 2005; Kamland collaboration, 2011; Raghavan et al., 1998; Rothschild et al., 1998). With the present technology, only geoneutrinos from U and Th decay can be detected, but geoneutrinos from K decay cannot because their energy is below the detection threshold. With the very small cross section of the geoneutrinos (on the order of $10^{-44}cm^2$), very long exposure times in large detectors are required for statistically significant measurements. The geoneutrino flux integrates all the sources in the Earth, from the crust as well as from the mantle. In a continental observatory, at least 75% of this flux comes from the crust (Enomoto et al., 2007). For determining the geoneutrino flux from the mantle, the local crustal contribution must be very accurately accounted for, which represents a difficult challenge (Dye, 2010; Perry et al., 2009). This problem could be circumvented by deploying large submarine detectors on the seafloor where the crustal contribution to the geoneutrino flux is minimum (Dye et al., 2006). An alternative solution would be to measure the direction of the interacting geoneutrinos, which

**Table 10** Heat production constants

| *Isotope/element* | *Natural abundance (%)* | *Half-life (year)* | *Energy per atom (pJ)* | *Heat production per unit mass of isotope/element ($\mu W\ kg^{-1}$)* |
|---|---|---|---|---|
| $^{238}U$ | 99.27 | $4.46 \times 10^9$ | 7.65 | 95.13 |
| $^{235}U$ | 0.72 | $7.04 \times 10^8$ | 7.11 | 568.47 |
| U | | | | 98.5 |
| $^{232}Th$ | 100 | $1.40 \times 10^{10}$ | 6.48 | 26.3 |
| Th | | | | 26.3 |
| $^{40}K$ | 0.0117 | $1.26 \times 10^9$ | 0.110 | 28.47 |
| K | | | | $3.33 \times 10^{-3}$ |

The table presents recent determinations that account for the energy taken away by neutrinos (Dye, 2012). These values differ slightly from the values commonly used by geoscientists (e.g., Rybach, 1988).

would also place constraints on the radial distribution of the mantle sources (Hochmuth et al., 2007; Mareschal et al., 2012).

In recent years, two groups have reported on their geoneutrino observations. The Kamioka Underground Observatory in Japan has reported on measurements during 9 years of operation. There, the geoneutrino flux is $39 \pm 10$ terrestrial neutrino units (1 TNU amounts to 1 geoneutrino event per $10^{32}$ protons per year exposure time) (Kamland collaboration, 2011). A crustal contribution to $27 \pm 11$ TNU was inferred from a model of the Japanese crust, leaving 12 TNU from the mantle. The 'noise-free' observations made after the shutdown of the Japanese nuclear reactors following the Fukushima accident have provided new estimates of the signal rate at Kamioka. The most recent analysis gives a signal rate of $30 \pm 7$ TNU, which leads to $\approx 7$ TNU from the mantle (Kamland Collaboration (Gando, A., and 45 Collaborators), 2013).

The latest results from the much smaller detector at Borexino, Italy, yield a higher signal rate of $39 \pm 12$ TNU with a crustal component now estimated at 23 TNU (Borexino Collaboration Group (Bellini and 88 Collaborators), 2013). Combining these results leads to a total heat production for uranium and thorium of $14 \pm 8$ TW (**Table 11**). Using an average K/U ratio of 12 000, we add heat generated by potassium and obtain a total heat production of $18 \pm 9$ TW. The difference between the Kamioka and the Borexino values is smaller than previously reported but leaves a large error bar on the mantle contribution. The error is due both to the experimental uncertainty and to the uncertainty on the crustal contribution. These results are remarkable because the observatories were built for particle physics in sites poorly suited to accurately calculate the neutrino flux from a very heterogeneous crust. Neutrino geophysics is still in its infancy, but the results obtained so far give confidence that, with longer exposure times and better statistics in well-located observatories, we shall get robust constraints on the concentration of radioactive elements in the mantle.

### 7.06.5.3 Heat Flux from the Core

The outer core is made of molten iron with very low viscosity and loses heat to the much more viscous deep mantle. Thus, the heat flux out of the core is controlled by the efficacy of mantle convection and cannot be considered as an independent input. Nevertheless, the thermal evolution of the core determines the energy available to drive the geodynamo, which can be constrained from thermodynamics. This question is briefly covered here and the interested reader should consult the volume concerning the core (see in particular Nimmo, **Chapter 8.02**) and some standard references (Braginsky and Roberts, 1995; Gubbins and Roberts, 1987; Labrosse, 2005a,b; Lister and Buffett, 1995), as well as Hernlund and McNamara (**Chapter 7.11**).

An energy balance can be written for the core, in much the same way as for the mantle. The main differences come from electromagnetic processes and chemical buoyancy due to inner core crystallization. The low viscosity maintains the convective state very close to the reference (radially symmetrical) state. The convective velocity at the surface of the core, which is of the order of $10^{-4}\,\mathrm{m\,s^{-1}}$ (Hulot et al., 2002; see also Jackson and Finlay, **Chapter 5.05**), suggests relative density fluctuations of order $10^{-9}$ (Braginsky and Roberts, 1995; Labrosse et al., 1997). Such fluctuations correspond to temperature variations $\delta T \sim 10^{-4}\,\mathrm{K}$ in the absence of other effects. This is much smaller than the secular temperature decrease, implying separation of scales between the upper boundary layer and the interior of the outer core. Thus, for the secular cooling of the core, it is sufficient to consider radial profiles of temperature and concentration, which are usually assumed to be isentropic and uniform, respectively. The very thin boundary layers of the outer core do not affect the bulk energy budget, contrary to those of the mantle.

The energy balance of the core equates the heat flux at the CMB to the sum of secular cooling, $Q_C$; latent heat from inner core crystallization, $Q_L$; compositional energy due to chemical separation of the inner core (often called gravitational energy, but see Braginsky and Roberts, 1995), $E_\xi$; and, possibly, radiogenic heat generation, $Q_H$. Secular cooling makes the inner core grow, which releases latent heat and compositional energy, and the first three energy sources in the balance can be related to the size of the inner core and its growth rate (Braginsky and Roberts, 1995). The current growth rate of the inner core is small (about 300 m $\mathrm{Gy^{-1}}$) and cannot be determined by observation. Thus, one has to resort to indirect means. Energy requirements for the geodynamo do not appear directly in the energy balance for the core because they are accounted for by internal energy transfers, like viscous dissipation in the mantle. The entropy balance, however, depends explicitly on dissipation ($\Phi_c$), which results mostly from Joule heating (ohmic dissipation). Combining the

**Table 11** Present state of geoneutrino observations and estimates of the total radioactivity of the Earth

| | *Geoneutrino flux ($10^6\,cm^{-2}\,s^{-1}$)* | *Total TNU* [a] | *Crust TNU* | *Mantle TNU* | *Heat production of U and Th (total) TW* | *Reference* |
|---|---|---|---|---|---|---|
| Kamioka | $3.4 \pm 0.8$ | $30 \pm 7$ | 23 | 7 | 11.2 | Kamland collaboration (Gando, A. and 45 collaborators), 2013) |
| Borexino | $4.4 \pm 1.4$ | $39 \pm 12$ | 23.5 | 15.5 | 15 | Borexino Collaboration Group (Bellini and 88 Collaborators) (2013) |

The estimated total heat generation includes the crustal contribution but not that of K.

[a]The terrestrial neutrino unit (TNU) corresponds to a flux triggering 1 event per $10^{32}$ protons for an exposure time of 1 year. For Th/U = 3.9, the corresponding neutrino flux is $0.113 \times 10^6\,\mathrm{cm^{-2}\,s^{-1}}$.

energy and the entropy balances, an efficiency equation can be written, which is to leading order (Braginsky and Roberts, 1995; Labrosse, 2003; Lister, 2003):

$$\Phi_c + T_\Phi \Delta S_{cond} = \frac{T_\Phi}{T_{CMB}}\left(1-\frac{T_{CMB}}{T_{ICB}}\right)Q_L + \frac{T_\Phi}{T_{CMB}}\left(1-\frac{T_{CMB}}{T_C}\right)Q_C + \frac{T_\Phi}{T_{CMB}}\left(1-\frac{T_{CMB}}{T_H}\right)Q_H + \frac{T_\Phi}{T_{CMB}}E_\xi \quad [46]$$

where $T_i$ is the temperature at which heat due to process $(i)$ is released and where

$$\Delta S_{cond} \equiv \int \lambda \left(\frac{\nabla T}{T}\right)^2 dV \quad [47]$$

is the entropy production due to heat conduction (see Ricard, **Chapter 7.02**).

Equation [46] shows that the different energy sources on the right-hand side serve to maintain the ohmic and viscous dissipation ($\Phi_c$) produced at temperature $T_\Phi$ as well as the dissipation due to conduction along the isentropic temperature profile ($T_\Phi \Delta S_{cond}$). The latter term is proportional to thermal conductivity, a poorly known physical property at the $(P, T)$ conditions of the core. Until recently, values in the range 20–77 W m$^{-1}$ K$^{-1}$ were used (Gubbins et al., 1982; Labrosse et al., 1997; Lister and Buffett, 1998). Recent measurements and ab initio calculations of electrical conductivity indicate larger values of thermal conductivity in the 84–140 W m$^{-1}$ K$^{-1}$ range at CMB conditions and in the 130–220 W m$^{-1}$ K$^{-1}$ range at the inner core boundary (de Koker et al., 2012; Gomi et al., 2013; Hirose et al., 2011; Pozzo et al., 2012). The rather large spread of values is not due to differences in experimental methods or theoretical calculations but to the uncertainty on core composition. The new conductivity values lead to a lower bound of 9 TW for the heat flux conducted along the isentrope at the CMB. This may be higher than the heat flux across the CMB. Were this to be true, a stable thermal stratification would develop in the upper part of the core and would impede convection and dynamo action.

All the source terms on the right-hand side of the efficiency eqn [46], save for radiogenic heating, are linked to inner core growth and are proportional to its growth rate. Therefore, if ohmic dissipation $\Phi_c$ and radiogenic heat production $Q_H$ can be estimated, one can calculate the inner core growth rate and the heat flux across the CMB.

Ohmic dissipation in the core is dominated by the small-scale components of the magnetic field, which cannot be determined directly because they are screened by crustal magnetic sources (Hulot et al., 1997, 2002). Estimates of this term have therefore relied on dynamo models and scaling relationships. Christensen (2010) had obtained a range of $\Phi_c = 1.1 - 15$ TW (see **Chapter 8.02** by Nimmo, for a more extensive discussion). The uncertainty of this estimate affects the CMB heat flow calculation (**Figure 11**). Taking $\Phi_c = 0$ TW clearly provides the absolute lower bound and implies $Q_{CMB} = 5$ TW, which is lower than the isentropic heat flow of 9 TW. Using their lowest thermal conductivity value for the core, Gomi et al. (2013) found that $T_\Phi \Delta S_{cond} = 1.7$ TW, which is higher than the previous estimates.

The new determinations of core conductivity lead to another argument on the minimum CMB heat flux. As discussed earlier, if the conductive heat flux along the core isentrope is larger than what can be transported by sluggish mantle convection, one expects a stable thermal stratification to develop at the top of the core. This argument must be revised in the presence of compositional convection, however. Including changes of compositional energy due to light element redistribution in the energy balance for any subshell in the core, Gomi et al. (2013) had determined the vertical profile of convective heat flux required to maintain an isentropic temperature profile. Because thermal conductivity increases along a core isentrope, the conductive heat flux along an isentrope reaches a maximum at a depth of about 1000 km below the CMB. With the CMB heat flux at the isentropic value, the downward increase of the conductive heat flux must be balanced by downward convective heat flux in a thick shell at the top of the core. At this point, one can tentatively propose that the actual temperature profile in this layer deviates from an isentrope and becomes stably stratified. Some degree of stable stratification has indeed been proposed at the top of the core but over 300 km at most (see Hirose et al., 2013, for a review). In conclusion, the conductive isentropic heat flux at the top of

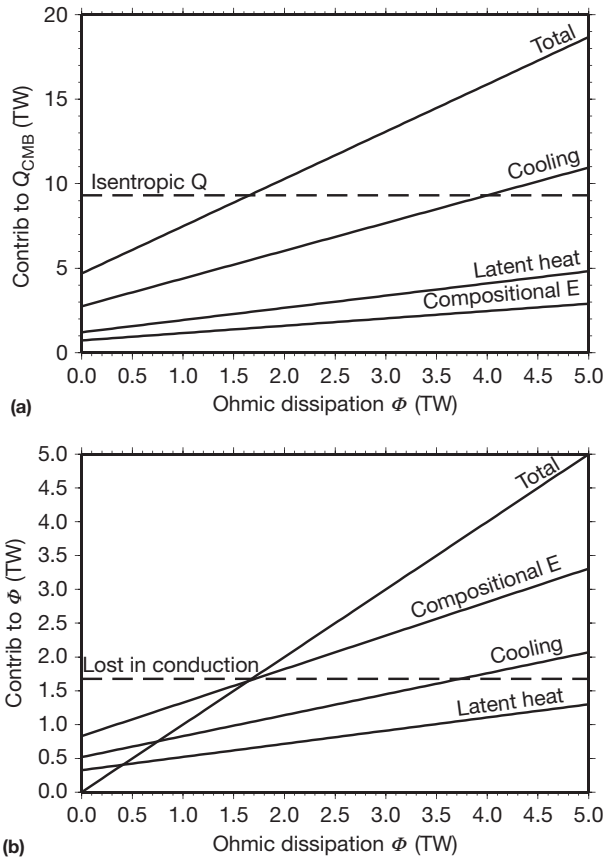


**Figure 11** Contributions to the energy (a) and entropy (b) balance in the core, in the absence of internal heat production. Based on the model of Labrosse (2003) and modified by Gomi et al. (2013) to account for the new estimates of core conductivity.

the core is at least 9 TW and depends on the imperfectly known core composition; this value must be considered a lower bound for the CMB heat flow. Assuming that the CMB heat flux has been maintained at the isentropic value through geologic time, Gomi et al. (2013) had calculated that the core has cooled by at least 750 K in 4.5 Gy, a result with powerful implications that are discussed later.

### 7.06.5.4 Other Sources: Tidal Heating and Crust–Mantle Differentiation

The Earth's rotation is accelerating because of postglacial readjustments, and it is slowing down because of tidal interaction with the moon. The torque exerted on the Moon is due to the lag between the tidal potential and the tidal bulge, which is 2.9° ahead of the potential. In the Earth–Moon system, angular momentum is conserved, but there is a net loss of the rotational and gravitational potential energy. This energy is converted into heat by frictional forces. With laser ranging, the changes in the Earth–Moon distance have been measured accurately (3.7 cm $year^{-1}$), and the slowing down of the Earth's rotation due to tidal interaction with the Moon can be calculated exactly (Bender et al., 1973). The effect of the solar tidal potential on Earth rotation is ≈20% that of the Moon and it must be included in the calculations. The slowing down of the Earth's rotation is $5.4\times10^{-22}$ rad $s^{-1}$ leading to 0.024 ms $year^{-1}$ increase in the length of the day. The energy loss has been calculated to be 3 TW, which must be accounted for by dissipation in the oceans, in the solid Earth, and in the Moon. It is commonly assumed that most of the tidal friction comes from dissipation in shallow seas because dissipation in the deep oceans was shown to be small (e.g., Jeffreys, 1962; Munk and MacDonald, 1960). Lambeck (1977) calculated that dissipation in the seas and oceans must account for 90–95% of the energy dissipation. The contribution of the solid Earth tide depends on the quality factor $Q$ and accounts for <0.1 TW for the values of $Q$ in the mantle suggested by seismology (Zschau, 1986). Such a low value has now found confirmation from satellite observations of the lag between the solid Earth tide (0.16°) and the lunar potential. This observation implies that the dissipation by the solid Earth is 0.083 TW (Ray et al., 1996 see also **Chapter 3.09** by Gross).

Some gravitational potential energy is released by the extraction of continental crust out of the mantle. A rough estimate can be obtained as follows:

$$\delta E_g = \int_c^R g(r) r \delta\rho 4\pi r^2 dr \qquad [48]$$

where $c$ and $R$ are the radii of the core and Earth, respectively, and $\delta\rho$ is the density difference at radial distance $r$. Using a total mass of crust of $2.6\times10^{22}$ kg and mass conservation, $\delta\rho/\rho$ is ≈0.1 in a well-mixed mantle. Neglecting induced changes of the gravity field, we get $\delta E_g \approx 2\times10^{28}$ J. For a constant rate of crustal growth during 3 Gy, the contribution to the energy budget is 0.2 TW, which can be considered as negligible. If the net extraction of crust from the mantle has occurred in a few short episodes, it has induced larger energy pulses. For three or four such episodes of ≈200−300 My duration (Condie, 1998), each pulse may have been as large as 0.6 TW, but this can still be neglected in an analysis of secular cooling. In contrast to the change of gravitational energy due to thermal contraction, most of this energy is converted to heat by viscous dissipation because it involves differential motions between melt and matrix.

### 7.06.5.5 Summary

Various models for the bulk silicate Earth composition lead to results that differ significantly from one another. Uncertainties on the average uranium, thorium, and potassium abundances stem from the propagation of errors through a sequence of elemental ratios and from the correction procedure for depletion effects due to melting. A lower bound on the bulk mantle heat production may be derived from the average MORB mantle source. A large uncertainty remains on the heat flux from the core, but the recently revised core conductivity values impose a higher lower bound than previously thought.

## 7.06.6 Secular Cooling: Constraints on Mantle Temperatures

In this section, we review evidence for secular cooling, starting with present-day evidence and working backward in time. The total heat lost by the mantle is more than all the inputs. Our preferred values for the input and output of energy are 23 and 39 TW, respectively (**Table 12**). The difference 16 TW must be accounted for by the secular cooling of the mantle (**Figure 12**). Addition of all the uncertainties results in an unrealistically wide range (1–28 TW) for the secular cooling. Assuming a constant value for the specific heat of 1250 J $kg^{-1}$ $K^{-1}$, the rate of cooling must be $3.4\times10^{-15}$ K $s^{-1}$ or 106 K $Gy^{-1}$, with a range 7–190 K $Gy^{-1}$.

**Table 12** Mantle energy budget, preferred value and range

| | *TW* | *TW* |
|---|---|---|
| Oceanic heat loss ($300\times10^6$ $km^2$) | 32 | 30–34 |
| Continental heat loss ($210\times10^6$ $km^2$) | 14 | 13–15 |
| Total surface heat loss ($510\times10^6$ $km^2$) | 46 | 43–49 |
| Radioactive sources (mantle + crust) | 18 | 13–23 |
| Continental heat production (crust + lith. mantle) | 8 | 7–8 |
| Heat flux from convecting mantle | 38 | 35–41 |
| Radioactive heat sources (convecting mantle) | 11 | 9–17 |
| Heat from core | 11 | 5–17[a] |
| Tidal dissipation in solid Earth | 0.1 | |
| Gravitational energy (differentiation of crust) | 0.3 | |
| Total input | 23 | 14–34 |
| Net loss (mantle cooling) | 16 | 1–29 |
| Present cooling rate, K $Gy^{-1}$ | 106 | 7–210 |
| Present Urey ratio[b] | 0.29 | 0.12–0.49 |

The distribution in the range is barely known for most cases and the preferred value is simply the middle one. The cooling rate is computed assuming $C_P = 1200$ J $K^{-1}$ $kg^{-1}$.
[a]This range includes estimates from core thermodynamics and inference from the perovskite–postperovskite phase diagram.
[b]Urey ratio for the convecting mantle, leaving out crustal heat sources from both the heat loss and the heat production.

### 7.06.6.1 The Present-Day Mantle Geotherm

The potential temperature of shallow oceanic mantle may be calculated from the composition of MORBs which have not been affected by fractional crystallization, and also from heat flux and bathymetry data, as explained earlier. Such independent determinations are summarized in Table 4 and are in very good agreement with one another. For temperatures at greater depth, one may use seismic discontinuities and the associated solid-state phase changes. This classical method requires specification of the mantle composition, which is usually taken to be pyrolite (Ringwood, 1962). Well-defined discontinuities at depths of 410 and 660 km have been linked to the olivine–wadsleyite transition and to the dissociation of spinel to ferropericlase and magnesiowüstite, the so-called postspinel transition. Other seismic discontinuities have been identified, notably at a depth of about 500 km (Table 13). Some of these are not detected everywhere and seem to have a regional character, and interpretation is still tentative to some extent. Recently, a new phase change relevant to the lowermost mantle has been discovered, from perovskite (Pv) to postperovskite (pPv) (Murakami et al., 2004; Oganov and Ono, 2004; see also Chapter 2.08 by Oganov and Chapter 2.05 by Yuen et al.).

The olivine–wadsleyite phase change has a large Clapeyron slope in a 3–4 MPa $K^{-1}$ range and hence provides an accurate temperature estimate (Katsura et al., 2004). Errors on temperature arise from the experimental data and from small differences in the depth of the seismic discontinuity. In addition, in a multicomponent material such as the mantle, there exists a transition region whose thickness depends on composition (Stixrude, 1997). Accounting for these effects, the temperature estimate at 410 km is $1760 \pm 45$ K for a pyrolytic upper mantle. Isentropic profiles that pass through these ($P$, $T$) values (Figure 13) correspond to potential temperatures in the range 1550–1650 K (Katsura et al., 2004), in very good agreement with the independent estimates from the composition of MORBs and heat flux data (Table 4).

Laboratory studies have cast doubt on the postspinel transition pressure (Irifune and Isshiki, 1998; Katsura et al., 2003). Furthermore, this transition may have a very small Clapeyron slope (as small as $-0.4$ MPa $K^{-1}$ according to Katsura et al. (2003)), implying that small uncertainties on pressure lead to large errors on the transition temperature. For these reasons, one should treat temperature estimates for this transition with caution. Nevertheless, the uncertainty often quoted for this value is similar to that for the 410 km discontinuity, and the

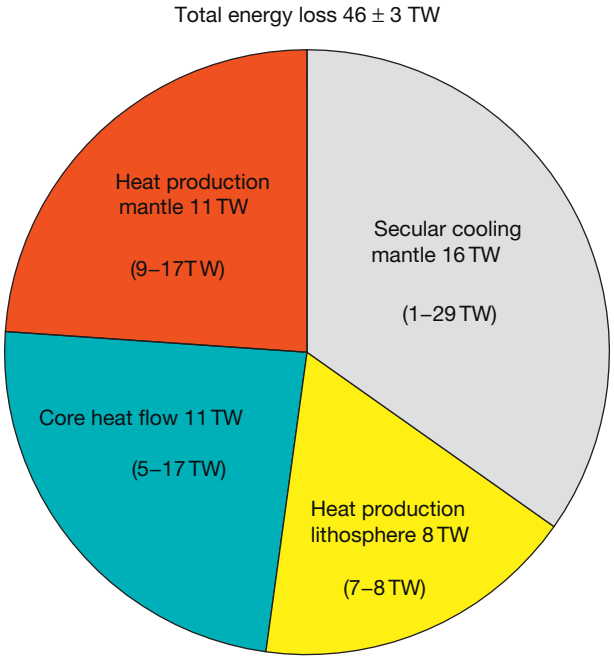


**Figure 12** Proposed breakdown of the present energy budget of the Earth. With continental lithosphere, mantle heat production, and core heat loss constrained, the mantle cooling rate is adjusted to fit the total energy loss.

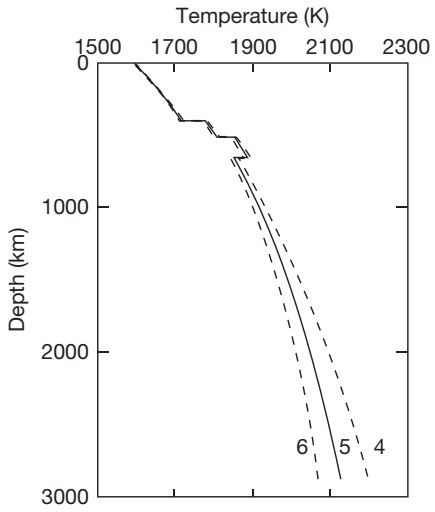


**Figure 13** Isentropic temperature profiles in the mantle for different values of the Anderson–Grüneisen parameter, as labeled. Reproduced from Katsura T, et al. (2004) Olivine–Wadsleyite transition in the system $(Mg,Fe)SiO_4$. *Journal of Geophysical Research* 109: B02209.

**Table 13** Anchor points for the mantle geotherm

| *Boundary* | *Depth (km)* | *Temperature (K)* | *Reference* |
|---|---|---|---|
| MORB generation | 50 | 1590–1750 [a] | Kinzler and Grove (1992) |
| Olivine–wadsleyite | 410 | $1760 \pm 45$ | Katsura et al. (2004) |
| Postspinel | 660 | $1870 \pm 50$ | Katsura et al. (2003, 2004) |
| Core–mantle | 2900 | $4080 \pm 130$ | Alfé et al. (2002) and Labrosse (2003), this paper |

[a]True range of temperatures in the shallow mantle.

present-day 'best' value for the mantle temperature at a depth of 660 km is 1870 ± 50 K (Ito and Katsura, 1989; Katsura et al., 2003, 2004).

The other major discontinuity, the core–mantle boundary, is a chemical boundary and its temperature can be computed from the core side. Once again, the method relies on a phase change, in this case the solidification of iron at the inner core boundary. Using ab initio calculations, Alfé et al. (2002) had determined that the melting temperature of pure Fe is in the range 6200–6350 K. Experiments by Anzellini et al. (2013) up to a pressure of 200 GPa are compatible with this value. In the presence of light elements (O, Si, and S), the liquidus temperature at the inner core boundary is lowered by 700 ± 100 K. The outer core can be assumed to be very close to isentropic (e.g., Braginsky and Roberts, 1995), and the variation in temperature can be linked to the variation in density by (e.g., Poirier, 2000)

$$\left(\frac{\partial T}{\partial \rho}\right)_S = \gamma \frac{T}{\rho} \qquad [49]$$

where $\gamma$ is the Grüneisen parameter (see **Chapter 7.02**). According to the theoretical calculations of Vočadlo et al. (2003; see also Vočadlo, **Chapter 2.06**), $\gamma = 1.5 \pm 0.01$ throughout the core. We may therefore assume that $\gamma$ is constant and integrate eqn [49]:

$$T_{CMB} = T_{ICB}\left(\frac{\rho_{CMB}}{\rho_{ICB}}\right)^{\gamma} = 0.73 T_{ICB} \qquad [50]$$

which relates the temperature at the CMB to that at the ICB and to density structure. Using $\gamma = 1.5$ and density values from the preliminary reference Earth model (PREM) of Dziewonski and Anderson (1981; see also Dziewonski and Romanowicz, **Chapter 1.01**), we obtain a range of 3950–4220 K for the temperature at the top of the core. This does not account for uncertainties in the PREM density values, and the range is narrower than the full range of published values, but a full discussion of all the different estimates is outside the scope of this chapter.

Strong constraints on temperatures above the CMB have been deduced from studies of the Pv to pPv phase change, provided that it takes place in the mantle (Murakami et al., 2004; Oganov and Ono, 2004; see also Irifune, vol. 2). According to the experiments of Tateno et al. (2009), this phase change has a Clapeyron slope of 13.3 ± 1.0 MPa $K^{-1}$ and a temperature of 3520 ± 70 K at the CMB pressure. A key feature is that it is likely to occur in the so-called $D''$ boundary layer at the base of the mantle. With a simple model for the radial temperature profile in this boundary layer, Hernlund et al. (2005; see also **Chapter 1.22** by Lay and Hernlund and McNamara, **Chapter 7.11**) predicted that the phase change boundary should be crossed twice in cold regions of the mantle (**Figure 14**) and should not be crossed in hot regions, which seems to be consistent with seismic observations. As illustrated in **Figure 14**, a double crossing of the phase boundary implies that the temperature gradient at the base of the mantle is higher than that of the Clapeyron diagram. It also implies that the temperature at the CMB must be higher than that of the phase change at that pressure (Hernlund and Labrosse, 2007). This provides us with a lower bound of 3700 K on the CMB temperature (Tateno et al., 2009), which is consistent with estimates obtained from the core side. Lateral variations of the depth of discontinuity that are determined by seismological observations imply lateral temperature differences of ≈1500 K in the lowermost mantle (Hirose, 2006).

Paired seismic discontinuities have also been detected in hot regions near the core–mantle boundary beneath the Pacific Ocean (Lay et al., 2006). These can be reconciled with the model of Hernlund et al. (2005) if these regions are enriched in iron. Using a model for the boundary layer above the core–mantle boundary and a thermal conductivity value of 10 $Wm^{-1}K^{-1}$, Lay et al. (2006) had estimated that the heat flux across the CMB is at least 13 ± 4 TW.

The interpretation of $D''$ discontinuities as due to the Pv to pPv phase transition has been challenged by several experimental studies. Catalli et al. (2009), Andrault et al. (2010), and Grocholski et al. (2012) had found that the Pv and pPv phases can stay in equilibrium with each other over a wide pressure range, which is not consistent with the sharpness of

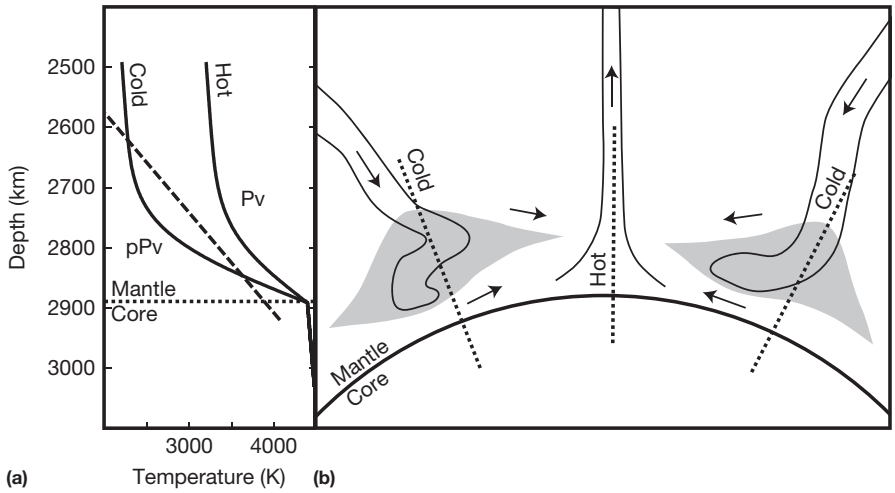


**Figure 14** Sketch of postperovskite lenses in cold regions of the lowermost mantle from Hernlund et al. (2005). (a) Schematic temperature profiles for 'cold' and 'hot' regions (plain curves) superimposed onto the phase boundary. (b) Sketch of thermal boundary layer at the base of the mantle with convective downwellings and upwellings.

the seismic discontinuity. These results are in direct contradiction with those of Tateno et al. (2009) who reported a sharp phase transition. The region of Pv–pPv coexistence could extend through the whole $D''$ layer and, for some mantle compositions, could be found at pressures higher than that of the CMB (Grocholski et al., 2012).

### 7.06.6.2 Temperature Versus Time

One may use petrologic constraints to investigate past temperatures of the mantle. Continental crustal material was different in the Archean than it is today. Basaltic lavas exhibit systematic compositional trends with time, including a secular decrease in average MgO content. MgO-rich ultramafic lavas named komatiites are common in the Archean and are almost absent from today's rock record. Early workers proposed that komatiites require the mantle source to be at least 300 K hotter than present (Green, 1975; Sleep, 1979), but they considered dry mantle only. The peridotite solidus depends strongly on water content, which in turn depends on the geologic setting. If komatiites are generated by mantle plumes, involving mantle that is essentially dry, that is, such that its water content is so small that it does not affect phase boundaries, one deduces that mantle plume temperatures have decreased by about 300 K in 3 Gy (Nisbet et al., 1995). Jarvis and Campbell (1983) suggested that such hot mantle plumes did not require the Archean mantle to be more than 100 K hotter than present on average. According to an alternative hypothesis, komatiites are generated in a subduction environment, involving mantle hydrated by downgoing plates. In that case, one is led to conclude that this part of the mantle was only slightly hotter ($\approx$100 K) in the Archean than it is today (Grove and Parman, 2004). In both cases, komatiites do not sample 'average' mantle and it is not clear how to incorporate these temperature estimates in models for the entire mantle.

Mid-ocean ridge tholeiites are better suited for studies of the mantle's average temperature because they can be sampled over very large areas. They are a compositionally heterogeneous group, however, which translates into a wide temperature range ($\approx$200 K) (Kinzler and Grove, 1992; Klein and Langmuir, 1987). Abbott et al. (1994) calculated the liquidus temperature for Phanerozoic MORBs and Archean MORB-like greenstones and determined the maximum and minimum mantle potential temperatures versus time. Although the range of temperatures for each period is wide ($\approx$200 K), the trend is well marked. Abbott et al. (1994) concluded that mantle temperatures decreased by $\approx$150 K since 3 Gy, which is less than the range of mantle potential temperatures at a given time. Work by Herzberg et al. (2010) on non-arc basaltic rocks, which are again chosen because they were melts of the ambient mantle, confirms these values (Figure 15). A cooling rate of 50 K Gy$^{-1}$ for the mantle represents $\approx$8 TW.

### 7.06.6.3 Early Earth

A full description of the Earth's thermal evolution must include the initial conditions. Here, 'initial' refers to the time when the Earth had completed its main phase of core–mantle differentiation and the mantle had solidified to the point where its dynamics can be described as subsolidus convection. Before reaching that point, a host of processes with different dynamics occurred. They may be separated in three categories: accretion, core formation, and magma ocean crystallization. The process of the formation of the Earth brought together matter that was originally dispersed in the protosolar nebula, thereby releasing gravitational energy. One may estimate the total energy released by taking the difference between the total gravitational energies before and after. The fate of this energy, however, depends on the way it is dissipated and transformed into another type of energy. The effect of core differentiation is quite different from that of accretion. Most of the processes involved remain speculative to some extent, and we restrict our discussion to the points that are directly relevant to the early thermal structure. Several review articles (e.g., Stevenson, 1989; Wetherill, 1990, several articles in vol. 9), and two books (e.g., Canup and Righter, 2000; Newsom and Jones, 1990) deal with these issues in detail.

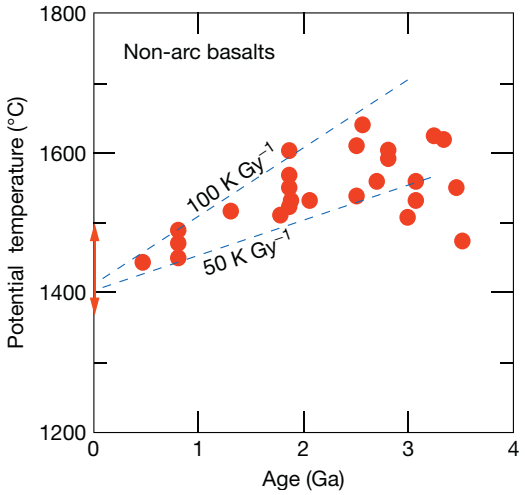


**Figure 15** Temperature of the source of non-arc basaltic rocks as a function of age. The vertical arrow at zero age stands for the range of mantle potential temperature estimates from Table 4. Most of the data fall between the 50 K Gy$^{-1}$ and the 100 K Gy$^{-1}$ lines. Data from Herzberg et al. (2010).

During accretion, the gravitational energy of impactors is first transformed into kinetic energy and then dissipated in the form of heat at the impact. One may define two limit cases. If no energy is lost to space or stored as elastic energy, the temperature of the whole Earth is raised by an amount equal to

$$\Delta T = \frac{-E_g}{MC_P} \sim 3.75 \times 10^5 \text{K} \qquad [51]$$

which would be sufficient to vaporize the whole planet. A large fraction of the impact energy, however, is released at shallow levels and lost to space by radiation. Stevenson (1989) estimated that, if all the energy is made available for radiation, accretion would raise the temperature of the Earth by $<$70 K relative to that of the nebula. The actual evolution lies somewhere between these two limiting cases, involving partial dissipation of the impact energy within the planet and radiative heat transfer through the primordial atmosphere. One important

factor is the size of the impactors. 'Small' impactors, which are much smaller than the target, account for the vast majority of impacts on Earth after the planetary embryo stage (Melosh and Ivanov, 1999). The depth of energy release increases with the size of the impactor and one key variable is the ratio between the time for energy transport to the surface and the time between two impacts. During accretion, evolution toward larger and fewer impactors has two competing effects: energy gets buried at greater depth while the time between two impacts increases, which enhances heat loss to the atmosphere. Assuming heat transport by diffusion, Stevenson (1989) concluded that typical accretion scenarios lead to significant energy retention within the planet. The extreme case is that of the giant impact thought to be at the origin of the Moon. Calculations suggest that the whole Earth temperature was raised to as high as 7000 K (Cameron, 2001; Canup, 2004). In such conditions, the whole Earth melted and parts of it were vaporized to form a thick atmosphere. The question of whether or not previous impacts were able to melt the Earth becomes irrelevant.

The formation of the core also has important energetic implications. Some gravitational energy is released by going from a homogeneous material to a stratified core–mantle system. Kinetic energy plays no role in this process, in contrast to the accretionary sequence, and gravitational potential energy is dissipated by viscous heating in both the iron and the silicate phases. Flasar and Birch (1973) estimated that this process would heat the whole Earth by about 1700 K. This estimate relies on the bulk difference in gravitational energy between the initial and the final states and hence gives no information on where energy gets dissipated. We know now that iron–silicate differentiation occurred very early in the solar system and affected planetesimals (Kleine et al., 2002). Clearly, core formation within planetesimals and in the Earth after the giant impact involves different dynamics. In large-scale models of the giant impact, the cores of the two protoplanets merge with little mixing with silicates (Canup, 2004). An iron emulsion may form in the molten silicate, however, due to a combination of the Rayleigh–Taylor and Kelvin–Helmholtz instabilities (Ichikawa et al., 2010; Rubie et al., 2003).

Several mechanisms have been proposed for core formation (e.g., Stevenson, 1990; Rushmer et al., 2000; see also Rubie **Chapter 9.03**): percolation of liquid metal through a compacting solid silicate matrix, iron droplets 'raining' through a magma ocean (Ichikawa et al., 2010), diapirs generated by Rayleigh–Taylor instability at a rheological interface, and hydraulic fracturing (Stevenson, 2003). All these mechanisms may have been active simultaneously or in succession at different times (Golabek et al., 2008; Ricard et al., 2009; Šrámek et al., 2010). They have different implications for dissipation. For example, percolation and compaction can explain core formation in planetesimals and planetary embryos (Šrámek et al., 2012). On planets larger than about the size of Mars, the same process can operate locally below impact sites and generate a metallic diapir, which sinks into the deeper mantle once enough metal has accumulated. Gravitational energy release during descent leads to further melting and can trigger runaway core growth (Monteux et al., 2009; Ricard et al., 2009).

For a Newtonian rheology, the amount of viscous heating is $\phi \sim \eta U^2/L^2$, where $\eta$ is the viscosity of the fluid phase, which may be silicate or iron, and $U$ and $L$ are the scales for velocity and length. In the case of an iron diapir, the velocity and length scales are the same for the metal and silicate phases, but the viscosity of the former is several orders of magnitudes lower. Viscous heating is thus concentrated in the silicate phase and produces little heating of the iron phase because the heat diffusion timescale is less than the descent timescale. This would differentiate a core that is initially colder than the lower mantle. In the case of interstitial flow, the small size of iron veins makes heat diffusion very effective and thermal equilibration with the surrounding silicate phase likely. In the case of iron droplets raining down through molten silicate, the droplet size is set by a balance between surface tension and viscous drag and is typically 1 cm (Ichikawa et al., 2010; Ulvrová et al., 2011). Thus, one also expects thermal equilibrium between metal and silicate. With these two last mechanisms, the metallic core is generated at the temperature of the lower mantle. In the model of Ricard et al. (2009), the diapir is in fact a two-phase mixture of liquid metal and solid silicate that remain in thermal equilibrium. This type of diapir heats up the surrounding solid silicate during descent. The resulting thermal structure is that of a hot core and lower mantle, a cool midmantle, and a hot upper mantle. Thus, the Earth's initial thermal structure depends strongly on the mechanism of core formation and cannot be specified with certainty yet.

### 7.06.6.4 Magma Ocean Evolution

Both the giant impact and core formation generated temperatures that were high enough for the entire silicate Earth to be molten. Cooling and crystallization of such a thick magma ocean involve heat transfer through the primordial atmosphere, convection, rotation, and crystal–melt separation. Available models have been aimed mostly at determining the extent of chemical stratification at the end of crystallization (Abe, 1997; Solomatov, 2000).

At the scale of the whole Earth's mantle, solidification and crystal–melt separation involve pressure-dependent properties that vary by large amounts from top to bottom. Current knowledge on a few of these is not sufficient to draw firm conclusions on magma ocean evolution. Starting from a fully molten mantle where crystallization begins, for example, depends on the respective slopes of the liquidus and the isentrope. We know that the liquidus is steeper than the isentrope over about 1000 km at the top of the mantle, but the reverse may be true at greater depths (Andrault et al., 2011; Fiquet et al., 2010; Thomas et al., 2012). An equally important variable is the density difference between melt and solid at equilibrium, which controls the manner of solid–liquid segregation. The standard magma ocean scenario postulates that crystallization proceeds from the bottom upward, which requires that crystals sink through melts at all depths. Melts are less dense than solids at low pressures, but the large compressibility of liquids compared to that of crystals implies that the latter could be buoyant with respect to silicate melts in the lower mantle (Andrault et al., 2012; de Koker et al., 2013; Nomura et al., 2011; Thomas et al., 2012). In this case, there might have been two different magma oceans in the early Earth at the top and bottom of the mantle, separated by a growing solid midmantle horizon (Labrosse et al., 2007).

The low viscosity of the melt and the size of Earth imply highly turbulent convective flows and rapid cooling, such that

the magma ocean at the surface solidifies in a few thousand years (Abe, 1997). A basal magma ocean, on the other hand, would cool at a much slower rate due to sluggish heat transfer across the solid mantle and could still contain isolated pockets of partial melt today (Labrosse et al., 2007). This would account for the ultralow-velocity zones that have been found above the CMB (Williams and Garnero, 1996).

Turning to the evolution of a surficial magma ocean, one must account for two rheological transitions, from pure magma to slurry (crystals suspended in a magma) and from slurry to mush (interconnected crystals forming a compacting matrix), which affect the convection regime and the cooling rate. Starting from a superheated melt at temperatures above the liquidus, the initial phase has a solid growing at the base and a fully molten upper layer that becomes thinner as cooling proceeds. A first transition occurs when the fully molten layer vanishes. At this stage, the Earth is made of a partially crystallized magma ocean that may lie over already fully solidified mantle. The radial temperature profile is tied to the solidus that has a steeper slope than the isentrope. Such a thermal stratification is unstable and leads to the convective overturn of the solid layer (Elkins-Tanton et al., 2003). The two layers evolve at vastly different timescales because of their different rheologies. The bulk cooling rate is set by the heat loss through the Earth's surface, which is controlled by the dynamics of the partially crystallized magma ocean at the top. In this second phase, heat transport occurs mostly by melt–solid separation and solidification proceeds from the bottom up. The fully solidified layer at the base of the magma ocean thickens rapidly and eventually becomes unstable. Convective overturn is slower than the cooling of the magma ocean and may be considered as a separate event that leads to decompression melting and the formation of a secondary magma ocean at the surface and possibly at the bottom of the mantle. The process of cooling and solidification of this magma ocean then repeats itself. This regime prevails until the shallow magma ocean reaches the rheological threshold between liquid behavior and solid behavior, which probably occurs at a crystal fraction of about 60%. At this stage, the shallow partially crystallized layer becomes strongly coupled to the solid mantle below and cooling proceeds through bulk convection everywhere. According to Abe (1993, 1997), this was completed in a few 10 My (**Figure 16**) and sets the initial conditions for secular cooling models of the solid Earth. From the most recent phase diagrams (Herzberg and Zhang, 1996; Litasov and Ohtani, 2002), the final rheological transition corresponds to a potential temperature of about $1800 \pm 100$ K for a mantle composed of dry pyrolite (**Figure 17**).

Recent advances in geochemistry have confirmed the theoretical estimates of Abe (1997). Caro et al. (2003) had found evidence that pushes early crust formation as far back as 4.4 Gy. Others have argued that liquid water was present on the Earth's surface at 4.3 Gy (Mojzsis et al., 2001). These studies cannot demonstrate that plate tectonics was already active at such early times, but provide some support for a solid upper mantle.

### 7.06.6.5 Average Secular Cooling Rate of the Mantle

Subsolidus convection began at a mantle potential temperature of about $1800 \pm 100$ K, which exceeds the present-day temperature by about 200 K. This constrains the average cooling rate of the Earth even if the timing is not known precisely. These various constraints lead to an average cooling rate of about 50 K $Gy^{-1}$ that is consistent with changes in the compositions of erupted lavas (Abbott et al., 1994; Herzberg et al., 2010).

The present-day mantle potential temperature is fixed at about 1600 K by a fit to heat flux and bathymetry data independently of petrologic constraints and in particular of the

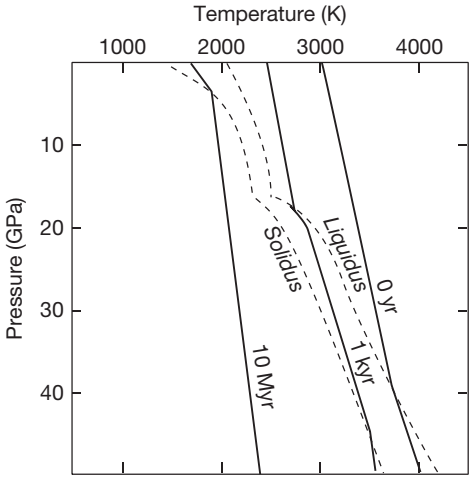


**Figure 16** Three geotherms at different times in the early Earth. The timescale for the thermal evolution is set by heat loss at the upper boundary that decays rapidly with temperature. At about 10 My, the solid content in the partially molten upper mantle layer reaches the threshold value of 60%, which marks the cessation of liquid behavior. After that time, convection is in the subsolidus regime controlled by solid behavior that still prevails today. Adapted from Abe Y (1997) Thermal and chemical evolution of the terrestrial magma ocean. *Physics of the Earth and Planetary Interiors* 100: 27–39.

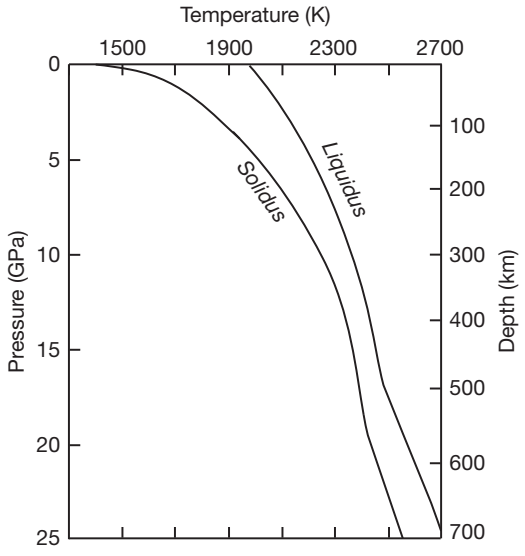


**Figure 17** Solidus and liquidus for dry pyrolite as a function of pressure. Adapted from Litasov K and Ohtani E (2002) Phase relations and melt compositions in CMAS–pyrolite–$H_2O$ system up to 25 GPa. *Physics of the Earth and Planetary Interiors* 134: 105–127.

water content of mantle rocks (McKenzie et al., 2005). If the mantle contained significant amounts of water at the end of the magma ocean phase, however, the phase diagram must be shifted to lower temperatures. One consequence is that the potential temperature at the beginning of subsolidus convection was lower than the 1800 K estimate used earlier. In this case, the average cooling rate must be even $< 50\ \mathrm{K\ Gy^{-1}}$.

#### 7.06.6.6 Summary

At the end of accretion and core–mantle separation, a magma ocean probably extended through a large fraction of the silicate Earth. Because of its small viscosity, it cooled and crystallized rapidly, which led to a stratified mantle with a solid lower layer and a partially crystallized upper layer. At the start of solid-state mantle convection, upper mantle temperatures were such that the surficial partially molten region had a solid fraction of about 60%. This sets the initial temperature of the solid Earth to a value that is about 200 K higher than the present.

### 7.06.7 Thermal Evolution Models

#### 7.06.7.1 The Urey Ratio

The decay time of the bulk radiogenic heat production, which is the weighted average of the individual decay times of the four relevant isotopes (Table 9), is 3 Gy. Thus, over the Earth's history, heat sources have decreased by a factor of about 4. The efficiency of the Earth's convective engine in evacuating heat generated by radioactive decay is commonly measured by the Urey ratio, *Ur*, which is the ratio of heat production over heat loss:

$$Ur = \frac{\int_V H \mathrm{d}V}{-\int_A \mathbf{q}\cdot\mathbf{n}\mathrm{d}A} \qquad [52]$$

To calculate this ratio, we do not take continental heat sources into account because they are stored in the continental lithosphere and hence are not involved in mantle convection. Using the data of Table 12, we find that $Ur = 0.29$, with a range of 0.12–0.49.

The heat budget of Table 12 allows calculation of the present-day cooling rate. Secular variations of basalt compositions and consideration of initial thermal conditions provide constraints on the total temperature drop over the Earth's history and hence on the average cooling rate (Figure 15). Thus, physical models are not needed to determine how the Earth has cooled down. Instead, the data allow a test of our understanding of mantle convection processes, and available constraints on the cooling rate can be turned into one for how the rate of heat loss has changed through time. The global heat balance reads as

$$M\langle C_\mathrm{p}\rangle \frac{\mathrm{d}T}{\mathrm{d}t} = -Q + H \qquad [53]$$

where $M$ is the mass of the Earth and $\langle C_\mathrm{p}\rangle$ an 'effective' heat capacity that accounts for the isentropic variation of temperature with depth. Integrating over the age of the Earth, one deduces that

$$\frac{\overline{Q} - \overline{H}}{Q - H} = \frac{(\mathrm{d}T/\mathrm{d}t)_\mathrm{av}}{\mathrm{d}T/\mathrm{d}t} \qquad [54]$$

where $\overline{Q}$ and $\overline{H}$ are the time-averaged values of heat loss and heat production and $(\mathrm{d}T/\mathrm{d}t)_\mathrm{av}$ is the average cooling rate. The cooling rate has an average value of about $50\ \mathrm{K\ Gy^{-1}}$ (i.e., about 200 K over 4 Gy; see Section 7.06.6.6) and a larger present-day value (about $120\ \mathrm{K\ Gy^{-1}}$). Thus, the ratio in eqn [54] is $< 1$ and probably as low as 0.4. This implies that the rate of heat loss has decreased less rapidly than that of heat production.

#### 7.06.7.2 'Parameterized' Cooling Models

The characteristics of convection in well-mixed homogeneous layers are well understood and have been used to develop secular cooling models for Earth. Here, we briefly recapitulate a few important results and set up the stage for further discussion with simple arguments. With constant physical properties, the heat flux through the top boundary of a convecting layer is a function of the temperature difference across that layer (e.g., Davies, 1980a,b; Schubert and Young, 1976; Sharpe and Peltier, 1978). A very robust scaling law relates the dimensionless heat flux (i.e., the Nusselt number) to the Rayleigh number:

$$Nu = \frac{Q/A}{kT/D} = C_1 Ra^{\beta} \qquad [55]$$

where $C_1$ is a proportionality constant, $Q/A$ the heat flux, $A$ the surface area, $T$ the temperature difference across the layer, $D$ the layer thickness, and $Ra$ the Rayleigh number:

$$Ra = \frac{g\alpha T D^3}{\kappa \nu_\mathrm{M}} \qquad [56]$$

where $\nu_\mathrm{M} = \mu_\mathrm{M}/\rho$ is the kinematic viscosity. This relationship can be turned into an equation for heat loss $Q$ of the form

$$Q = C_2 T^{1+\beta} \nu_\mathrm{M}^{-\beta} \qquad [57]$$

where the constants $C_2$ and $\beta$ are obtained from boundary layer theory as well as laboratory experiments (Howard, 1964; Olson, 1987; Turcotte and Oxburgh, 1967). This relationship is valid if, and only if, instability always occurs in the same conditions, for example, when a Rayleigh number defined locally in the boundary layer exceeds a critical value. Cooling models of this kind have been termed 'parameterized' because they collapse all the physics of mantle convection into a single equation involving only temperature and two dimensionless parameters, $C_2$ and $\beta$. Typically, $\beta = 1/3$, such that heat loss is governed solely by local instabilities of the upper boundary layer. The value of constant $C_2$, but not that of exponent $\beta$, depends on the instability threshold and on the length of the convective cell (Grigné et al., 2005; Olson, 1987).

One additional parameter is required to account for the strong dependence of viscosity on temperature. Secular cooling implies that the mantle viscosity increases with time, which slows down convection and decreases the cooling rate. One can approximate an Arrhenius law for viscosity by an equation of the form $\nu = \nu_0 (T/T_0)^{-n}$, with $n \sim 35$, which is valid for $T \sim T_0$ (Christensen, 1985; Davies, 1980a,b). The thermal evolution equation then takes the following form:

$$M\langle C_p\rangle\frac{dT}{dt}=-Q_0\left(\frac{T}{T_0}\right)^{1+\beta(1+n)}+H(t) \quad [58]$$

where $Q_0$ is the heat loss at the reference potential temperature $T_0$. Temperature changes in the Earth are small compared to the absolute temperature (i.e., $\approx$200 K for a present-day temperature of $\approx$1600 K). One may thus linearize the thermal evolution equation:

$$T=T_0+\Theta, \text{ with } \Theta \ll T_0 \quad [59]$$

$$M\langle C_p\rangle\frac{d\Theta}{dt}=-Q_0\left[1+\frac{\Theta}{T_0}(1+\beta+\beta n)\right]+H(t) \quad [60]$$

For simplicity, we assume that heat production decreases exponentially with time, such that $H(t)=H_0\times\exp(-t/\tau_r)$, where $\tau_r\approx 3$ Gy. The solution of eqn [60] is

$$\Theta=\Theta_0\times\exp(-t/\tau_p)+\frac{Q_0\tau_p}{M\langle C_p\rangle}(\exp(-t/\tau_p)-1)+\frac{H_0\tau_p\tau_r}{M\langle C_p\rangle T_0(\tau_r-\tau_p)}(\exp(-t/\tau_r)-\exp(-t/\tau_p)) \quad [61]$$

where we introduce the convective relaxation time $\tau_p$:

$$\tau_p=\frac{M\langle C_p\rangle T_0}{(1+\beta+\beta n)Q_0} \quad [62]$$

Using standard values for the parameters and variables involved, $n=35$, $\beta=1/3$, $M=6\times10^{24}$ kg, $Q_0=30$ TW, $T_0=1300$ K (the temperature jump across the boundary layer is the relevant parameter here), and $\langle C_p\rangle=1200\,\mathrm{J\,kg^{-1}\,K^{-1}}$, the thermal relaxation time is about 800 My.

Equation [61] for the average mantle temperature depends on a number of parameters. We can summarize simply the constraints brought by observations by noting that, for $t\gg\tau_p$,

$$Ur\rightarrow\frac{(\tau_r-\tau_p)}{\tau_r} \quad [63]$$

For $\tau_p=800$ My and $\tau_r=3$ Gy, $Ur=0.75$, which is much larger than the values derived earlier. In order to meet the constraint of the Urey ratio, one must increase the adjustment time of mantle convection. Rephrased differently, this states that the rate of heat loss does not keep up with the decrease of radiogenic heat production. We have reached the same conclusion in the previous section with a completely different argument on the difference between the secular average and the present-day values of the cooling rate.

In order to increase the adjustment time of mantle convection, one option is to appeal to a layered mantle (McKenzie and Richter, 1981). Another option is to decrease the value of exponent $\beta$. According to Christensen (1984, 1985), this may be a consequence of the temperature dependence of viscosity. For very large variations of viscosity, however, convection occurs in the stagnant lid regime (e.g., Davaille and Jaupart, 1993; Ogawa et al., 1991; Solomatov and Moresi, 1997). In this case, plate tectonics is shut off, which is not a satisfactory solution. There may be an intermediate regime with subduction of the very viscous lid, such that $\beta=0.293$ (Solomatov and Moresi, 1997), but this $\beta$ value is too large to meet the constraint of the Urey ratio. In an attempt to account for the resistance to plate bending at subduction zones, Conrad and Hager (1999) had suggested that $\beta\sim0$. Following a similar line of reasoning and building on a study by Sleep (2000), Korenaga (2003) pushed the argument further by introducing variations of plate rigidity due to changes in the depth and degree of melting as the mantle cools down. He proposed that $\beta$ is in fact negative. In accurate models of compressible mantle convection, however, dissipation due to plate bending accounts for $<10\%$ of the total dissipation and has little impact on the value of $\beta$ (Leng and Zhong, 2010). Furthermore, there is no evidence that resistance to bending actually limits subduction on Earth. For example, no correlation exist between the slab dip (which specifies the radius of curvature of the plate at the trench and hence the extent of bending) and the magnitude of slab pull or the convergence rate (Lallemand et al., 2005).

'Parameterized' models rely on strong assumptions on plate size and/or subduction age, which are difficult to test and which may not be valid. One important point is that, after about 2 Gy, temperatures from eqn [61] are not sensitive to the initial conditions, which has two implications. One is that failure to reproduce the present-day Urey ratio cannot be blamed on the poorly known initial condition. The other implication is that 'backward' thermal calculations starting from the present become unreliable for old ages.

We now describe several features of the Earth's convective system that make it quite distinctive. We discuss the relevance of heat loss 'parameterizations' and evaluate whether the present-day heat balance is representative of the secular evolution of Earth, which, by definition, only involves long-term changes.

### 7.06.7.3 The Peculiarities of Mantle Convection: Observations

Convection in the Earth's mantle proceeds in peculiar ways. One distinctive feature is the triangular age distribution of the seafloor (**Figure 7**; Becker et al., 2009; Labrosse and Jaupart, 2007; Parsons, 1982), which is at odds with other convecting systems as well as with the parameterized schemes discussed earlier. We show in **Appendix H** the age distribution at the upper boundary of several convective layers. None of them resemble that of Earth, which illustrates current limitations in reproducing mantle convection processes.

A few other peculiar features of mantle convection are worth mentioning. Heat loss is unevenly distributed at the surface. The Pacific Ocean alone accounts for almost 50% of the oceanic total and 34% of the global heat loss of the planet. This is due in part to the large area of this ocean and in part to its high spreading rate. Oceanic plates are transient, such that changes of oceanic heat loss may occur when a new ridge appears or when one gets subducted. For example, the heat flux out of the Atlantic Ocean is about 6 TW, 17% of the oceanic total (Sclater et al., 1980). This ocean has almost no subduction and started opening only at 180 My. At that time, the generation of a new mid-ocean ridge led to an increase of the area of young seafloor at the expense of old seafloor from the other oceans and hence to enhanced heat loss. From the standpoint of dynamics, the most challenging features of mantle convection are perhaps the large variations of plate speeds and dimensions that exist. With the small number of

plates present, averaging values of spreading velocity and plate size may well be meaningless.

One key feature of Earth is the presence of large continents at the surface, which play an important role. They do not allow large heat fluxes through them and generate boundaries with complicated shapes that constrain mantle flow. They exert a strong control on secular cooling and may well be responsible for the triangular distribution of ocean floor ages (Coltice et al., 2012; Grigné and Labrosse, 2001; Labrosse and Jaupart, 2007; Lenardic et al., 2005).

### 7.06.7.4 Convection with Oceanic Plates

Controls on the Earth's heat loss are direct consequences of the convection regime. To derive an equation for heat loss on Earth, we focus on the oceans. In continents, crustal radioactivity accounts for a large fraction of the surface heat flux, such that the basal heat flux out of the convecting mantle is very small. Continental radioactivity plays no dynamic role and we may thus, as a first approximation, equate the heat loss of Earth to that of the oceans. For the sake of simplicity, we specify the heat flux using a half-space cooling model. Predictions from that model differ from observations at old ages only, and the difference represents a small fraction of the total: changing heat loss through seafloor older than 80 My by 30% (an overestimate) impacts the total planetary value by only 6%. Thus, we assume that $q=\lambda T_M/\sqrt{\pi\kappa\tau}$. For a rectangular plate of velocity $U$ and width $l$, heat loss $Q_P$ is

$$Q_P=\int_A q\mathrm{d}A=\int_0^{\tau_m} qlU\mathrm{d}\tau=2\frac{\lambda}{\sqrt{\pi\kappa}}T_M Ul\sqrt{\tau_m} \qquad [64]$$

where $\tau_m$ is the maximum plate age. The plate length is $L=U\tau_m$ and the rate of heat loss over the total area of the plate, $A_P=Ll$, is

$$Q_P=2A_P\frac{\lambda T_M}{\sqrt{\pi\kappa\tau_m}} \qquad [65]$$

This result holds for a plate where subduction occurs at the same age everywhere, such that the distribution of seafloor ages is a boxcar function (which shall be referred to as a 'rectangular' age distribution). Note that it was derived directly from eqn [64] independently of dynamic constraints on the spreading velocity. All the dynamic information needed is in the subduction age $\tau_m$, which has not been determined yet.

It may be shown that all the other key variables of convection, plate velocity $U$ and length $L$, depend on $\tau_m$. To obtain a closure equation for this variable, a widely used argument is that the thermal boundary layer becomes unstable when a local Rayleigh number exceeds a threshold value. This leads to the 'parameterized' model with $\beta=1/3$, which is not satisfactory. A key piece of physics is missing, which would specify how $\tau_m$ changes when the mantle cools down. When the Earth was hotter, lithospheric plates were stiffer than today (Korenaga, 2006), but consequences for the subduction age $\tau_m$ or the plate length $L$ are not obvious. One might imagine, for example, that the higher intrinsic stiffness of the lithosphere gets compensated by subducting younger and hence thinner plates, such that the total dissipation due to bending does not change much.

To specify the controls on the Earth's heat loss, one runs into two different types of difficulties. One must understand what determines the maximum plate age $\tau_m$ and one must go from a single convection cell to several cells with completely different characteristics. Even if we restrict ourselves to the major plates on Earth today, we cannot overlook the fact that both their size and spreading rate vary by one order of magnitude. In such conditions, the best strategy is to derive useful relationships without reference to dynamic arguments.

We use again the half-space cooling model that is sufficiently accurate for our purposes. The distribution of seafloor area can be expressed as a function of dimensionless age $\tau/\tau_m$:

$$\frac{\mathrm{d}A}{\mathrm{d}\tau}=C_A f\left(\frac{\tau}{\tau_m}\right) \qquad [66]$$

where $C_A$ is the plate accretion rate. By construction, dimensionless function $f$ goes from 1 for $\tau/\tau_m=0$ to 0 for $\tau/\tau_m=1$. Using the heat flux expression [30], the total oceanic heat loss is

$$Q_{oc}=A_o\frac{\lambda T_M}{\sqrt{\pi\kappa\tau_m}}\frac{\int_0^1\frac{f(u)}{\sqrt{u}}\mathrm{d}u}{\int_0^1 f(u)\mathrm{d}u}=A_o\frac{\lambda T_M}{\sqrt{\pi\kappa\tau_m}}\xi(f) \qquad [67]$$

where $A_o$ is the total ocean surface and $\xi(f)$ a coefficient that depends on the dimensionless age distribution. For the present-day triangular age distribution,

$$Q_{oc}=\frac{8A_o}{3}\frac{\lambda T_M}{\sqrt{\pi\kappa\tau_m}} \qquad [68]$$

This has the same form as the previous result for a rectangular plate (eqn [65]), with a different proportionality constant.

Even though we have not used any dynamic argument to derive the heat loss equation, we can relate changes of heat loss to changes of spreading rate. The total oceanic area is

$$A_o=C_A\tau_m\int_0^1 f(u)\mathrm{d}u \qquad [69]$$

If we assume that the oceanic area and the age distribution remain constant, changes of $C_A$, the rate of plate generation, imply changes of $\tau_m$, which in turn imply changes of heat loss at constant mantle temperature.

The oceanic heat loss can be equated with little error to the convective heat loss on Earth. Thus, eqns [65], [67], and [69] provide the most compact description of the physical controls on cooling. They avoid the problem of defining an 'average' plate with average velocity and length. They say nothing, however, about the maximum plate age $\tau_m$.

### 7.06.7.5 Vagaries of Seafloor Spreading and Heat Loss

We have taken great care in calculating the various items in the energy budget but have been dealing with a record of oceanic spreading and geologic activity that is very short compared to the planet's age. Thus, we must evaluate whether our estimates are truly representative of the Earth's secular evolution or not.

In eqn [67], one coefficient that can vary significantly over short timescales is $\xi(f)$, which depends on the dimensionless

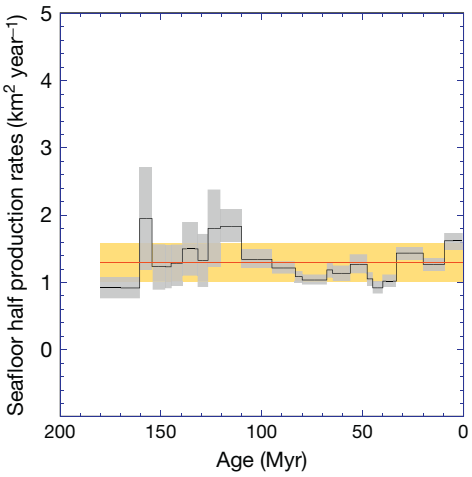


**Figure 18** Variation of seafloor spreading rates over the last 180 My accounting for oceanic ridges that got subducted in the Pacific and Tethys Oceans. The black line is the half spreading rate and the gray area represents the uncertainty. The red line is the average value. Adapted from Cogné J-P and Humler E (2004) Temporal variation of oceanic spreading and crustal production rates during the last 180 My. *Earth and Planetary Science Letters* 227: 427–439.

distribution of seafloor ages. A few authors have attempted to calculate spreading rates in the past. The last 180 My has seen the closure of the Tethys Ocean and the subduction of several ridges in the paleo-Pacific Ocean (Engebretson et al., 1984). Accounting for those, the total seafloor generation rate has not changed significantly for the past 180 My according to Cogné and Humler (2004) (**Figure 18**). Fluctuations in seafloor spreading may occur on a larger timescale. Subduction of young seafloor occurs mostly at the edge of continents and may be due to the complex shapes of ocean–continent boundaries. With all continents assembled in a single landmass, the large continuous oceanic domain imposes less constraints on spreading and subduction. In other words, the present-day distribution of subduction zones may be a transient feature associated with the breakup of Gondwanaland (Seton et al., 2009). Coltice et al. (2012) had recently reproduced the triangular oceanic age distribution with numerical calculations of convection in a spherical Earth with platelike behavior and rigid blocks acting as continents. They found that, when continents are assembled, ocean–ocean subduction dominates and generates the same rectangular age distribution as classical convection systems where subduction is entirely controlled by buoyancy.

The assembly and breakup of supercontinents may affect the distribution of seafloor ages in the oceans and hence the Earth's heat loss. Such global reorganization occurs over some characteristic time $\tau_W$. Allègre and Jaupart (1985) had related this time to the 'mean free path' of continents, such that continents sweep the whole surface of the Earth and necessarily run into one another. They obtained $\tau_W \approx 400$ My for present-day spreading rates and distribution of continents, which is less than the thermal adjustment time $\tau_p$ (eqn [62]). $\tau_W$ varies as a function of continental area and drift velocity and has probably been larger in the past when continents occupied a smaller fraction of the Earth's surface. Geologic data support such an increase of $\tau_W$ (Hoffman, 1997). Note that this observation runs against the intuitive notion that plates moved faster in the past. If the rate of heat loss of the Earth depends on the distribution of continents, it oscillates on a timescale $\tau_W$ over a long-term decreasing trend. We now attempt to estimate how large these oscillations can be.

Convective systems that are not constrained by lateral boundaries lead to age distributions that are almost rectangular (see **Appendix H**). In this case, subduction occurs at the same age everywhere and parameter $\xi(f)$ is equal to 2, as shown by eqn [65], which is 25% less than the value for the triangular distribution (8/3). This decreases the estimated oceanic heat loss by about 8 TW, which amounts to about half of the difference between present heat loss and heat production in the mantle (**Table 12**). Assuming for the sake of argument that the lifetime of a supercontinent is as long as the Wilson cycle and that these cycles are accompanied by changes of the age distribution of seafloor, the time-averaged oceanic heat loss could be 12.5% (i.e., 4 TW) less than the estimate of **Table 12**. A similar result was obtained by Grigné et al. (2005) using numerical models with many interacting convection cells of variable wavelength. As shown by Labrosse and Jaupart (2007), such fluctuations have a small influence on the Earth's thermal evolution because they are too small to cause significant changes of the planet's bulk internal energy and temperature. They do, however, impact arguments on the Urey ratio and the global energy budget.

Another variable that enters the heat loss expression (eqn [67]) is the total area of oceans. So far, we have assumed that it remains constant through time, but changes of oceanic area that are not related to rigid plate tectonics are likely to occur due to zones of diffuse deformation. Such zones are found in both oceans and continents and presently account for $\approx 15\%$ of the Earth's surface (Gordon, 2000). In continents, extension occurs at the expense of oceans, whereas shortening increases the oceanic area. These zones are usually very active and characterized by high heat flux, as in the Basin and Range Province, for example. Assuming that the average heat flux over such zones is equal to that in the Basin and Range Province (105 mW m$^{-2}$), the net effect on the global heat loss is small because this heat flux is $\approx$ the average oceanic one.

Yet another type of transient may be due to alternating phases of enhanced and subdued hot spot activity. The magnitude of the induced heat loss variations is likely to be small given the relatively modest contribution of mantle plumes to the total heat loss ($<4$ TW).

Three types of transient phenomena are likely to induce fluctuations of the Earth's rate of heat loss. Thus, one should allow for small, but significant, departures from today's energy budget in studies of the Earth's secular thermal evolution. These departures are not large enough to explain the difference between the present and the average values of the secular cooling rate, however, and we evaluate the role that may be played by the Earth's core.

### 7.06.7.6 Heat Flow from the Core

Collapsing the thermal evolution of the Earth into a single energy equation (eqn [53]) explicitly assumes that only one temperature is sufficient to describe internal energy changes or

equivalently that the core and the mantle evolve at proportional rates. There are reasons to think otherwise: as discussed in Section 7.06.5.3, the core has probably been cooling by more than 750 K, and possibly by as much as 1000 K, in 4 Gy, whereas the mantle has cooled by $<200$ K over the same interval. Let us consider how this affects the thermal evolution of the Earth.

Allowing for imperfect coupling between mantle and core, the global energy balance must allow for two different temperature evolutions:

$$M_m\langle C_m\rangle\frac{dT_m}{dt}+M_c\langle C_c\rangle\frac{dT_c}{dt}=-Q+H \qquad [70]$$

where, for simplicity, the effective heat capacities for the core and mantle, $\langle C_c\rangle$ and $\langle C_m\rangle$, respectively, account for isentropic temperature gradients and the consequences of inner core growth. $M_m$ and $M_c$ are the mantle and core masses, respectively. Taking average cooling rates of $50\,K\,Gy^{-1}$ and $250\,K\,Gy^{-1}$ for mantle and core, respectively, and $H=20$ TW, we find that the present-day heat loss is $Q=43$ TW, close to the observations. With the additional degree of freedom brought by core cooling, one can readily reconcile the present-day energy budget with available constraints on the mantle cooling rate and heat production. In other words, the difference between the present-day cooling rate of Earth ($98\,K\,Gy^{-1}$, Table 11) and the secular average value for the mantle ($50\,K\,Gy^{-1}$, Section 7.06.6) may be due in part to imperfect thermal coupling between mantle and core.

### 7.06.7.7 Summary

This section has emphasized that it is not easy to get around the powerful constraint of the energy budget. Most theoretical models for the cooling of Earth fail to account for the present-day imbalance between heat loss and heat production. This may be due in part to a particular convection phase that temporarily enhances heat loss compared to the long-term evolution. Past mantle temperature changes are documented in a variety of ways and provide key evidence on the Earth's convective engine. In particular, they imply that, in the past, the bulk rate of heat loss has changed less rapidly than that of heat production. The assumption that temperatures in the core and the mantle evolve at proportional rates is a gross simplification, which is difficult to reconcile with recent results on core thermal properties and geodynamo requirements.

## 7.06.8 Conclusions

Studies of the thermal evolution of the Earth are as old as physics and remain central to geology, for they deal with the energy that drives all geologic processes. The heat budget of the mantle can be established with a reasonable accuracy ($\approx$20%), thanks to the tremendous improvements in our knowledge of physical properties and data coverage. The Urey number is the ratio of heat production to heat loss, two imperfectly known quantities whose estimates are summarized in Table 12. Our current estimates for the Urey number are in the range 0.12–0.49, which rules out most available cooling models. Heat loss does not follow the decay of radiogenic heat production, and the time lag is on the order of the age of the Earth (see Section 7.06.7.1).

The present mantle energy budget implies a secular cooling rate in the range of 7–210 K $Gy^{-1}$. Over a long timescale, the average value for the cooling rate estimated from geologic constraints appears to be at the low end of this range (50 K $Gy^{-1}$). There is no reason to assume that the cooling rate has remained constant through time. Both geologic data and physical constraints on the thermal structure of the early Earth indicate that the cooling rate has increased as the planet got older (see Section 7.06.7.5). Plate tectonics is a regime of mantle convection attainable only in a state of subsolidus rheology that is with at most 40% melt. Thus, independent constraints on the cooling rate come from considerations of early Earth conditions. The most recent phase diagrams for the mantle indicate that the 40% melt threshold is reached when the potential temperature is about 200 K higher than at present (Litasov and Ohtani, 2002; Zerr et al., 1998; see also Boehler, vol. 2). If plate tectonics has been operating since the end of the magma ocean, the total amount of cooling is known and the average cooling rate cannot be more than about 50 K $Gy^{-1}$.

## Appendix A Contraction of the Earth due to Secular Cooling

The planet contracts as it cools down. This induces changes of gravity that themselves induce changes of pressure and density. Here, we derive an approximate solution for a homogeneous planet in order to show how this affects the contraction rate and to identify the control variables.

Assuming spherical symmetry, governing equations are as follows:

$$\frac{1}{r^2}\frac{d}{dr}(r^2g)=4\pi G\rho \qquad [A.1]$$

$$\frac{dP}{dr}=-\rho g \qquad [A.2]$$

where $G$ is the gravitational constant and $P$ the pressure. From the equation of state, we deduce that

$$\frac{d\rho}{dr}=\frac{d\rho}{dP}\frac{dP}{dr}=\frac{\rho}{K_s}\frac{dP}{dr} \qquad [A.3]$$

$$=-\frac{\rho^2 g}{K_s} \qquad [A.4]$$

where $K_s$ is the isentropic bulk modulus. For simplicity, the bulk modulus is assumed to be constant. Using radius $R$ as length scale and the density at the top (defined more precisely later) $\rho_T$ as density scale, the proper gravity scale is

$$[g]=G\rho_T R \qquad [A.5]$$

Equations can now be written using dimensionless variables:

$$\frac{1}{r^2}\frac{d}{dr}(r^2g)=4\pi\rho \qquad [A.6]$$

$$\frac{d\rho}{dr}=-\epsilon\rho^2 g \qquad [A.7]$$

where $\varepsilon$ is a dimensionless number that provides a measure of the magnitude of density changes due to pressure:

$$\varepsilon = \frac{\rho_T [g] R}{K_s} = \frac{G\rho_T^2 R^2}{K_s} \quad [A.8]$$

We consider that the radial temperature profile is isentropic and neglect the upper thermal boundary layer that does not contribute much to the total mass and energy. Thus, reference density $\rho_T$ is the mantle density at the atmospheric pressure, that is, at the potential temperature of the isentropic radial profile. For what follows, the key point is that $\rho_T$ is not affected by internal pressure changes due to contraction.

For $\rho_T = 3.3 \times 10^3\,\mathrm{kg\,m^{-3}}$, $R = 6370$ km, and a value of 150 GPa for $K_s$, $\varepsilon \approx 0.2$. This is small and we expand all the variables in series of $\varepsilon$. We find

$$\rho = 1 + \varepsilon\left[-\frac{4\pi}{6}\left(r^2 - 1\right)\right] + \cdots \quad [A.9]$$

$$g = \frac{4\pi}{3} r + \varepsilon\left[\frac{16\pi^2}{90} r\left(5 - 3r^2\right)\right] + \cdots \quad [A.10]$$

To first order in $\varepsilon$, the mass of the planet is

$$M = \frac{4}{3}\pi\rho_T R^3\left(1 + \frac{4\pi}{15}\varepsilon\right) = \frac{4}{3}\pi\rho_T R^3\left(1 + \frac{4\pi}{15}\frac{G\rho_T^2 R^2}{K_s}\right) \quad [A.11]$$

Writing that mass is conserved when $\rho_T$ and $R$ change, we obtain

$$\frac{\Delta R}{R} = -\frac{1}{3}\frac{\Delta\rho_T}{\rho_T}\left(1 + \frac{16\pi}{45}\frac{G\rho_T^2 R^2}{K_s}\right) \quad [A.12]$$

By definition, surface density $\rho_T$ is calculated at the atmospheric pressure and hence depends on temperature only, such that

$$\frac{\Delta\rho_T}{\rho_T} = -\alpha\Delta T \quad [A.13]$$

where $\alpha$ is the thermal expansion coefficient at the atmospheric pressure. The end result is therefore

$$\frac{\Delta R}{R} = \frac{\alpha\Delta T}{3}\left(1 + \frac{16\pi}{45}\frac{G\rho_T^2 R^2}{K_s}\right) \quad [A.14]$$

This shows that contraction is enhanced by the change in gravity field.

## Appendix B Gravitational Energy Changes

Here, we present a demonstration for changes of the bulk gravitational energy that was made by Paul Roberts (pers. comm.). For a sphere of uniform density and radius $R$,

$$E_g = -\frac{16\pi^2}{15} G\rho^2 R^5 \quad [B.1]$$

For a contracting object with moving material boundaries, it is convenient to employ the Lagrangian variables. Because of mass conservation, the most convenient variable is the mass in a sphere of radius $r$:

$$M(r) = 4\pi\int_0^r \rho(r) r^2 \mathrm{d}r = \int_0^r \rho(r)\mathrm{d}V \quad [B.2]$$

Thus,

$$g(r) = \frac{GM(r)}{r^2} \quad [B.3]$$

The gravitational energy in a material volume bounded by spheres of radii $r_1$ and $r_2$ is

$$E_{12} = -\int_{r_1}^{r_2} \rho g r \mathrm{d}V = -\int_{M_1}^{M_2} r g \mathrm{d}M = -\int_{M_1}^{M_2} \frac{GM}{r}\mathrm{d}M \quad [B.4]$$

The Lagrangian derivative is easily calculated using the variable $M$:

$$\frac{\mathrm{d}E_{12}}{\mathrm{d}t} = \int_{M_1}^{M_2} \frac{\mathrm{d}r}{\mathrm{d}t}\frac{GM}{r^2}\mathrm{d}M \quad [B.5]$$

For this calculation, the velocity field is limited to contraction, such that $\mathrm{d}r/\mathrm{d}t = v_c$. Thus,

$$\frac{\mathrm{d}E_{12}}{\mathrm{d}t} = \int_{M_1}^{M_2} v_c \frac{GM}{r^2}\mathrm{d}M = -\int_{r_1}^{r_2} \rho(\mathbf{v}_c \cdot \mathbf{g})\mathrm{d}V \quad [B.6]$$

which is the integral form of eqn [17] in the main text.

## Appendix C Viscous Dissipation

The developments that follow stem in part from comments by Yanick Ricard. Viscous dissipation involves deviatoric stresses and departures from hydrostatic equilibrium. For steady-state conditions, Alboussière and Ricard (2013) had thoroughly examined the various assumptions and simplifications that have been made over the years and had come up with several alternative forms of the dissipation equation. In transient thermal conditions, the problem becomes more complicated as one must deal with changes of the hydrostatic base state. The base state is defined by the azimuthal averages of temperature and pressure and follows an isentrope, defined by its entropy $\bar{s}$, temperature $\overline{T}$, pressure $\overline{p}$, and density $\overline{\rho}$. By definition of the isentrope, $\bar{s}$ does not vary with radial distance, such that

$$\rho T\frac{\partial\bar{s}}{\partial r} = \rho C_p\frac{\partial\overline{T}}{\partial r} - \alpha\overline{T}\frac{\partial\overline{p}}{\partial r} = 0 \quad [C.1]$$

From hydrostatics,

$$\frac{\partial\overline{p}}{\partial r} = -\overline{\rho}g \quad [C.2]$$

which leads to

$$\frac{\partial\overline{T}}{\partial r} = -\frac{\alpha g}{C_p}\overline{T} \quad [C.3]$$

which defines the isentropic radial temperature profile. $\bar{s}$ is a function of time only and is well suited to track changes of the base state as the planet is cooling down.

For convection in the solid Earth, inertial terms can be neglected in the momentum balance, with the consequence that changes of kinetic energy are also negligible in the mechanical energy balance equation [10]. Subtracting the hydrostatic balance equation [14] from the momentum balance, we get

$$0 = -\nabla(\delta p) - \nabla\cdot\boldsymbol{\sigma} + \delta\rho\mathbf{g} \quad [C.4]$$

where $\delta\rho$ and $\delta\rho$ are deviations from the azimuthal averages of pressure and density, respectively, and where we have neglected perturbations to the gravity field, which only appear in second-order terms. Introducing the temperature

perturbation, $\theta$, the density perturbation is obtained by a Taylor expansion about the mean:

$$\frac{\delta\rho}{\overline{\rho}}=\frac{\delta p}{K_T}-\alpha\theta \qquad [C.5]$$

Introducing the isentropic bulk modulus $K_S$ and Grüneisen parameter $\gamma$, such that $K_S=K_T(1+\gamma\alpha T)$, we obtain

$$0=-\nabla(\delta p)+\overline{\rho}\mathbf{g}\left[\frac{\delta p}{K_S}+\frac{\gamma\alpha T}{K_S}\delta p-\alpha\theta\right]-\nabla\cdot\boldsymbol{\sigma} \qquad [C.6]$$

which can be recast as

$$0=-\overline{\rho}\nabla\left(\frac{\delta p}{\overline{\rho}}\right)+\overline{\rho}\mathbf{g}\left[\frac{\gamma\alpha T}{K_S}\delta p-\alpha\theta\right]-\nabla\cdot\boldsymbol{\sigma} \qquad [C.7]$$

Using the entropy equation, we obtain

$$0=-\overline{\rho}\nabla\left(\frac{\delta p}{\overline{\rho}}\right)-\frac{\alpha\overline{\rho}T\mathbf{g}}{C_p}\delta s-\nabla\cdot\boldsymbol{\sigma} \qquad [C.8]$$

where $\delta s$ is the entropy perturbation. Taking the scalar product with convective velocity $\mathbf{w}$, we deduce a modified form of the mechanical energy balance:

$$0=-\overline{\rho}\mathbf{w}\cdot\nabla\left(\frac{\delta p}{\overline{\rho}}\right)-\frac{\alpha\overline{\rho}T}{C_p}(\mathbf{w}\cdot\mathbf{g})\delta s-\mathbf{w}\cdot\nabla\cdot\boldsymbol{\sigma} \qquad [C.9]$$

Integrating this equation over the planet volume yields three separate integrals, which are evaluated separately. The first one on the right yields

$$\int_V\overline{\rho}\mathbf{w}\cdot\nabla\left(\frac{\delta p}{\overline{\rho}}\right)\mathrm{d}V=\int_A\delta p\,\mathbf{w}\cdot\mathrm{d}A-\int_V\frac{\delta p}{\overline{\rho}}\nabla\cdot(\overline{\rho}\mathbf{w})\mathrm{d}V \qquad [C.10]$$

The two contributions on the right-hand side are zero. For the first one, we use the fact that the pressure perturbation $\delta p$ must vanish at the Earth's surface where pressure is held constant. For the second one, we rely on the continuity equation in the anelastic approximation, $\nabla\cdot(\overline{\rho}\mathbf{w})=0$ (Braginsky and Roberts, 1995). The third integral on the right of the mechanical energy balance equation [C.9] yields

$$\begin{aligned}\int_V\mathbf{w}\cdot\nabla\cdot\boldsymbol{\sigma}\mathrm{d}V&=\int_V(\mathbf{w}\cdot\nabla\cdot\boldsymbol{\sigma}-\nabla\cdot[\boldsymbol{\sigma}\cdot\mathbf{w}])\mathrm{d}V+\int_V\nabla\cdot[\boldsymbol{\sigma}\cdot\mathbf{w}]\mathrm{d}V\\&=\int_V\phi\mathrm{d}V+\int_A\mathbf{w}\cdot[\boldsymbol{\sigma}\cdot\mathrm{d}A]\end{aligned} \qquad [C.11]$$

The last term on the right of this equation is the work of shear stresses at the Earth's surface, which is negligible. Using these results, the mechanical energy equation may be reduced to

$$\int_V\overline{\phi}\mathrm{d}V=-\int_V\frac{\alpha\overline{\rho}T}{C_p}(\mathbf{w}\cdot\mathbf{g})\delta s\mathrm{d}V \qquad [C.12]$$

which specifies dissipation. Under a series of assumptions, it may be shown that the integral on the right can be reduced to (Alboussière and Ricard, 2013)

$$\int_V\frac{\alpha\overline{\rho}T}{C_p}(\mathbf{w}\cdot\mathbf{g})\delta s\mathrm{d}V=-\int_V\rho\alpha g\overline{w_r\theta}\mathrm{d}V \qquad [C.13]$$

where $w_r$ is the radial velocity component. This integral can be interpreted as the work of buoyancy forces and has been called the 'buoyancy flux.' The power of the dissipation equation in this form is that it can be expressed as a function of the convective heat flux $\left(\rho C_p\overline{w_r\theta}\right)$ and can be related to heat loss directly. Alboussière and Ricard (2013) had emphasized its approximate nature, however, such that it cannot be applied to complex thermodynamic systems without care.

Dissipation enters the local energy balance (eqn [11]) but not the global energy budget for the planet as a whole (eqn [1]). To find out how this comes about, we separate entropy into the azimuthal average $\bar{s}$ and perturbation $\delta s$:

$$\overline{\rho}T\frac{\mathrm{D}s}{\mathrm{D}t}=\overline{\rho}T\frac{\mathrm{D}\bar{s}}{Dt}+\overline{\rho}T\frac{\partial\delta s}{\partial t}+\overline{\rho}T\mathbf{w}\cdot\nabla\delta s \qquad [C.14]$$

where we have relied on the anelastic approximation in using $\overline{\rho}$ instead of $\rho$ (Braginsky and Roberts, 1995). The last term on the right can be rewritten as follows:

$$\overline{\rho}T\mathbf{w}\cdot\nabla\delta s=\nabla\cdot(\overline{\rho}T\delta s\mathbf{w})-\overline{\rho}(\mathbf{w}\cdot\nabla T)\delta s-T\delta s\nabla\cdot(\overline{\rho}\mathbf{w}) \qquad [C.15]$$

The third term on the right can be set to zero using mass conservation, as mentioned earlier. The first term on the right is written in conservative form and leads to zero upon integration over the volume. Thus,

$$\int_V\overline{\rho}T(\mathbf{w}\cdot\nabla\delta s)\mathrm{d}V=-\int_V\overline{\rho}(\mathbf{w}\cdot\nabla T)\delta s\mathrm{d}V \qquad [C.16]$$

Collecting terms in the energy balance and neglecting external energy transfers (in the $\psi$ term), we find

$$\begin{aligned}\int_V\overline{\rho}T\frac{\mathrm{D}\bar{s}}{\mathrm{D}t}\mathrm{d}V+\int_V\overline{\rho}T\frac{\partial\delta s}{\partial t}\mathrm{d}V&=\int_V\overline{\rho}\mathbf{w}\cdot\left(\nabla T-\frac{\alpha T}{C_p}\mathbf{g}\right)\delta s\mathrm{d}V\\&\quad-\int_A\mathbf{q}\cdot\mathrm{d}A+\int_VH\mathrm{d}V\end{aligned} \qquad [C.17]$$

If we neglect second-order terms, the first term on the right involves temperature variations along the isentrope and cancels because of our assumption of an isentropic base state defined by eqn [C.3]. We now evaluate the second term on the left. Integrating over the volume involves surface integrals:

$$\int_V\overline{\rho}T\frac{\partial\delta s}{\partial t}\mathrm{d}V=\int_0^R\left(\int_A\overline{\rho}T\frac{\partial\delta s}{\partial t}\mathrm{d}A\right)\mathrm{d}r \qquad [C.18]$$

We split temperature into the azimuthal average $\overline{T}$ and perturbation $\theta$ and consider the two corresponding contributions. For the former, by definition of the azimuthal average, the surface integral over a spherical shell of radius $r$ can be expressed as follows:

$$\int_A\overline{\rho}\overline{T}\frac{\partial\delta\bar{s}}{\partial t}\mathrm{d}A=\left(\overline{\rho}\overline{T}\frac{\partial\delta\bar{s}}{\partial t}\right)4\pi r^2 \qquad [C.19]$$

which is zero by definition of the entropy perturbation $\delta s$. The remaining term involving the temperature perturbation $\theta$ and the entropy perturbation $\delta s$ is a second-order term that can be neglected as before.

The first term on the left of eqn [C.17] involves the entropy of the base state:

$$\overline{\rho}T\frac{\overline{\mathrm{D}s}}{\mathrm{D}t}=\overline{\rho}T\left(\frac{\partial\bar{s}}{\partial t}+\mathbf{w}\cdot\nabla\bar{s}\right)=\overline{\rho}T\left(\frac{\partial\bar{s}}{\partial t}\right) \qquad [C.20]$$

where we have used $\nabla\bar{s}=0$ by definition of the isentrope. Writing entropy variations with state variables $T$ and $\rho$, we get

$$\overline{\rho}T\frac{\partial \overline{s}}{\partial t}=\overline{\rho}C_v\frac{\partial \overline{T}}{\partial t}-\frac{\alpha T K_T}{\rho}\frac{\partial \rho}{\partial t} \quad [C.21]$$

We therefore end up with an equation for temperature:

$$\int_V \overline{\rho}C_v\frac{\partial \overline{T}}{\partial t}dV=\int_V \frac{\alpha T K_T}{\rho}\frac{\partial \rho}{\partial t}dV-\int_A \mathbf{q}\cdot d\mathbf{A}+\int_V H dV \quad [C.22]$$

where the first term on the right is the only remaining contribution of contraction and has been referred to as 'adiabatic heating.' This term is small for solid-state planets because of their small values of the thermal expansion coefficient ($\alpha T \ll 1$). If one uses an alternative form of the entropy equation with pressure and temperature as the two independent state variables, one deals with $C_p$ instead of $C_v$. The former varies with temperature but the latter does not (at least in the Dulong–Petit–Debye limit). Using the thermodynamic identity $C_p = C_v(1+\gamma\alpha T)$, one can see that it is not self-consistent to deal with adiabatic heating and ignore variations of $C_p$ at the same time (Alboussière and Ricard, 2013). From a purely practical point of view, however, as long as one does not introduce such simplifications into formal thermodynamic arguments, there is no harm in keeping negligible terms in an equation.

## Appendix D Half-Space Cooling Model with Temperature-Dependent Properties

The general form of the one-dimensional heat equation is

$$\rho C_p\frac{\partial T}{\partial \tau}=\frac{\partial}{\partial z}\left(\lambda\frac{\partial T}{\partial z}\right) \quad [D.1]$$

where all properties depend on temperature $T$. In this section, the temperature for the half-space is initially $T_M$ and temperature is set to zero at the surface: $T(z=0,\tau)=0$.

For constant physical properties, the temperature for the half-space is given by (Carslaw and Jaeger, 1959)

$$T(z,t)=T_M \mathrm{erf}\left(\frac{z}{2\sqrt{\kappa\tau}}\right) \quad [D.2]$$

and the surface heat flux is

$$q(0,t)=\frac{\lambda T_M}{\sqrt{\pi\kappa\tau}} \quad [D.3]$$

For temperature-dependent properties, Carslaw and Jaeger (1959) introduced the following variable:

$$\theta=\frac{1}{\lambda_0}\int_0^T \lambda dT \quad [D.4]$$

where $\lambda_0$ is thermal conductivity at the reference temperature $T=0$; the heat equation becomes:

$$\frac{1}{\kappa}\frac{\partial \theta}{\partial \tau}=\frac{\partial^2 \theta}{\partial z^2} \quad [D.5]$$

where $\kappa$ is the temperature-dependent thermal diffusivity. For the boundary and initial conditions of interest here, this equation can be written in terms of a similarity variable $\eta$:

$$\theta(z,t)=\Theta(\eta), \text{ with } \eta=z\tau^{-1/2} \quad [D.6]$$

$$-\frac{\eta}{2\kappa}\Theta'=\Theta'' \quad [D.7]$$

with the following boundary conditions:

$$\Theta(0)=0, \Theta(\infty)=\Theta_M, \Theta'(\infty)=\Theta''(\infty)=0 \quad [D.8]$$

The surface heat flux is thus

$$q=\lambda\frac{\partial T}{\partial z}_{z=0}=k_0\tau^{-1/2}\Theta'(0) \quad [D.9]$$

which is of the form $C_Q\tau^{-1/2}$ regardless of the specific functional form of $\rho$, $C_p$, and $\lambda$. This beautiful result was pointed out first by Lister (1977).

## Appendix E Plate Models for the Oceanic Lithosphere

For a plate of thickness $a$ initially at temperature $T_M$, with $T(z=0,\tau)=0$ and $T(z=a,\tau)=T_M$, the temperature for $0<z<a$ is given by

$$T(z,\tau)=T_M\left(\frac{z}{a}+\sum_{n=1}^{\infty}\frac{2}{n\pi}\sin\left(\frac{n\pi z}{a}\right)\exp\left(\frac{-n^2\pi^2\kappa\tau}{a^2}\right)\right) \quad [E.1]$$

and the surface heat flux is given by

$$q(0,t)=\frac{\lambda T_M}{a}\left(1+2\sum_{n=1}^{\infty}\exp\left(\frac{-n^2\pi^2\kappa\tau}{a^2}\right)\right) \quad [E.2]$$

which diverges at $\tau=0$. For $\tau \ll a^2/\kappa$, the heat flux

$$q(0,\tau)\approx\frac{\lambda T_M}{\sqrt{\pi\kappa\tau}} \quad [E.3]$$

With fixed heat flux at the base, $Q(a,\tau)=\lambda T_M/a$, the temperature of the plate is given by

$$T(z,\tau)=\frac{T_M z}{a}-\frac{4T_M}{\pi}\sum_{n=0}^{\infty}\frac{(-1)^n}{(2n+1)}\cos\left(\frac{(2n+1)\pi(z-a)}{2a}\right)\times\exp\left(\frac{-(2n+1)^2\pi^2\kappa\tau}{4a^2}\right)+\frac{8T_M}{\pi^2}\sum_{n=0}^{\infty}\frac{(-1)^n}{(2n+1)^2}\sin\left(\frac{(2n+1)\pi z}{2a}\right)\exp\left(\frac{-(2n+1)^2\pi^2\kappa\tau}{4a^2}\right) \quad [E.4]$$

and the surface heat flux is given by

$$\frac{q(0,t)}{\frac{\lambda T_M}{a}}=1+2\sum_{n=0}^{\infty}\exp\left(\frac{-(2n+1)^2\pi^2\kappa\tau}{4a^2}\right)+\frac{4}{\pi}\sum_{n=0}^{\infty}\frac{(-)^n}{(2n+1)}\exp\left(\frac{-(2n+1)^2\pi^2\kappa\tau}{4a^2}\right) \quad [E.5]$$

The surface heat flux for these three different boundary conditions is compared in Figure 19, with the same length scale $L=a$ for the half-space and the constant temperature boundary condition and $L=2a$ for the heat flux boundary condition.

## Appendix F Differences Between Estimates of the Energy Budget

Table 14 compares our construction of the mantle energy budget with those proposed by Stacey and Davis (2008) and

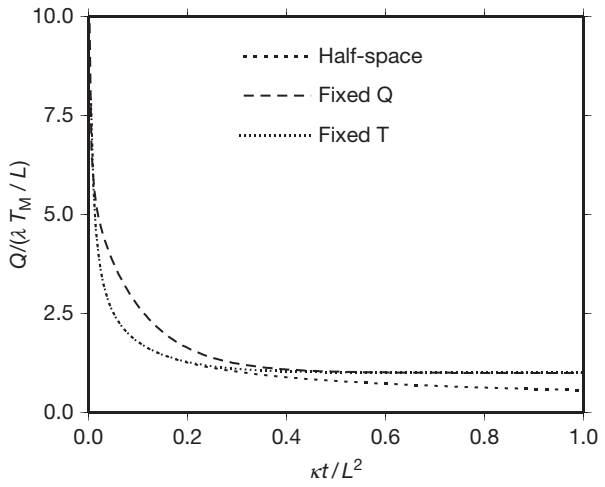


**Figure 19** Normalized heat flux as a function of reduced time for different cooling models for the oceanic lithosphere. Length scale $L$ is equal to $a$, the plate thickness, in the fixed temperature model and to 2a in the fixed flux model. In the half-space model, $L$ cancels out. See **Appendix E**.

**Table 14** Various estimates of the global budget

| | *Stacey and Davis (2008)* | *Davies (1999)* | *This study* |
|---|---|---|---|
| Total heat loss | 44 | 41 | 46 |
| Continental heat production | 8 | 5 | 8 |
| Upper mantle | | 1.3 | |
| Lower mantle | | 11–27 | |
| Mantle heat production | 20 | 12–28[a] | 11 |
| Latent heat–core differentiation | 1.2 | <1 | |
| Mantle differentiation | 0.6 | 0.3 | 0.2 |
| Gravitational (thermal contraction) | 3.1 | | |
| Tidal dissipation | | 0.1 | 0.1 |
| Core heat loss | 3.5 | 5 | 11 |
| Mantle cooling | 8 | 9[b] | 16 |
| Present Urey ratio | 0.64 | 0.3–0.68 | 0.12–0.49 |

[a]Lower mantle heat production is variable and calculated to fit the mantle cooling rate.
[b]Mantle cooling is fixed.

Davies (1999). Although the total energy budget is almost identical, there are major differences in the breakdown of the budget between different items. These differences originate in the various assumptions made as well as in the objectives that are sought. Our estimate uses a slightly different total oceanic area that reflects our better knowledge of continental margins. It also includes the contribution of hot spots, which is not accounted for by bulk lithosphere cooling. Finally, it allows for a small amount of radioelements in the subcontinental lithospheric mantle and takes advantage of our improved constraints on crustal heat production.

For Stacey and Davis (2008), the total heat production (28 TW) is significantly higher than the value of 20 TW for BSE and almost equal to that of the nondepleted chondritic model of Birch (1965). It seems that these authors have added the crustal heat production to BSE. The core heat loss is low because it is assumed identical to the heat carried by hot spots. Stacey and Davis (2008) also assumed that all the gravitational energy released by thermal contraction (3.1 TW) goes to heat.

In Davies (1999), the secular cooling of the mantle is assumed to be fixed by petrologic data and the lower mantle heat production is the variable that is adjusted to balance the budget when all the other variables are fixed. Core cooling is also assumed identical to the total heat flux from hot spots. Upper mantle heat production is known to be low (from samples of the mantle carried to the surface). Lower mantle is assumed to be a mixture between a depleted chondritic composition, which would give 11 TW, and a MORB (!?) like component, which would yield 27 TW. The ratio of those two components is adjusted to balance the budget. (Note that depleted mantle should give only 6 TW and the MORB-like component seems to have the same heat production as that of chondrites.)

The global energy budget of the Earth was one of the arguments used by Kellogg et al. (1999) to propose that the lowermost mantle forms a distinct reservoir with chondritic concentration in radioelements, the 'abyssal layer.' The heat production in the depleted MORB mantle (i.e., the source of depleted MORBs) is $\approx 0.6\,\mathrm{pW\,kg^{-1}}$. Assuming that this is representative of the whole mantle, the total mantle heat production would only be 2.5 TW, that is, much less than the $\approx 13$ TW obtained by removing the crustal heat production from BSE. (Note that Kellogg et al. (1999) used 31 TW for the total heat production in a 'chondritic' Earth.)

## Appendix G Average Thermal Structure and Temperature Changes in Upwellings and Downwellings

The reference vertical temperature profile is often called 'adiabatic,' which is misleading. Here, we recapitulate the definitions and introduce two different reference temperature profiles. The equation for the entropy per unit mass, $s$, is

$$\rho T \frac{\mathrm{D}s}{\mathrm{D}t} = \rho C_\mathrm{p} \frac{\mathrm{D}T}{\mathrm{D}t} - \alpha T \frac{\mathrm{D}p}{\mathrm{D}t} \qquad [\mathrm{G}.1]$$

$$= -\nabla \cdot \mathbf{q} + \phi + H \qquad [\mathrm{G}.2]$$

Note that this shows that entropy is not conserved due to irreversible dissipation and radioactive decay. Density changes due to temperature have a small impact on pressure and dynamic pressure variations are small compared to the hydrostatic pressure. Thus,

$$\frac{\mathrm{D}p}{\mathrm{D}t} \approx -\rho g w \qquad [\mathrm{G}.3]$$

where $w$ is the radial velocity component.

From these equations, we may deduce the isentropic temperature profile, such that $\mathrm{D}s/\mathrm{D}t = 0$. In the interior of the convecting system, far from the upper and lower boundaries, the dominant velocity component is the vertical. Assuming steady state and using eqn [G.1],

$$\rho C_\mathrm{p} w \frac{\mathrm{d}T_\mathrm{S}}{\mathrm{d}r} = -\alpha T_\mathrm{S} \rho g w \qquad [\mathrm{G}.4]$$

where $T_\mathrm{S}$ stands for the isentropic temperature profile. Thus,

$$\frac{dT_S}{dr} = -\frac{\alpha g}{C_p} T_S \qquad [G.5]$$

This is close to the vertical profile of the azimuthally averaged temperature in a steady-state well-mixed convective system with no internal heat production and negligible viscous dissipation.

The isentropic temperature gradient derived earlier provides a convenient *reference* profile that illustrates the role of compressibility. However, it is a poor approximation for the temperature path followed by a rising (or sinking) mantle parcel. We may consider for simplicity that such a parcel does not exchange heat with its surroundings, which is a good approximation for the broad return flow away from subduction zones. In this case, we set $\mathbf{q} = 0$, use the same approximation as before for pressure, and obtain

$$\rho C_p \frac{DT}{Dt} \approx \rho C_p \left( \frac{\partial T}{\partial t} + w \frac{\partial T}{\partial r} \right) = -(\alpha T) \rho g w + H + \phi \qquad [G.6]$$

The material parcel's temperature changes due to radiogenic heat production and dissipation and due to the work of pressure forces. This may be recast as follows:

$$\frac{\partial T}{\partial r} = -\frac{\alpha g}{C_p} T + \frac{1}{w} \left( \frac{\phi + H}{\rho C_p} - \frac{\partial T}{\partial t} \right) \qquad [G.7]$$

where one should note that secular cooling acts in the same direction as internal heat production. The radial temperature gradient from eqn [G.7] differs from the isentropic value by about 30%. Here, we see the importance of knowing precisely the secular cooling rate $\partial T/\partial t$.

## Appendix H Seafloor Age Distribution as Seen from Models of Mantle Convection

We present here a few examples of temperature fields obtained in numerical models of convection and compute the seafloor age distribution they would provide for comparison with that

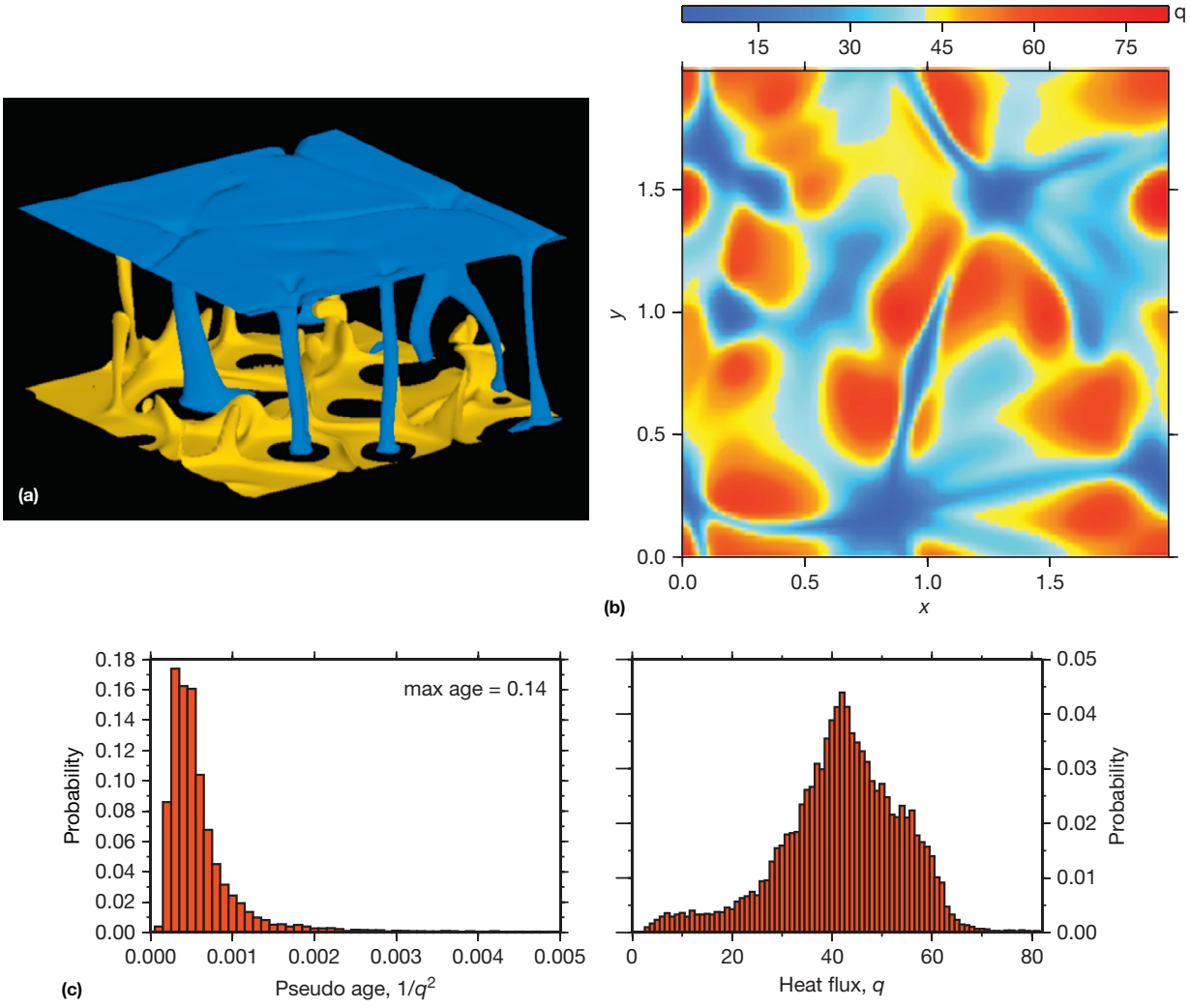


**Figure 20** Snapshot of temperature (a), surface heat flux (b), and the corresponding pseudo-age distribution (c) in a convection system with a Rayleigh number $Ra = 10^7$ and an internal heating rate $H = 20$. Note that the age distribution is far from that of the Earth's oceans, which is triangular. From the model of Labrosse (2002). See **Appendix H** for details.

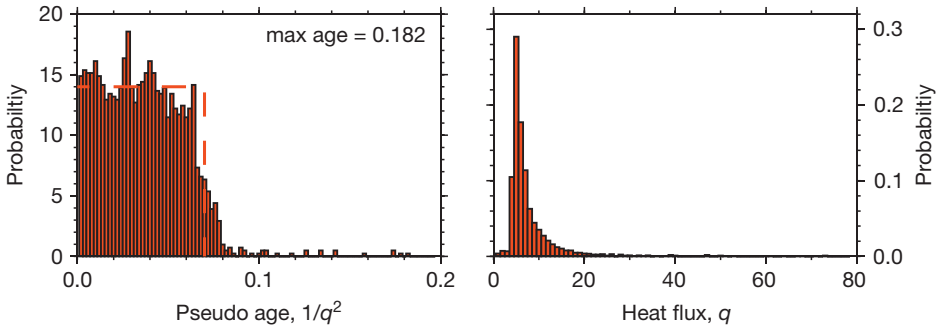


**Figure 21** Distribution of surface heat flux ($q$, right) and pseudo age ($1/q^2$) for a model with platelike behavior, corresponding to **Figure 3**. The age distribution is close to a rectangular one (dashed line). See **Appendix H** for details. From the model of Grigne et al. (2005).

of Earth today. In all cases presented, convection is set by imposing a destabilizing temperature difference $\Delta T$ between top and bottom and a uniform internal heating rate per unit volume $H$. This defines two dimensionless parameters (e.g., Sotin and Labrosse, 1999), the Rayleigh number $Ra$ and the dimensionless internal heating rate $H^*$:

$$Ra = \frac{g\alpha\Delta T D^3}{\kappa v_0}; \quad H^* = \frac{HD^2}{k\Delta T} \qquad [H.1]$$

where $D$ is the thickness of the system and $v_0$ is the dynamic viscosity at some reference point. The other symbols are the same as in the rest of the chapter. A third dimensionless number is the Prandtl number $Pr = v_0/\kappa$, which is of order $10^{23}$ in the mantle and is accordingly set to infinity. The viscosity of mantle material is known to vary with temperature, pressure, mineral phase, etc. To reproduce the plate tectonics regime of mantle convection, a complex rheological law must be used (see **Chapters 7.01** and **7.03**). This introduces yet another set of parameters. For example, the pseudoplastic rheology used by Tackley (2000) is defined by an effective viscosity

$$\eta_{\text{eff}} = \min\left[\eta(T), \frac{\sigma_y}{2\dot{\varepsilon}}\right] \qquad [H.2]$$

where $\sigma_y$ is a yield stress and $\dot{\varepsilon} = \sqrt{\dot{\varepsilon}_{i,j}\dot{\varepsilon}_{i,j}}/2$ the second invariant of the strain rate tensor. Viscosity is temperature-dependent:

$$\eta(T) = \exp\left[\frac{23.03}{T+1} - \frac{23.03}{2}\right] \qquad [H.3]$$

This specific rheological law was used to obtain the results of **Figure 3** (Grigné et al., 2005).

In numerical models of mantle convection, determining the age of each point at the surface requires extensive calculations with markers. To alleviate this difficulty, we use the fact that the surface heat flux is due to conductive cooling and define a pseudo age as follows:

$$q \propto \frac{1}{\sqrt{\tau}} \qquad [H.4]$$

We thus use heat flux values to determine the age distribution.

The first configuration tested is that of isoviscous Rayleigh–Bénard convection with internal heating. Using a snapshot from Labrosse (2002), we get a distribution of pseudo ages that is peaked at low values and exhibits a roughly exponential tail at large ages (**Figure 20**). This reflects that, with a large amount of internal heating, convective flow is dominated by strong cold plumes and passive return flow in most of the interior. There are weak hot plumes in the lower part of the domain, but they do not contribute much to the heat flux, in a manner reminiscent of that on Earth. The distribution of surface heat flux is due to the distributed return flow.

A somewhat more realistic model relying on the pseudoplastic rheology has been developed by Grigné et al. (2005) and a snapshot is shown in **Figure 3**. The distribution of surface heat flux and pseudo age for this model is given in **Figure 21**. The platelike behavior is such that the distribution of heat flux is peaked at low values and the pseudo-age distribution is approximately rectangular, reflecting the fact that all plates have similar sizes and velocity.

## Acknowledgments

Denis Andrault, David Bercovici, Jean-Pascal Cogné, Earl Davis, Steve Dye, Mark Jellinek, Jun Korenaga, Charlie Langmuir, Paul Roberts, and Gerald Schubert provided us with much information and many ideas. A thorough review by Yanick Ricard clarified important thermodynamic aspects.

## References

Abbott D, Burgess L, Longhi J, and Smith WHF (1994) An empirical thermal history of the Earth's upper mantle. *Journal of Geophysical Research* 99: 13835.

Abe Y (1993) Physical state of the very early Earth. *Lithos* 30: 223–235.

Abe Y (1997) Thermal and chemical evolution of the terrestrial magma ocean. *Physics of the Earth and Planetary Interiors* 100: 27–39.

Alboussière T and Ricard Y (2013) Reflections on dissipation associated with thermal convection. *Journal of Fluid Mechanics* 751: R1.

Alfé D, Gillan MJ, and Price GD (2002) Ab initio chemical potentials of solid and liquid solutions and the chemistry of the earth's core. *Journal of Chemical Physics* 116: 7127–7136.

Allègre CJ and Jaupart C (1985) Continental tectonics and continental kinetics. *Earth and Planetary Science Letters* 74: 171–186.

Andrault D, Bolfan-Casanova N, Nigro GL, Bouhifd MA, Garbarino G, and Mezouar M (2011) Solidus and liquidus profiles of chondritic mantle: Implication for melting of the Earth across its history. *Earth and Planetary Science Letters* 304: 251–259.

Andrault D, Muñoz M, Bolfan-Casanova N, et al. (2010) Experimental evidence for perovskite and post-perovskite coexistence throughout the whole D″ region. *Earth and Planetary Science Letters* 293: 90–96.
Andrault D, Petitgirard S, Nigro GL, et al. (2012) Solid–liquid iron partitioning in Earth's deep mantle. *Nature* 487: 354–357.
Anzellini S, Dewaele A, Mezouar M, Loubeyre P, and Morard G (2013) Melting of iron at Earth's inner core boundary based on fast X-ray diffraction. *Science* 340: 464–466.
Armitage JJ, Jaupart C, Fourel L, and Allen PA (2013) The instability of continental passive margins and its effect on continental topography and heat flow. *Journal of Geophysical Research* 118: 1817–1836.
Ashwal LD, Morgan P, Kelley SA, and Percival J (1987) Heat production in an Archean crustal profile and implications for heat flow and mobilization of heat producing elements. *Earth and Planetary Science Letters* 85: 439–450.
Barreyre T, Escartín J, Garcia R, Cannat M, Mittelstaedt E, and Prados R (2012) Structure, temporal evolution, and heat flux estimates from the Lucky Strike deep-sea hydrothermal field derived from seafloor image mosaics. *Geochemistry, Geophysics, Geosystems* 13: 4007.
Becker TW, Conrad CP, Buffett BA, and Müller RD (2009) Past and present seafloor age distributions and the temporal evolution of plate tectonic heat transport. *Earth and Planetary Science Letters* 278: 233–242.
Bender PL, et al. (1973) The Lunar Laser Ranging Experiment. *Science* 182: 229–238.
Birch F (1965) Speculations on the thermal history of the Earth. *Geological Society of America Bulletin* 76: 133–154.
Birch F, Roy RF, and Decker ER (1968) Heat flow and thermal history in New England and New York. In: An-Zen E (ed.) *Studies of Appalachian Geology*, pp. 437–451. New York: Wiley-Interscience.
Bird RB, Stewart WE, and Lightfoot EN (1960) *Transport Phenomena*. New York: Wiley.
Bodell JM and Chapman DS (1982) Heat flow in the north central Colorado plateau. *Journal of Geophysical Research* 87: 2869–2884.
Boillot G, Grimaud S, Mauffret A, et al. (1980) Ocean–continent boundary off the Iberian margin: A serpentinite diapir west of the Galicia Bank. *Earth and Planetary Science Letters* 48: 23–24.
Bonneville A, Von Herzen RP, and Lucazeau F (1997) Heat flow over Reunion hot spot track: Additional evidence for thermal rejuvenation of oceanic lithosphere. *Journal of Geophysical Research* 102: 22731–22748.
Borexino Collaboration Group (Bellini, G., 88 Collaborators) (2013) Measurement of geo-neutrinos from 1353 days of Borexino. *Physics Letters B* 722: 295–300.
Borexino Collaboration Group (Bellini, G., 89 Collaborators) (2010) Measurement of geo-neutrinos from 1353 days of Borexino. *Physics Letters B* 687: 299–304.
Boyet M and Carlson RW (2005) $^{142}$Nd evidence for early (>4.53 Ga) global differentiation of the silicate Earth. *Science* 309: 576–581.
Boyet M and Gannoun A (2013) Nucleosynthetic Nd isotope anomalies in primitive enstatite chondrites. *Geochimica et Cosmochimica Acta* 121: 652–666.
Bradley DC (2008) Passive margins through earth history. *Earth-Science Reviews* 91: 1–26.
Brady RJ, Ducea MN, Kidder SB, and Saleeby JB (2006) The distribution of radiogenic heat production as a function of depth in the Sierra Nevada Batholith, California. *Lithos* 86: 229–244.
Braginsky SI and Roberts PH (1995) Equations governing convection in Earth's core and the geodynamo. *Geophysical and Astrophysical Fluid Dynamics* 79: 1–97.
Breuer D and Spohn T (1993) Cooling of the earth, Urey ratios, and the problem of potassium in the core. *Geophysical Research Letters* 20: 1655–1658.
Calves G, Schwab AM, Huuse M, Clift PD, and Inam A (2010) Thermal regime of the northwest Indian rifted margin – Comparison with predictions. *Marine and Petroleum Geology* 27: 1133–1147.
Cameron AGW (2001) From interstellar gas to the Earth–Moon system. *Meteoritics and Planetary Science* 36: 9–22.
Canup RM (2004) Simulations of a late lunar-forming impact. *Icarus* 168: 433–456.
Canup RM and Righter K (eds.) (2000) *Origin of the Earth and Moon*. Tucson, AZ: University of Arizona Press.
Carlson RL and Johnson HP (1994) On modeling the thermal evolution of the oceanic upper mantle: An assessment of the cooling plate model. *Journal of Geophysical Research* 99: 3201–3214.
Caro G and Bourdon B (2010) Non-chondritic Sm/Nd ratio in the terrestrial planets: Consequences for the geochemical evolution of the mantle–crust system. *Geochimica et Cosmochimica Acta* 74: 3333–3349.
Caro G, Bourdon B, Birck J-L, and Moorbath S (2003) $^{146}$Sm–$^{142}$Nd evidence from Isua metamorphosed sediments for early differentiation of the Earth's mantle. *Nature* 423: 428–432. http://dx.doi.org/10.1038/nature01668.
Caro G, Bourdon B, Halliday AN, and Quitte G (2008) Super-chondritic Sm/Nd ratios in mars, the earth and the moon. *Nature* 452: 336–339.
Carslaw HS and Jaeger JC (1959) *Conduction of Heat in Solids*, 2nd edn. Oxford: Clarendon Press.
Catalli K, Shim S-H, and Prakapenka VB (2009) Thickness and Clapeyron slope of the post-perovskite boundary. *Nature* 462: 782–785.
CCGM/CGMW (2000) *Geological Map of the World at 1:25 000 000*, 2nd edn. CD Rom, http://ccgm.free.fr/cartes_monde_gb.html.
Cermak V and Bodri L (1986) Two-dimensional temperature modelling along five East-European geotraverses. *Journal of Geodynamics* 5: 133–163.
Chapman DS and Pollack HN (1974) 'Cold spot' in West Africa: Anchoring the African plate. *Nature* 250: 477–478.
Christensen UR (1984) Heat transport by variable viscosity convection and implications for the Earth's thermal evolution. *Physics of the Earth and Planetary Interiors* 35: 264–282.
Christensen UR (1985) Thermal evolution models for the earth. *Journal of Geophysical Research* 90: 2995–3007.
Christensen UR (2010) Dynamo scaling laws and applications to the planets. *Space Science Reviews* 152: 565–590.
Clauser C, et al. (1997) The thermal regime of the crystalline continental crust: Implications from the KTB. *Journal of Geophysical Research* 102: 18417–18441.
Cochran JR (1981) Simple models of diffuse extension and the pre-seafloor spreading development of the continental margin of the Northeastern Gulf of Aden. *Oceanologica Acta* 4(supplement): 155–165.
Cogley JG (1984) Continental margins and the extent and number of continents. *Reviews of Geophysics and Space Physics* 22: 101–122.
Cogné J-P and Humler E (2004) Temporal variation of oceanic spreading and crustal production rates during the last 180 My. *Earth and Planetary Science Letters* 227: 427–439.
Coltice N, Rolf T, Tackley PJ, and Labrosse S (2012) Dynamic causes of the relation between area and age of the ocean floor. *Science* 336: 335–338.
Condie KC (1998) Episodic continental growth and supercontinents: A mantle avalanche connection? *Earth and Planetary Science Letters* 163: 231–246.
Conrad CP and Hager BH (1999) The thermal evolution of an earth with strong subduction zones. *Geophysical Research Letters* 26: 3041–3044.
Courtney R and White R (1986) Anomalous heat flow and geoid across the Cape Verde Rise: Evidence of dynamic support from a thermal plume in the mantle. *Geophysical Journal of the Royal Astronomical Society* 87: 815–868.
Crane K and O'Connell S (1983) The distribution and implications of the heat flow from the Gregory rift in Kenya. *Tectonophysics* 94: 253–272.
Crosby AG and McKenzie D (2009) An analysis of young ocean depth, gravity and global residual topography. *Geophysical Journal International* 178: 1198–1219.
Crough ST (1983) Hotspot swells. *Annual Review of Earth and Planetary Sciences* 11: 165–193.
Cull JP (1991) Heat flow and regional geophysics in Australia. In: Cermak V and Rybach L (eds.) *Terrestrial Heat Flow and the Lithosphere Structure*, pp. 486–500. Berlin: Springer.
Davaille A and Jaupart C (1993) Transient high-Rayleigh-number thermal convection with large viscosity variations. *Journal of Fluid Mechanics* 253: 141–166.
Davies GF (1980a) Thermal histories of convective Earth models and constraints on radiogenic heat production in the Earth. *Journal of Geophysical Research* 85: 2517–2530.
Davies GF (1980b) Review of oceanic and global heat flow estimates. *Reviews of Geophysics and Space Physics* 18: 718–722.
Davies GF (1988) Ocean bathymetry and mantle convection, 1. Large-scale flow and hotspots. *Journal of Geophysical Research* 93: 10467–10480.
Davies GF (1999) *Dynamic Earth: Plates, Plumes, and Mantle Convection*. Cambridge: Cambridge University Press.
Davies JH and Davies DR (2010) Earth's surface heat flux. *Solid Earth* 1: 5–24.
Davis EE and Elderfield H (2004) *Hydrogeology of the Oceanic Lithosphere*. Cambridge: Cambridge University Press.
Davis EE and Lister CRB (1974) Fundamentals of ridge crest topography. *Earth and Planetary Science Letters* 21: 405–413.
Davis EE, et al. (1999) Regional heat flow variations across the sedimented Juan de Fuca ridge eastern flank: Constraints on lithospheric cooling and lateral hydrothermal heat transport. *Journal of Geophysical Research* 104: 17675–17688.
de Koker N, Karki BB, and Stixrude LP (2013) Thermodynamics of the MgO–$SiO_2$ liquid system in Earth's lowermost mantle from first principles. *Earth and Planetary Science Letters* 361: 58–63.
de Koker N, Steinle-Neumann G, and Vlček V (2012) Electrical resistivity and thermal conductivity of liquid Fe alloys at high P and T, and heat flux in earth's core. *Proceedings of the National Academy of Sciences of the United States of America* 109: 4070–4073.
Deming D, Sass JH, and Lachenbruch AH (1992) and R. F. D. Rito1, Heat flow and subsurface temperature as evidence for basin-scale ground-water flow, North Slope of Alaska. *Geological Society of America Bulletin* 104: 528–542.

Donnelly KE, Goldstein SL, Langmuir CH, and Spiegelman M (2004) Origin of enriched ocean ridge basalts and implications for mantle dynamics. *Earth and Planetary Science Letters* 226: 347–366.
Duchkov AD (1991) Review of Siberian heat flow data. In: Cermak V and Rybach L (eds.) *Terrestrial Heat Flow and the Lithosphere Structure*, pp. 426–443. Berlin: Springer.
Dunn RA, Toomey DR, and Solomon SC (2000) Three-dimensional seismic structure and physical properties of the crust and shallow mantle beneath the East Pacific Rise at 9 30′N. *Journal of Geophysical Research* 105: 23537–23555.
Dye ST (2010) Geo-neutrinos and silicate earth enrichment of U and Th. *Earth and Planetary Science Letters* 297: 1–9.
Dye ST (2012) Geoneutrinos and the radioactive power of the Earth. *Reviews of Geophysics* 50: 3007.
Dye ST, Guillian E, Learned JG, et al. (2006) Earth radioactivity measurements with a deep ocean anti-neutrino observatory. *Earth, Moon, and Planets* 99: 241–252.
Dziewonski AM and Anderson DL (1981) Preliminary reference Earth model. *Physics of the Earth and Planetary Interiors* 25: 297–356.
Elkins-Tanton LT, Parmentier EM, and Hess PC (2003) Magma ocean fractional crystallization and cumulate overturn in terrestrial planets: Implications for Mars. *Meteoritics and Planetary Science* 38: 1753–1771.
Engebretson DC, Cox A, and Gordon RG (1984) Relative motions between oceanic plates of the Pacific basin. *Journal of Geophysical Research* 89: 10291–10310.
England PC, Oxburg ER, and Richardson SW (1980) Heat refraction in and around granites in north-east England. *Geophysical Journal of the Royal Astronomical Society* 62: 439–455.
Enomoto S, Ohtani E, Inoue K, and Suzuki A (2007) Neutrino geophysics with KamLAND and future prospects. *Earth and Planetary Science Letters* 258: 147–159.
Erickson AJ, Von Herzen RP, Sclater JG, Girdler RW, Marshall BV, and Hyndman R (1975) Geothermal measurements in Deep-Sea drill holes. *Journal of Geophysical Research* 80: 2515–2528.
Fiorentini G, Lissia M, Mantovani F, and Vannucci R (2005) Geo-neutrinos: A new probe of Earth's interior [rapid communication]. *Earth and Planetary Science Letters* 238: 235–247.
Fiquet G, Auzende AL, Siebert J, et al. (2010) Melting of peridotite to 140 gigapascals. *Science* 329: 1516–1518.
Fitoussi C and Bourdon B (2012) Silicon isotope evidence against an enstatite chondrite Earth. *Science* 335: 1477–1480.
Flasar FM and Birch F (1973) Energetics of core formation: A correction. *Journal of Geophysical Research* 78: 6101–6103.
Fountain DM and Salisbury MH (1981) Exposed cross-sections through the continental crust: Implications for crustal structure, petrology, and evolution. *Earth and Planetary Science Letters* 56: 263–277.
Fountain DM, Salisbury MH, and Furlong KP (1987) Heat production and thermal conductivity of rocks from the Pikwitonei–Sachigo continental cross-section, central Manitoba: Implications for the thermal structure of Archean crust. *Canadian Journal of Earth Sciences* 24: 1583–1594.
Fourier JBJ (1824) Remarques générales sur les températures du globe terrestre et des espaces planétaires. *Annales des Chimie et des Physique* 27: 136–167.
Fournier RO (1989) Geochemistry and dynamics of the Yellowstone National Park hydrothermal system. *Annual Review of Earth and Planetary Sciences* 17: 13–53.
Francheteau J, Jaupart C, Jie SX, et al. (1984) High heat flow in southern Tibet. *Nature* 307: 32–36.
Golabek GJ, Schmeling H, and Tackley PJ (2008) Earth's core formation aided by flow channelling instabilities induced by iron diapirs. *Earth and Planetary Science Letters* 271: 24–33.
Gomi H, Ohta K, Hirose K, et al. (2013) The high conductivity of iron and thermal evolution of the earth's core. *Physics of the Earth and Planetary Interiors* 224: 88–103.
Gordon RG (2000) Diffuse oceanic plate boundaries: Strain rates, vertically averaged rheology, and comparisons with narrow plate boundaries and stable plate interiors. In: Richards MA, Gordon RG, and van der Hilst RD (eds.) *The History and Dynamics of Global Plate Motions*. *Geophysical Monograph Series*, vol. 121, pp. 143–159. Washington, DC: American Geophysical Union.
Goutorbe B, Drab L, Loubet N, and Lucazeau F (2007) Heat-flow revisited on the eastern Canadian Shield shelf. *Terra Nova* 19: 381–386.
Goutorbe B, Lucazeau F, and Bonneville A (2008a) The thermal regime of South African continental margins. *Earth and Planetary Science Letters* 267: 256–265.
Goutorbe B, Lucazeau F, and Bonneville A (2008b) The surface heat flow and the mantle contribution on the margins of Australia. *Geochemistry, Geophysics, Geosystems* 267: 256–265.
Green DH (1975) Genesis of Archean peridotitic magmas and constraints on Archean geothermal gradients and tectonics. *Geology* 3: 15–18.
Grigné C and Labrosse S (2001) Effects of continents on Earth cooling: Thermal blanketing and depletion in radioactive elements. *Geophysical Research Letters* 28: 2707–2710.
Grigné C, Labrosse S, and Tackley PJ (2005) Convective heat transfer as a function of wavelength: Implications for the cooling of the Earth. *Journal of Geophysical Research* 110: B03409. http://dx.doi.org/10.1029/2004JB003376.
Grigne C, Labrosse S, and Tackley PJ (2007) Convection under a lid of finite conductivity in wide aspect ratio models: Effect of continents on the wavelength of mantle flow. *Journal of Geophysical Research* 112(B08): 403–414.
Grocholski B, Catalli K, Shim S-H, and Prakapenka V (2012) Mineralogical effects on the detectability of the postperovskite boundary. *Proceedings of the National Academy of Sciences of the United States of America* 109: 2275–2279.
Grove TL and Parman SW (2004) Thermal evolution of the Earth as recorded by komatiites. *Earth and Planetary Science Letters* 219: 173–187.
Gubbins D and Roberts PH (1987) Magnetohydrodynamics of the Earth's core. In: Jacobs JA (ed.). *Geomagnetism*, vol. 2, pp. 1–183. London: Academic Press.
Gubbins D, Thomson CJ, and Whaler KA (1982) Stable regions in the Earth's liquid core. *Geophysical Journal of the Royal Astronomical Society* 68: 241–251.
Guillou L and Jaupart C (1995) On the effect of continents on mantle convection. *Journal of Geophysical Research* 100: 24217–24238.
Guillou L, Mareschal JC, Jaupart C, Gariépy C, Bienfait G, and Lapointe R (1994) Heat flow and gravity structure of the Abitibi belt, Superior Province, Canada. *Earth and Planetary Science Letters* 122: 447–460.
Guillou-Frottier L, Mareschal J-C, Jaupart C, Gariépy C, Lapointe R, and Bienfait G (1995) Heat flow variations in the Grenville Province, Canada. *Earth and Planetary Science Letters* 136: 447–460.
Gupta ML, Sharma SR, and Sundar A (1991) Heat flow and heat generation in the Archean Dharwar craton and implication for the southern Indian Shield geotherm. *Tectonophysics* 194: 107–122.
Harris RN and Chapman DS (2004) Deep-seated oceanic heat flow, heat deficits, and hydrothermal circulation. In: Davis EE and Elderfield H (eds.) *Hydrogeology of the Oceanic Lithosphere*, pp. 311–336. Cambridge: Cambridge University Press.
Hart SR and Zindler A (1986) In search of a bulk-Earth composition. *Chemical Geology* 57: 247–267.
Hasterok D (2013) A heat flow based cooling model for tectonic plates. *Earth and Planetary Science Letters* 361: 34–43.
Hasterok D, Chapman DS, and Davis EE (2011) Oceanic heat flow: Implications for global heat loss. *Earth and Planetary Science Letters* 311: 386–395.
Henry SG and Pollack HN (1988) Terrestrial heat flow above the Andean subduction zone in Bolivia and Peru. *Journal of Geophysical Research* 93: 15153–15162.
Henry P and Wang C-Y (1991) Modeling of fluid flow and pore pressure at the toe of Oregon and Barbados Accretionary Wedges. *Journal of Geophysical Research* 96: 20109–20130.
Hernlund JW and Labrosse S (2007) Geophysically consistent values of the perovskite to post-perovskite transition Clapeyron slope. *Geophysical Research Letters* 34: L05309.
Hernlund JW, Thomas C, and Tackley PJ (2005) Phase boundary double crossing and the structure of Earth's deep mantle. *Nature* 434: 882–886. http://dx.doi.org/10.1038/nature03472.
Herzberg C, Condie K, and Korenaga J (2010) Thermal history of the Earth and its petrological expression. *Earth and Planetary Science Letters* 292: 79–88.
Herzberg C and Zhang J (1996) Melting experiments on anhydrous peridotite KLB-1: Compositions of magmas in the upper mantle and transition zone. *Journal of Geophysical Research* 101: 8271–8296.
Hillier JK (2010) Subsidence of normal seafloor: Observations do indicate flattening. *Journal of Geophysical Research* 115: B03102.
Hillier JK and Watts AB (2005) Relationship between depth and age in the North Pacific Ocean. *Journal of Geophysical Research* 110: B02405.
Hirose K (2006) Postperovskite phase transition and its geophysical implications. *Reviews of Geophysics* 44: RG3001. http://dx.doi.org/10.1029/2005RG000186.
Hirose K, Gomi H, Ohta K, Labrosse S, and Hernlund JW (2011) The high conductivity of iron and thermal evolution of the Earth's core. *Mineralogical Magazine* 75: 1027.
Hirose K, Labrosse S, and Hernlund JW (2013) Composition and state of the core. *Annual Review of Earth and Planetary Sciences* 41: 657–691.
Hochmuth KA, Feilitzsch FV, Fields BD, et al. (2007) Probing the Earth's interior with a large-volume liquid scintillator detector. *Astroparticle Physics* 27: 21–29.
Hoffman PF (1997) Tectonic geology of North America. In: van der Pluijm B and Marshak S (eds.) *Earth Structure: An Introduction to Structural Geology and Tectonics*, pp. 459–464. New York: McGraw Hill.
Holmes A (1915) Radioactivity and the earth's thermal history: Part 1. The concentration of radioactive elements in the earth's crust. *Geological Magazine* 2: 60–71.

Howard LN (1964) Convection at high Rayleigh number. In: Gortler H (ed.) *Proceedings of the Eleventh International Congress of Applied Mechanics*, pp. 1109–1115. New York: Springer.
Hu S, He L, and Wang J (2000) Heat flow in the continental area of China: A new data set. *Earth and Planetary Science Letters* 179: 407–419.
Huismans R and Beaumont C (2011) Depth-dependent extension, two-stage breakup and cratonic underplating at rifted margins. *Nature* 473: 74–78.
Hulot G, Eymin C, Langlais B, Mandea M, and Olsen N (2002) Small-scale structure of the geodynamo inferred from Oersted and Magsat satellite data. *Nature* 416: 620–623.
Hulot G, Khoklov A, and LeMouel JL (1967) Uniqueness of mainly dipolar magnetic field recovered from directional data. *Geophysical Journal International* 129: 347–354.
Humler E, Langmuir C, and Daux V (1999) Depth versus age: New perspectives from the chemical compositions of ancient crust. *Earth and Planetary Science Letters* 173: 7–23.
Husson L, Pichon XLL, Henry P, Flotte N, and Rangin C (2008) Thermal regime of the NW shelf of the Gulf of Mexico, Part B: Heat flow. *Bulletin de la Société Géologique de France* 179: 139–145.
Hyndman RD (2010) The consequences of Canadian Cordillera thermal regime in recent tectonics and elevation: A review. *Canadian Journal of Earth Sciences* 47: 621–632.
Hyndman RD, Wang K, Yuan T, and Spence GD (1993) Tectonic sediment thickening, fluid expulsion, and the thermal regime of subduction zone accretionary prisms: The Cascadia margin off Vancouver Island. *Journal of Geophysical Research* 98: 21865–21876.
Ichikawa H, Labrosse S, and Kurita K (2010) Direct numerical simulation of an iron rain in the magma ocean. *Journal of Geophysical Research* 115: B01404.
Irifune T and Isshiki M (1998) Iron partitioning in a pyrolite mantle and the nature of the 410-km seismic discontinuity. *Nature* 392: 702–705.
Ito E and Katsura T (1989) A temperature profile of the mantle transition zone. *Geophysical Research Letters* 16: 425–428.
Jackson MG and Jellinek AM (2013) Major and trace element composition of the high $^{3}He/^{4}He$ mantle: Implications for the composition of a nonchonditic earth. *Geochemistry, Geophysics, Geosystems* 14: 2954–2976.
Jacobs JA (1961) Some aspects of the thermal history of the Earth. *Geophysical Journal of the Royal Astronomical Society* 4: 267–275.
Jacobs J and Allan DW (1956) The thermal history of the earth. *Nature* 177: 155–157.
Jarvis GT and Campbell IH (1983) Archean komatiites and geotherms – Solution to an apparent contradiction. *Geophysical Research Letters* 10: 1133–1136.
Jaupart C (1983) Horizontal heat transfer due to radioactivity contrasts: Causes and consequences of the linear heat flow-heat production relationship. *Geophysical Journal of the Royal Astronomical Society* 48: 411–435.
Jaupart C, Francheteau J, and Shen X-J (1985) On the thermal structure of the southern Tibetan crust. *Geophysical Journal of the Royal Astronomical Society* 81: 131–155.
Jaupart C, Mann JR, and Simmons G (1982) A detailed study of the distribution of heat flow and radioactivity in New Hampshire (U.S.A.). *Earth and Planetary Science Letters* 59: 267–287.
Jaupart C and Mareschal JC (1999) The thermal structure and thickness of continental roots. *Lithos* 48: 93–114.
Jaupart C and Mareschal JC (2013) Constraints on crustal heat production from heat flow data. In: Rudnick RL (ed.) *Treatise on Geochemistry. The Crust*, 2nd edn., vol. 3, pp. 65–84. New York: Pergamon.
Javoy M (1995) The integral enstatite chondrite model of the earth. *Geophysical Research Letters* 22: 2219–2222.
Javoy M (1999) Chemical Earth models. *Comptes Rendus de l'Acadêmie des Sciences, Paris* 329: 537–555.
Javoy M, et al. (2010) The chemical composition of the Earth: Enstatite chondrite models. *Earth and Planetary Science Letters* 293: 259–268.
Jeffreys S (1962) *The Earth: Its Origin, History, and Physical Constitution*, 5th edn. Cambridge: Cambridge University Press.
Joeleht TH and Kukkonen IT (1998) Thermal properties of granulite facies rocks in the Precambrian basement of Finland and Estonia. *Tectonophysics* 291: 195–203.
Joly J (1909) *Radioactivity and Geology*. Dublin: Dublin University Press.
Jones MQW (1988) Heat flow in the Witwatersrand Basin and environs and its significance for the South African Shield geotherm and lithosphere thickness. *Journal of Geophysical Research* 93: 3243–3260.
Kaminski E and Javoy M (2013) A two-stage scenario for the formation of the earth's mantle and core. *Earth and Planetary Science Letters* 365: 97–107.
Kamland Collaboration (2011) Partial radiogenic heat model for Earth revealed by geoneutrino measurements. *Nature Geosciences* 4: 647–651.
Kamland Collaboration (Gando, A., 45 Collaborators) (2013) Reactor on-off antineutrino measurement with KamLAND. *Physical Review D* 88: 033001.
Katsura T, et al. (2003) Post-spinel transition in $MgSiO_4$ determined by in-situ X-ray diffractometry. *Physics of the Earth and Planetary Interiors* 136: 11–24.
Katsura T, et al. (2004) Olivine–Wadsleyite transition in the system (Mg, Fe)$SiO_4$. *Journal of Geophysical Research* 109: B02209.
Kellogg LH, Hager BH, and van der Hilst RD (1999) Compositional stratification in the deep mantle. *Science* 283: 1881–1884.
Ketcham RA (1996) Distribution of heat-producing elements in the upper and middle crust of southern and west central Arizona: Evidence from the core complexes. *Journal of Geophysical Research* 101(13): 13611–13632.
King SD and Anderson DL (1998) Edge-driven convection. *Earth and Planetary Science Letters* 160: 289–296.
Kinzler RJ and Grove TL (1992) Primary magmas of mid-ocean ridge basalts. 2. Applications. *Journal of Geophysical Research* 97: 6907–6926.
Klein EM and Langmuir CH (1987) Global correlations of ocean ridge basalt chemistry with axial depth and crustal thickness. *Journal of Geophysical Research* 92: 8089–8115.
Kleine T, Münker C, Mezger K, and Palme H (2002) Rapid accretion and early core formation on asteroids and the terrestrial planets from Hf-W chronometry. *Nature* 418: 952–955.
Korenaga J (2003) Energetics of mantle convection and the fate of fossil heat. *Geophysical Research Letters* 30: 20. http://dx.doi.org/10.1029/2003GL016982.
Korenaga J (2006) Archean geodynamics and the thermal evolution of the earth. In: Benn K, Mareschal J, and Condie KC (eds.) *Archean Geodynamics and Environments*. *Geophysical Monograph Series*, vol. 164, pp. 7–32. Washington, DC: American Geophysical Union.
Korenaga T and Korenaga J (2008) Subsidence of normal oceanic lithosphere, apparent thermal expansivity, and sea floor flattening. *Earth and Planetary Science Letters* 268: 41–51.
Kremenentsky AA, Milanovsky SY, and Ovchinnikov LN (1989) A heat generation model for the continental crust based on deep drilling in the Baltic shield. *Tectonophysics* 159: 231–246.
Kukkonen IT and Peltonen P (1999) Xenolith-controlled geotherm for the central Fennoscandian shield: Implications for lithosphere–asthenosphere relations. *Tectonophysics* 304: 301–315.
Labrosse S (2002) Hotspots, mantle plumes and core heat loss. *Earth and Planetary Science Letters* 199: 147–156.
Labrosse S (2003) Thermal and magnetic evolution of the Earth's core. *Physics of the Earth and Planetary Interiors* 140: 127–143.
Labrosse S (2005a) Core-mantle boundary, heat flow across. In: Gubbins D and Herrero-Bervera E (eds.) *Encyclopedia of Geomagnetism and Paleomagnetism*, pp. 127–130. Dordrecht, The Netherlands: Springer.
Labrosse S (2005b) Geodynamo, energy sources. In: Gubbins D and Herrero-Bervera E (eds.) *Encyclopedia of Geomagnetism and Paleomagnetism*, pp. 300–302. Dordrecht, The Netherlands: Springer.
Labrosse S, Hernlund JW, and Coltice N (2007) A crystallizing dense magma ocean at the base of Earth's mantle. *Nature* 450: 866–869.
Labrosse S and Jaupart C (2007) Thermal evolution of the Earth: Secular changes and fluctuations of plate characteristics. *Earth and Planetary Science Letters* 260: 465–481.
Labrosse S, Poirier J-P, and Le Mouël J-L (1997) On cooling of the Earth's core. *Physics of the Earth and Planetary Interiors* 99: 1–17.
Lachenbruch AH (1970) Crustal temperature and heat production: Implications of the linear heat flow heat production relationship. *Journal of Geophysical Research* 73: 3292–3300.
Lachenbruch AH and Sass JH (1978) Models of an extending lithosphere and heat flow in the Basin and Range province. *Memoirs of the Geological Society of America* 152: 209–258.
Lallemand S, Heuret A, and Boutelier D (2005) On the relationships between slab dip, back-arc stress, upper plate absolute motion, and crustal nature in subduction zones. *Geochemistry, Geophysics, Geosystems* 6: 1–18. http://dx.doi.org/10.1029/2005GC000917.
Lambeck K (1977) Tidal dissipation in the oceans: Astronomical, geophysical, and oceanographic consequences. *Philosophical Transactions of the Royal Society of London, Series A* 287: 545–594.
Langmuir CH, Goldstein SL, Donnelly K, and Su YK (2005) Origins of enriched and depleted mantle reservoirs. *EOS Transactions*. *Fall Meeting Supplement*, vol. 86, p. 1. Washington, DC: American Geophysical Union, Abstract V23D-02.
Lapwood ER (1952) The effect of contraction in the cooling of a gravitating sphere, with special reference to the Earth. *Monthly Notices of the Royal Astronomical Society, Geophysical Supplement* 6: 402–407.

Latil-Brun MV and Lucazeau F (1988) Subsidence, extension and thermal history of the West African margin in Senegal. *Earth and Planetary Science Letters* 90: 204–220.

Lay T, Hernlund J, Garnero EJ, and Thorne MS (2006) A post-perovskite lens and D″ heat flux beneath the central Pacific. *Science* 314: 1272. http://dx.doi.org/10.1126/science.1133280.

Lenardic A, Moresi L-N, Jellinek A, and Manga M (2005) Continental insulation, mantle cooling, and the surface area of oceans and continents. *Earth and Planetary Science Letters* 234: 317–333.

Leng W and Zhong S (2010) Constraints on viscous dissipation of plate bending from compressible mantle convection. *Earth and Planetary Science Letters* 297: 154–164.

Lévy F, Jaupart C, Mareschal J, Bienfait G, and Limare A (2010) Low heat flux and large variations of lithospheric thickness in the Canadian Shield. *Journal of Geophysical Research* 115: 6404.

Lewis TJ, Hyndman RD, and Fluck P (2003) Heat flow, heat generation and crustal temperatures in the northern Canadian Cordillera: Thermal control on tectonics. *Journal of Geophysical Research* 108: 2316.

Lister CRB (1977) Estimators for heat flow and deep rock properties based on boundary layer theory. *Tectonophysics* 41: 157–171.

Lister JR (2003) Expressions for the dissipation driven by convection in the Earth's core. *Physics of the Earth and Planetary Interiors* 140: 145–158.

Lister JR and Buffett BA (1995) The strength and efficiency of the thermal and compositional convection in the geodynamo. *Physics of the Earth and Planetary Interiors* 91: 17–30.

Lister JR and Buffett BA (1998) Stratification of the outer core at the core–mantle boundary. *Physics of the Earth and Planetary Interiors* 105: 5–19.

Lister CRB, Sclater JG, Nagihara S, Davis EE, and Villinger H (1990) Heat flow maintained in ocean basins of great age – Investigations in the north-equatorial West Pacific. *Geophysical Journal International* 102: 603–630.

Litasov K and Ohtani E (2002) Phase relations and melt compositions in CMAS–pyrolite–$H_2O$ system up to 25 GPa. *Physics of the Earth and Planetary Interiors* 134: 105–127.

Louden KE, Sibuet J-C, and Harmegnies F (1997) Variations in heat flow across the ocean–continent transition in the Iberia abyssal plain. *Earth and Planetary Science Letters* 151: 233–254.

Lucazeau F, Bonneville A, Escartin J, et al. (2006) Heat flow variations on a slowly accreting ridge: Constraints on the hydrothermal and conductive cooling for the Lucky Strike segment (Mid-Atlantic Ridge, 37°N). *Geochemistry, Geophysics, Geosystems* 7: 7011.

Lucazeau F, Brigaud F, and Bouroullec JL (2004) High-resolution heat flow density in the lower Congo basin. *Geochemistry, Geophysics, Geosystems* 5: 3001.

Lucazeau F, Leroy S, Rolandone F, et al. (2010) Heat-flow and hydrothermal circulation at the ocean–continent transition of the eastern Gulf of Aden. *Earth and Planetary Science Letters* 295: 554–570.

Lucazeau F, et al. (2008) Persistent thermal activity at the Eastern Gulf of Aden after continental break-up. *Nature Geoscience* 1: 854–858.

Lyubetskaya T and Korenaga J (2007) Chemical composition of Earth's primitive mantle and its variance: 1. Method and results. *Journal of Geophysical Research* 112: 3211.

MacDonald GJF (1959) Calculations on the thermal history of the Earth. *Journal of Geophysical Research* 64: 1967–2000.

Marcaillou B, Spence G, Collot J-Y, and Wang K (2006) Thermal regime from bottom simulating reflectors along the north Ecuador-south Colombia margin: Relation to margin segmentation and great subduction earthquakes. *Journal of Geophysical Research* 111: 12407.

Mareschal JC and Jaupart C (2004) Variations of surface heat flow and lithospheric thermal structure beneath the North American craton. *Earth and Planetary Science Letters* 223: 65–77.

Mareschal JC, Jaupart C, Cheng LZ, et al. (1999) Heat flow in the Trans-Hudson Orogen of the Canadian Shield: Implications for Proterozoic continental growth. *Journal of Geophysical Research* 104: 29007–29024.

Mareschal JC, Jaupart C, Gariépy C, et al. (2000a) Heat flow and deep thermal structure near the southeastern edge of the Canadian Shield. *Canadian Journal of Earth Sciences* 37: 399–414.

Mareschal J-C, Jaupart C, Phaneuf C, and Perry C (2012) Geoneutrinos and the energy budget of the Earth. *Journal of Geodynamics* 54: 43–54.

Mareschal JC, Jaupart C, Rolandone F, et al. (2005) Heat flow, thermal regime, and rheology of the lithosphere in the Trans-Hudson Orogen. *Canadian Journal of Earth Sciences* 42: 517–532.

Mareschal JC, Poirier A, Rolandone F, et al. (2000b) Low mantle heat flow at the edge of the North American Continent, Voisey Bay, Labrador. *Geophysical Research Letters* 27: 823–826.

Martínez F and Cochran JR (1989) Geothermal measurements in the northern Red Sea: Implications for lithospheric thermal structure and mode of extension during continental rifting. *Journal of Geophysical Research* 94: 12239–12265.

McDonald GJF (1959) Calculations on the thermal history of the earth. *Journal of Geophysical Research* 64: 1967–2000.

McDonough WF and Sun SS (1995) The composition of the earth. *Chemical Geology* 120: 223–253.

McKenna TE and Sharp JM Jr. (1998) Radiogenic heat production in sedimentary rocks of the Gulf of Mexico basin, south Texas. *American Association of Petroleum Geologists Bulletin* 82: 484–496.

McKenzie D (1978) Some remarks on the development of sedimentary basins. *Earth and Planetary Science Letters* 40: 25–32.

McKenzie D and Bickle M (1988) The volume and composition of melt generated by extension of the lithosphere. *Journal of Petrology* 29: 625–679.

McKenzie D, Jackson J, and Priestley K (2005) Thermal structure of oceanic and continental lithosphere. *Earth and Planetary Science Letters* 233: 337–349.

McKenzie D and Richter FM (1981) Parameterized thermal convection in a layered region and the thermal history of the Earth. *Journal of Geophysical Research* 86: 11667–11680.

McKenzie DP and Weiss N (1975) Speculations on the thermal and tectonic history of the earth. *Geophysical Journal* 42: 131–174.

McLennan J, Hulme T, and Singh SC (2005) Cooling of the lower oceanic crust. *Geology* 33: 357.

Melosh HJ and Ivanov BA (1999) Impact crater collapse. *Annual Review of Earth and Planetary Sciences* 27: 385–415.

Mittelstaedt E, Escartín J, Gracias N, et al. (2012) Quantifying diffuse and discrete venting at the Tour Eiffel vent site, Lucky Strike hydrothermal field. *Geochemistry, Geophysics, Geosystems* 13: 4008.

Mojzsis SJ, Harrison TM, and Pidgeon RT (2001) Oxygen-isotope evidence from ancient zircons for liquid water at the Earth's surface 4,300 Myr ago. *Nature* 409: 178–181.

Molnar P and England P (1990) Temperatures, heat flux, and frictional stress near major thrust faults. *Journal of Geophysical Research* 95: 4833–4856.

Monteux J, Ricard YR, Coltice N, Dubuffet F, and Ulvrová M (2009) A model of metal–silicate separation on growing planets. *Earth and Planetary Science Letters* 287: 353–362.

Morgan P (1983) Constraints on rift thermal processes from heat flow and uplift. *Tectonophysics* 94: 277–298.

Müller RD, Roest WR, Royer J-Y, Gahagan LM, and Sclater JG (1997) Digital isochrons of the world's ocean floor. *Journal of Geophysical Research* 102: 3211–3214.

Müller RD, Sdrolias M, Gaina C, and Roest WR (2008) Age, spreading rates, and spreading asymmetry of the world's ocean crust. *Geochemistry, Geophysics, Geosystems* 9: 4006.

Munk WH and MacDonald GJF (1960) *The Rotation of the Earth*. Cambridge: Cambridge University Press.

Murakami M, Hirose K, Kawamura K, Sata N, and Ohishi Y (2004) Post-perovskite phase transition in $MgSiO_3$. *Science* 304: 855–858.

Nagihara S and Opre K (2005) Jones, Geothermal heat flow in the northeast margin of the Gulf of Mexico. *American Association of Petroleum Geologists Bulletin* 89: 821–831.

Newsom HE and Jones JH (eds.) (1990) *Origin of the Earth*. Oxford: Oxford University Press.

Nicolaysen LO, Hart RJ, and Gale NH (1981) The Vredefort radioelement profile extended to supracrustal strata at Carletonville, with implications for continental heat flow. *Journal of Geophysical Research* 86: 10653–10662.

Nisbet EG, Cheadle MJ, Arndt NT, and Bickle MJ (1995) Constraining the potential temperature of the Archean mantle: A review of the evidence from komatiites. *Lithos* 30: 291–307.

Nomura R, Ozawa H, Tateno S, et al. (2011) Spin crossover and iron-rich silicate melt in the Earth's deep mantle. *Nature* 473: 199–202.

Nyblade AA (1997) Heat flow across the East African Plateau. *Geophysical Research Letters* 24: 2083–2086.

Oganov AR and Ono S (2004) Theoretical and experimental evidence for a post-perovskite phase of $MgSiO_3$ in Earth's D″ layer. *Nature* 430: 445–448.

Ogawa M, Schubert G, and Zebib A (1991) Numerical simulations of three-dimensional thermal convection in a fluid with strongly temperature-dependent viscosity. *Journal of Fluid Mechanics* 233: 299–328.

Olson P (1987) A comparison of heat transfer laws for mantle convection at very high Rayleigh numbers. *Physics of the Earth and Planetary Interiors* 48: 153–160.

Olson P (1990) Hot spots, swells and mantle plumes. In: *Magma Transport and Storage*, pp. 33–51. New York: Wiley.

Palme H and O'Neill HSC (2003) Cosmochemical estimates of mantle composition. In: Carlson RW (ed.) *Mantle and Core*. *Treatise on Geochemistry*, vol. 2. Amsterdam: Elsevier.
Pari G and Peltier WR (2000) Subcontinental mantle dynamics: A further analysis based on the joint constraints of dynamic surface topography and free-air gravity. *Journal of Geophysical Research* 105: 5635–5662.
Parsons B (1982) Causes and consequences of the relation between area and age of the ocean floor. *Journal of Geophysical Research* 87: 289–302.
Parsons B and Sclater JG (1977) An analysis of the variation of ocean floor bathymetry and heat flow with age. *Journal of Geophysical Research* 82: 803–827.
Peltier WR and Jarvis GT (1982) Whole mantle convection and the thermal evolution of the earth. *Physics of the Earth and Planetary Interiors* 29: 281–304.
Perry HKC, Jaupart C, Mareschal JC, and Bienfait G (2006) Crustal heat production in the Superior Province, Canadian Shield, and in North America inferred from heat flow data. *Journal of Geophysical Research* 111: B07301.
Perry HKC, Mareschal J, and Jaupart C (2009) Enhanced crustal geo-neutrino production near the Sudbury Neutrino Observatory, Ontario, Canada. *Earth and Planetary Science Letters* 288: 301–308.
Pinet C and Jaupart C (1987) The vertical distribution of radiogenic heat production in the Precambrian crust of Norway and Sweden: Geothermal implications. *Geophysical Research Letters* 14: 260–263.
Pinet C, Jaupart C, Mareschal J-C, Gariepy C, Bienfait G, and Lapointe R (1991) Heat flow and structure of the lithosphere in the eastern Canadian shield. *Journal of Geophysical Research* 96: 19941–19963.
Poirier J-P (2000) *Introduction to the Physics of the Earth's Interior*. 2nd edn. Cambridge: Cambridge University Press.
Pollack HN and Chapman DS (1977a) On the regional variations of heat flow, geotherms, and lithospheric thickness. *Tectonophysics* 38: 279–296.
Pollack HN and Chapman DS (1977b) Mantle heat flow. *Earth and Planetary Science Letters* 34: 174–184.
Pollack HN, Hurter SJ, and Johnston JR (1993) Heat flow from the earth's interior: Analysis of the global data set. *Reviews of Geophysics* 31: 267–280.
Poort J and Klerkx J (2004) Absence of a regional surface thermal high in the Baikal rift: New insights from detailed contouring of heat flow anomalies. *Tectonophysics* 383: 217–241.
Pozzo M, Davies CJ, Gubbins D, and Alfè D (2012) Thermal and electrical conductivity of iron at Earth's core conditions. *Nature* 485: 355–358.
Putirka KD, Perfit M, Ryerson FJ, and Jackson MG (2007) Ambient and excess mantle temperatures, olivine thermometry, and active vs passive upwelling. *Chemical Geology* 241: 177–206.
Raghavan RS, Schoenert S, Enomoto S, Shirai J, Suekane F, and Suzuki A (1998) Measuring the global radioactivity in the Earth by multidetector antineutrino spectroscopy. *Physical Review Letters* 80: 635–638.
Ramondec P, Germanovich L, Damm KV, and Lowell R (2006) The first measurements of hydrothermal heat output at 9°50′N, East Pacific Rise. *Earth and Planetary Science Letters* 245: 487–497.
Rao YH, Subrahmanyam C, Sharma SR, Rastogi AA, and Deka B (2001) Estimates of geothermal gradients and heat flow from BSRs along the Western Continental Margin of India. *Geophysical Research Letters* 28: 355–358.
Ray RD, Eanes RJ, and Chao BF (1996) Detection of tidal dissipation in the solid earth by satellite tracking and altimetry. *Nature* 381: 595–597.
Reiter M and Jessop AM (1985) Estimates of terrestrial heat flow in offshore eastern Canada. *Canadian Journal of Earth Sciences* 22: 1503–1517.
Ribe NM and Christensen UR (1994) Three-dimensional modeling of plume–lithosphere interaction. *Journal of Geophysical Research* 99: 669–682.
Ricard Y, Šrámek O, and Dubuffet F (2009) A multi-phase model of runaway core–mantle segregation in planetary embryos. *Earth and Planetary Science Letters* 284: 144–150.
Ringwood AE (1962) A model for the upper mantle. *Journal of Geophysical Research* 67: 857–867.
Rolandone F, Jaupart C, Mareschal JC, et al. (2002) Surface heat flow, crustal temperatures and mantle heat flow in the Proterozoic Trans-Hudson Orogen, Canadian Shield. *Journal of Geophysical Research* 107: 2314. http://dx.doi.org/10.1029/2001JB000698.
Rothschild CG, Chen MC, and Calaprice FP (1998) Antineutrino geophysics with liquid scintillator detectors. *Geophysical Research Letters* 25: 1083–1086.
Rowley DB (2002) Rate of plate creation and destruction: 180 Ma to present. *Geological Society of America Bulletin* 114: 927–933.
Roy RF, Decker ER, Blackwell DD, and Birch F (1968) Heat flow in the United States. *Journal of Geophysical Research* 73: 5207–5221.
Roy S and Rao RUM (2000) Heat flow in the Indian shield. *Journal of Geophysical Research* 105: 25587–25604.
Royer J, Müller R, Gahagan L, et al. (1992) A global isochron chart. *Technical Report 117*, University of Texas Institute for Geophysics, Austin.
Rubie DC, Melosh HJ, Reid JE, Liebske C, and Righter K (2003) Mechanisms of metal–silicate equilibration in the terrestrial magma ocean. *Earth and Planetary Science Letters* 205: 239–255.
Rudnick RL and Fountain DM (1995) Nature and composition of the continental crust: A lower crustal perspective. *Reviews of Geophysics* 33: 267–310.
Rudnick RL and Gao S (2003) Composition of the continental crust. In: Rudnick RL (ed.) *Treatise on Geochemistry*. *The Crust*, vol. 3, pp. 1–64. New York: Pergamon.
Rudnick RL, McDonough WF, and O'Connell RJ (1998) Thermal structure, thickness and composition of continental lithosphere. *Chemical Geology* 145: 395–411.
Rudnick RL and Nyblade AA (1999) The thickness of Archean lithosphere: Constraints from xenolith thermobarometry and surface heat flow. In: Fei Y, Bertka CM, and Mysen BO (eds.) *Mantle Petrology: Field Observations and High Pressure Experimentation: A Tribute to Francis R. (Joe) Boyd*, pp. 3–11. Geochemical Society.
Rushmer T, Minarik WG, and Taylor GJ (2000) Physical processes of core formation. In: Canup RM and Drake K (eds.) *Origin of the Earth and Moon*, pp. 227–243. Tucson, AZ: University of Arizona Press.
Russell JK, Dipple GM, and Kopylova MG (2001) Heat production and heat flow in the mantle lithosphere, Slave craton, Canada. *Physics of the Earth and Planetary Interiors* 123: 27–44.
Rybach L (1988) Determination of heat production rate. In: Haenel R, Rybach L, and Stegena L (eds.) *Handbook of Terrestrial Heat-Flow Density Determination*, pp. 125–142. Dordrecht: Kluwer.
Schubert G, Stevenson D, and Cassen P (1980) Whole planet cooling and the radiogenic heat source contents of the Earth and Moon. *Journal of Geophysical Research* 85: 2531–2538.
Schubert G, Turcotte DL, and Olson P (2001) *Mantle Convection in the Earth and Planets*. Cambridge: Cambridge University Press.
Schubert G and Young RE (1976) Cooling the Earth by whole mantle subsolidus convection: A constraint on the viscosity of the lower mantle. *Tectonophysics* 35: 201–214.
Sclater JG and Crowe J (1979) A heat flow survey at anomaly 13 on the Reykjanes Ridge: A critical test of the relation between heat flow and age. *Journal of Geophysical Research* 84: 1593–1602.
Sclater JG and Francheteau J (1970) The implications of terrestrial heat flow observations on current tectonic and geochemical models of the crust and upper mantle of the earth. *Geophysical Journal of the Royal Astronomical Society* 20: 509–542.
Sclater JG, Jaupart C, and Galson D (1980) The heat flow through oceanic and continental crust and the heat loss of the Earth. *Reviews of Geophysics and Space Physics* 18: 269–312.
Seton M, Gaina C, Muller RD, and Heine C (2009) Mid-Cretaceous seafloor spreading pulse: Fact or fiction? *Geology* 37: 687–690.
Sharpe HN and Peltier WR (1978) Parameterized mantle convection and the Earth's thermal history. *Geophysical Research Letters* 5: 737–740.
Singh SC, Minshull TA, and Spence GD (1993) Velocity structure of a gas hydrate reflector. *Science* 260: 204–207.
Sleep NH (1971) Thermal effects of the formation of Atlantic continental margins by continental break up. *Geophysical Journal of the Royal Astronomical Society* 24: 325–350.
Sleep NH (1979) Thermal history and degassing of the earth: Some simple calculations. *Journal of Geology* 87: 671–686.
Sleep NH (1990) Hotspots and mantle plumes: Some phenomenology. *Journal of Geophysical Research* 95: 6715–6736.
Sleep NH (2000) Evolution of the mode of convection within terrestrial planets. *Journal of Geophysical Research* 105: 17563–17578.
Solomatov VS (2000) Fluid dynamics of a terrestrial magma ocean. In: Canup RM, Righter K, and 69 Collaborating Authors (eds.) *Origin of the Earth and Moon*, pp. 323–338. Tucson, AZ: University of Arizona Press.
Solomatov VS and Moresi LN (1997) Three regimes of mantle convection with non-Newtonian viscosity and stagnant lid convection on the terrestrial planets. *Geophysical Research Letters* 24: 1907–1910.
Sotin C and Labrosse S (1999) Three-dimensional thermal convection of an isoviscous, infinite Prandtl number fluid heated from within and from below: Applications to heat transfer in planetary mantles. *Physics of the Earth and Planetary Interiors* 112: 171–190.
Spinelli GA and Harris RN (2011) Effects of the legacy of axial cooling on partitioning of hydrothermal heat extraction from oceanic lithosphere. *Journal of Geophysical Research* 116: 9102.

Šrámek O, Milelli L, Ricard Y, and Labrosse S (2012) Thermal evolution and differentiation of planetesimals and planetary embryos. *Icarus* 217: 339–354.
Šrámek O, Ricard Y, and Dubuffet F (2010) A multiphase model of core formation. *Geophysical Journal International* 181: 198–220.
Stacey FD and Davis PM (2008) *Physics of the Earth*. 4th edn. Cambridge: Cambridge University Press.
Stein CA and Stein S (1992) A model for the global variation in oceanic depth and heat flow with lithospheric age. *Nature* 359: 123–129.
Stevenson DJ (1989) Formation and early evolution of the Earth. In: Peltier W (ed.) *Mantle Convection*, pp. 817–873. New York: Gordon and Breach.
Stevenson DJ (1990) Fluid dynamics of core formation. In: Newsom HE and Jones JH (eds.) *Origin of the Earth*, pp. 231–249. New York: Oxford University Press.
Stevenson DJ (2003) Mission to earth's core – A modest proposal. *Nature* 423: 239–240.
Stixrude L (1997) Structure and sharpness of phase transitions and mantle discontinuities. *Journal of Geophysical Research* 102: 14835–14852.
Strutt RJ (1906) On the distribution of radium in the earth's crust and on internal heat. *Proceedings of the Royal Society of London, Series A* 77: 472–485.
Su YJ (2000) *Mid-Ocean Ridge Basalt Trace Element Systematics: Constraints from Database Management, ICPMS Analysis, Global Data Compilation and Petrologic Modeling*. Unpublished PhD Thesis, Columbia University, New York, No. 1, 569 pp.
Swanberg CA, Chessman MD, Simmons G, Smithson SB, Grnlie G, and Heier KS (1974) Heat-flow heat-generation studies in Norway. *Tectonophysics* 23: 31–48.
Tackley PJ (2000) Self-consistent generation of tectonic plates in time-dependent, three-dimensional mantle convection simulations, 1. Pseudoplastic yielding. *Geochemistry, Geophysics, Geosystems* 1: 1021.
Tateno S, Hirose K, Sata N, and Ohishi Y (2009) Determination of post-perovskite phase transition boundary up to 4400 K and implications for thermal structure in D″ layer. *Earth and Planetary Science Letters* 277: 130–136.
Thomas CW, Liu Q, Agee CB, Asimow PD, and Lange RA (2012) Multi-technique equation of state for $Fe_2SiO_4$ melt and the density of Fe-bearing silicate melts from 0 to 161 GPa. *Journal of Geophysical Research* 117: B10206.
Thomson W (1864) On the secular cooling of the earth. *Transactions of the Royal Society of Edinburgh* 23: 295–311.
Turcotte DL and Oxburgh ER (1967) Finite amplitude convective cells and continental drift. *Journal of Fluid Mechanics* 28: 29–42.
Ulvrová M, Coltice N, Ricard Y, Labrosse S, Dubuffet F, and Sramek O (2011) Compositional and thermal equilibration of particles, drops and diapirs in geophysical flows. *Geochemistry, Geophysics, Geosystems* 12: 1–11.
Unternehr P, Peron-Pinvidic G, Manatschal G, and Sutra E (2010) Hyper-extended crust in the South-Atlantic: In search of a model. *Petroleum Geoscience* 16: 207–215.
Urey HC (1964) A review of atomic abundances in chondrites and the origin of meteorites. *Reviews of Geophysics* 2: 1–34.
Vasseur G and Singh RN (1986) Effects of random horizontal variations in radiogenic heat source distribution on its relationship with heat flow. *Journal of Geophysical Research* 91: 10397–10404.
Villinger H, Grevemeyer I, Kaul N, Hauschild J, and Pfender M (2002) Hydrothermal heat flux through aged oceanic crust: Where does the heat escape? *Earth and Planetary Science Letters* 202: 159–170.
Vočadlo L, Alfè D, Gillan MJ, and Price GD (2003) The properties of iron under core conditions from first principles calculations. *Physics of the Earth and Planetary Interiors* 140: 101–125.
Vogt PR and Ostenso NA (1967) Steady state crustal spreading. *Nature* 215: 810–817.
Vosteen HD, Rath V, Clauser C, and Lammerer B (2003) The thermal regime of the Eastern Alps from inverse analyses along the TRANSALP profile. *Physics and Chemistry of the Earth* 28: 393–405.
Wasserburg G, McDonald GJF, Hoyle F, and Fowler WA (1964) Relative contributions of uranium, thorium, and potassium to heat production in the earth. *Science* 143: 465–467.
Wasson JT and Kalleymen GW (1988) Composition of chondrites. *Philosophical Transactions of the Royal Society of London* 325: 535–544.
Wetherill GW (1990) Formation of the Earth. *Annual Review of Earth and Planetary Sciences* 18: 205–256.
Whitmarsh RB, Manatschal G, and Minshull TA (2001) Evolution of magma-poor continental margins from rifting to seafloor spreading. *Nature* 413: 150–154.
Williams Q and Garnero EJ (1996) Seismic evidence for partial melt at the base of the Earth's mantle. *Science* 273: 1528.
Williams DL, Herzen RP, Sclater JG, and Anderson RN (1974) The Galapagos Spreading Centre: Lithospheric cooling and hydrothermal circulation. *Geophysical Journal of the Royal Astronomical Society* 38: 587–608.
Williams DL and von Herzen RP (1974) Heat loss from the earth: New estimate. *Geology* 2: 327–328.
Workman RK and Hart SR (2005) Major and trace element composition of the depleted MORB mantle (DMM). *Earth and Planetary Science Letters* 231: 53–72.
Zerr A, Diegeler A, and Boehler R (1998) Solidus of Earth's deep mantle. *Nature* 281: 243–246.
Zschau J (1986) Constraints from the Chandler wobble period. In: Anderson AJ and Cazenave A (eds.) *Space Geodesy and Geodynamics*, pp. 315–344. New York: Academic Press.